Universidad Autónoma de San Luis Potosí

Centro de Investigación y Estudios de Posgrado
Facultad de Ingeniería

Estudio de un Esquema de Electrónica de Potencia para Inercia Virtual basado en Baterías

TESIS

QUE PARA OBTENER EL GRADO DE:

Doctor en Ingeniería Eléctrica

PRESENTA:

M.C. Alberto Arellanes Duran

ASESOR:

Dr. Ciro Alberto Núñez Gutiérrez

CO-ASESOR:

Dra. Nancy Visairo Cruz

San Luis Potosí, S.L.P. Enero de 2023

Universidad Autónoma de San Luis Potosí

Centro de Investigación y Estudios de Posgrado
Facultad de Ingeniería

Study of a Power Electronics Scheme for Virtual Inertia based on Batteries

TESIS

QUE PARA OBTENER EL GRADO DE:

Doctor en Ingeniería Eléctrica

PRESENTA:

M.C. Alberto Arellanes Duran

ASESOR:

Dr. Ciro Alberto Núñez Gutiérrez

CO-ASESOR:

Dra. Nancy Visairo Cruz

San Luis Potosí, S.L.P. Enero de 2023

Universidad Autónoma de San Luis Potosí

Facultad de Ingeniería

Centro de Investigación y Estudios de Posgrado

Doctorado en Ingeniería Eléctrica

"Estudio de un Esquema de Electrónica de Potencia para Inercia Virtual basado en Baterías"

Presenta: _____

M.C. Alberto Arellanes Duran

Sinodales:

_____ _____

Dr. Ciro Alberto Núñez Gutiérrez
(Director de tesis)

Dra. Nancy Visairo Cruz
(Co-directora de tesis)

_____ _____

Dr. Rafael Peña Gallardo

Dr. Juan Segundo Ramírez

_____

Dr. Eugenio Camargo Trigueros

UASLP
Universidad Autónoma de San Luis Potosí

FACULTAD DE INGENIERÍA

17 de noviembre de 2022

M. C. ALBERTO ARELLANES DURAN
P R E S E N T E.

En atención a su solicitud de Temario, presentada por los **Dres. Ciro Alberto Núñez Gutiérrez y Nancy Visairo Cruz**, Asesor y Coasesora de la Tesis que desarrollará Usted, con el objeto de obtener el Grado de **Doctor en Ingeniería Eléctrica**, me es grato comunicarle que en la sesión del H. Consejo Técnico Consultivo celebrada el día 17 de noviembre del presente, fue aprobado el Temario propuesto:

TEMARIO:

"Estudio de un Esquema de Electrónica de Potencia para Inercia Virtual basado en Baterías"

1. Introducción.
2. Descripción de sistemas de almacenamiento de energía basados en baterías
3. Modelado del convertidor CD/CA y filtro LCL
4. Diseño del esquema de control holístico
5. Evaluación de desempeño
6. Conclusiones.

   Apéndices.

   Bibliografía.

"MODOS ET CUNCTARUM RERUM MENSURAS AUDEBO"

A T E N T A M E N T E

DR. EMILIO JORGE GONZÁLEZ GALVÁN
DIRECTOR.

UNIVERSIDAD AUTONOMA DE SAN LUIS POTOSI
FACULTAD DE INGENIERIA
DIRECCION

Copia. Archivo
*etn.

"Rumbo al centenario de la autonomía universitaria"

ANIVERSARIO DE LA AUTONOMÍA UASLP 2023

www.uaslp.mx

Av. Manuel Nava 8
Zona Universitaria • CP 78290
San Luis Potosí, S.L.P.
tel. (444) 826 2330 al39
fax (444) 826 2336

UNIVERSIDAD AUTÓNOMA DE SAN LUIS POTOSÍ
FACULTAD DE INGENIERÍA

Centro de Investigación y Estudios de Posgrado

Posgrado en Ingeniería Eléctrica

Los firmantes, Dr. Ciro Alberto Núñez Gutiérrez y Dra. Nancy Visairo Cruz, profesores investigadores de la Universidad Autónoma de San Luis Potosí

HACEN CONSTAR

Que la tesis que tiene por título:

Estudio de un Esquema de Electrónica de Potencia para Inercia Virtual basado en Baterías

Presentada por el Sr:

M.C. Alberto Arellanes Duran

Para optar por el grado de:

Doctor en Ingeniería Eléctrica

Ha sido realizada bajo su dirección

Rúbricas: _____

Dr. Ciro Alberto Núñez Gutiérrez

_____

Dra. Nancy Visairo Cruz

San Luis Potosí, S.L.P. México, febrero de 2023

UNIVERSIDAD AUTÓNOMA DE SAN LUIS POTOSÍ

FACULTAD DE INGENIERÍA

Área de Investigación y Estudios de Posgrado

Aclaración

El presente trabajo que lleva por título:

"Estudio de un Esquema de Electrónica de Potencia para Inercia Virtual basado en Baterías"

se realizó en el periodo enero de 2019 a febrero de 2023 bajo la dirección del Dr. Ciro Alberto Núñez Gutiérrez y la Dra. Nancy Visairo Cruz.

Originalidad

Por este medio aseguro que he realizado este documento de tesis para fines académicos sin ayuda indebida de terceros y sin utilizar otros medios más que los indicados.

Las referencias e información tomadas directa o indirectamente de otras fuentes se han definido en el texto como tales y se ha dado el debido crédito a las mismas.

El autor exime a la UASLP de las opiniones vertidas en este documento y asume la responsabilidad total del mismo.

Este documento no ha sido sometido como tesis a ninguna otra institución nacional o internacional en forma parcial o total.

Se autoriza a la UASLP para que divulgue este documento de Tesis para fines académicos.

Nombre y Firma del autor

_____

A mis padres con amor José Luis Arellanes Cobos y Marisela Durán Gamez
En verdad, gracias.

Acknowledgment

Me gustaría agradecer a mis asesores, el Dr. Ciro Alberto Núñez Gutiérrez y Dra. Nancy Visairo Cruz, por ser mis mentores, por su guía, consejos, enseñanzas, asesorías, motivaciones y por la confianza y seguridad que ambos me dieron para la realización de este trabajo y mi estudio aquí en la Universidad Autónoma de San Luis Potosí.

También agradezco a los demás miembros de mi comité asesor, Dr. Juan Segundo Ramírez, Dr. Rafael Peña Gallardo y Dr. Eugenio Camargo Trigueros, por sus valiosas sugerencias y ayuda. Quiero dar mi agradecimiento especial al Dr. Juan Segundo por la resolución de dudas durante la investigación de tesis.

A mi compañera de vida Clarissa Nallely Acosta Campas.

A mis hermanos Victor Manuel, José Luis, Jesús y Alan René.

A mis compañeros de posgrado Humberto, Miguel, Julio, Josue, Dante y Roberto.

Por último quiero agradecer a CONACYT por brindarme el apoyo económico durante mis estudios de posgrado, siendo becario con el CVU: 738225.
Este trabajo fue apoyado por el Consejo Nacional de Ciencia y Tecnología (CONACYT) bajo el Proyecto A1-S-29705

Abstract

This thesis addresses the design of a holistic control for a Battery Energy Storage System (BESS) to provide operational improvements. This kind of system are continuously growing in applications related with punctual operations depending on the desired profitability accompanied with its use. However, a research gap has been detected when a completely unified control is desired; it means, to avoid of transformations, double loops, and several tuning controllers to address each control objective.

The technology for BESS is growing fast as a result of declining prices over the previous ten years. Additionally, the BESS provides more options for better-balancing fluctuations in the variable renewable electricity penetration, which is used not only for one application but also for various applications. The BESS must, however, be able to operate in a variety of modes in order to complete these applications. The controllers that address these operation modes are a part of the so-called "Hierarchical Control". From this perspective, a significant motivation for this work is to design a unified control to manage all the operation modes and make the operation-modes transition seamlessly, thereby not compromising the electrical power system stability. The hypothesis proposes that there may achieve a specific tuning process for the linear state feedback technique with integral action in which the same controller gains are used for the three operation modes: 1) isolated mode, 2) mode Grid-connected (inverter) and 3) Grid-connected (rectifier) mode. Besides that, a seamless transition can be achieved. The Butterworth linear polynomial approach is proposed for the LCL filter design and the closed-loop control tuning in a concatenated way. The design is developed with the islanded operation mode as a reference point because the transfer function satisfies the requirement of the dimensional similitude between the input and output, which refers to the input voltage and output voltage. This approach suggests a tuning factor for the closed-loop system considering the wideband and the switching frequency of the system. This shows how the LCL filter design and control gains tuning are connected as a part of an integrated design process. The eigenvalues locus shows that the system is stable for each operating mode. According to these findings, gains do not need to be re-tuned because the same tuning gains applied to all operating modes satisfy the desired performance of the system, this specific methodology is called in this thesis "Holistic control". It is clear from the development of this thesis work how a minor modification

in the tuning methodology represents an opportunity to enhance the energy efficiency in the mode transitions. When the energy requirements are evaluated, the results show a clear difference between the tuning process, showing improved performance that results in significant energy savings between 12% and 90%. In addition, the settling time is also considerably reduced. This result, which served as the inspiration for this study, is pertinent when a significant amount of power should be transferred to achieve, among others, power peak shaving, frequency support, and islanding mode. To evaluate the seamless transition among operating modes, load steps and step references simulation runs were performed on the PSCAD/EMTDC. They show that the closed-loop system fulfills the voltage and frequency thresholds required by IEEE 1547-2018 for seamless transitions. Besides, an analytical comparison of the energy consumption between tuning methods is made by using MATLAB SIMULINK (2018a). Finally, experimental results in a 617 W, 120 V_{L-L} three-phase converter prototype are also presented to show the feasibility of the improved holistic control.

List of abbreviations

$/kWh Dollar per Kilowatt-hour.

AC Alternating Current.

BESS Battery Energy Storage Systems.

BRK Breaker.

DC Direct Current.

DER Distributed Energy Resources.

DSP Digital Signal Processor.

EPRI Electric Power Research Institute.

ES Energy Storage.

gci Grid Connected (Inverter) Mode.

gcr Grid Connected (Rectifier) Mode.

IEC International Electrotechnical Commission.

IEEE Institute of Electrical and Electronics Engineers.

ism Islanded-mode.

kWh Kilowatt-hour.

L-L Line to Line.

MOSFET Metal–oxide–semiconductor field-effect transistor.

p.u. Per-unit.

PCB Printed Circuit Board.

PCC Point of Common Coupling.

PLL Phase Locked Loop.

PWM Pulse Width Modulation.

RMS Root Mean Square.

RoCoF Rate of Change of Frequency.

SiC Silicon carbide.

SOC State of Charge.

SPWM Sinusoidal Pulse Width Modulation.

THD Total Harmonic Distortion.

List of symbols

$\dot{\sigma}_{\text{ism}}$ Error between the voltage reference and measured voltage.

η Energy efficiency.

$|G\,(jw)_{\text{h199}}|$ Gain at the frequency of the first relevant harmonic.

$\alpha_{\text{i\_j\_cl}}$ Eigenvalue i of j operation mode in closed-loop.

$\alpha_{\text{i\_j}}$ Eigenvalue i of j operation mode in open-loop.

$\widehat{\mathbf{A}}_{\text{gci}}$ State matrix of grid-connected mode inverter in closed-loop.

$\widehat{\mathbf{A}}_{\text{gcr}}$ State matrix of grid-connected mode rectifier in closed-loop.

$\widehat{\mathbf{A}}_{\text{ism}}$ State matrix of islanded-mode in closed-loop.

$\mathbf{A}_{\text{gci}}$ State matrix of grid-connected mode inverter in open-loop.

$\mathbf{A}_{\text{gcr}}$ State matrix of grid-connected mode rectifier in open-loop.

$\mathbf{A}_{\text{ism}}$ State matrix of islanded-mode in open-loop.

$\mathbf{B}_{\text{gci}}$ Input matrix of grid-connected mode inverter in open-loop.

$\mathbf{B}_{\text{gcr\_1}}$ Input matrix one of grid-connected mode rectifier in open-loop.

$\mathbf{B}_{\text{gcr\_2}}$ Input matrix two of grid-connected mode rectifier in open-loop.

$\mathbf{B}_{\text{ism}}$ Input matrix of islanded-mode in open-loop.

$\mathbf{C}_{\text{gci}}$ Output matrix of grid-connected mode inverter in open-loop.

$\mathbf{C}_{\text{gcr}}$ Output matrix of grid-connected mode rectifier in open-loop.

$\mathbf{C}_{\text{ism}}$ Output matrix of islanded-mode in open-loop.

$\alpha_{\text{ismcl(integral action)}}$ Eigenvalues for islanded-mode in closed-loop for the integral action.

$\alpha_{\text{ismcl(states feedback)}}$ Eigenvalues for islanded-mode in closed-loop for the states feedback.

$k_{i_{holistic}}$ Gain of integral action for holistic first approach.

k_i Gain of integral action.

$h_{199(11940Hz)}$ First relevant harmonic amplitude.

VA_{base} Rated power in VA.

ω_0 Rated angular velocity of the rotor in rad/s.

ω_c Cutoff frequency in rad/s.

ω_m Angular velocity of the rotor in rad/s.

ω_{cl} Closed-loop wideband frequency in rad/s.

$\omega_{h_{199}}$ First relevant harmonic frequency in rad/s.

ω_{sw} Switching frequency in rad/s.

Φ phase-angle between grid voltage and current at fundamental frequency in angle.

C_r Reference capacitor.

C_{DC} DC link capacitor.

C_f Delta LCL-interconnected filter capacitor.

$E_{holistic}$ Energy required by the first approach of the holistic controller.

$E_{improved\_holistic}$ Energy required by the improved holistic controller.

E_{Keq} Kinetic energy stored in synchronous generators.

f Frequency measured at the PCC of the power system in Hz.

f_0 Fundamental frequency in Hz.

f_m Frequency of the rotor in Hz.

$G_{BT}(s)$ Butterworth filter transfer function.

H_{eq} Inertia constant.

H_{sys} Total inertia constant of the power system.

i Number of eigenvalue.

i_a Current through inductor L_{f1} in phase A.

i_A Current through inductor L_{f2} in phase A.

i_b Current through inductor L_{f1} in phase B.

i_B Current through inductor L_{f2} in phase B.

i_c Current through inductor L_{f1} in phase C.

i_C Current through inductor L_{f2} in phase C.

$i_{a'b'}$ Delta-connected AB capacitor current.

$i_{b'c'}$ Delta-connected BC capacitor current.

$i_{c'a'}$ Delta-connected CA capacitor current.

i_{cDC} DC link capacitor current.

i_{ch} DC link impedance current.

i_{DC} DC bus current.

j Operation mode ism, gci or gcr.

J_g Moment of inertia of the synchronous machine.

L_r Reference inductor.

L_{f1} Delta LCL-interconnected filter input inductor.

L_{f2} Delta LCL-interconnected filter output inductor.

M Introduced tuning factor.

m_a Amplitude modulation index.

m_f Frequency modulation index.

P_e Electromagnetic active power.

P_m^* Market active power reference.

P_r^* Regulation active power reference.

P_t^* Total active power reference.

P_v Steam valve position.

P_{ab_holistic} Power delivered by the first approach holistic control.

$P_{ab\_\text{improved\_holistic}}$ Power delivered by the improved holistic control.

P_{ab}^* Power reference at steady state for the ab_{L-L}.

P_{AC} Power in the AC side of the DC/AC converter.

P_{anci}^* Extra ancillary services active power reference.

P_{DC} Power in the DC side of the DC/AC converter.

P^*_{droop} Droop control active power reference.

$P_{g(s)}$ Governor mechanism output.

$P^*_{inertia}$ Inertia active power reference.

P_{mec} Mechanical active power.

P^*_{mec} Mechanical active power reference.

$Q(s)$ Butterworth filter polynomial.

Q^*_m Market reactive power reference.

Q^*_r Regulation reactive power reference.

Q^*_t Total reactive power reference.

Q^*_{anci} Extra ancillary services reactive power reference.

Q^*_{droop} Droop control reactive power reference.

r Reference of the controlled input.

r_{gci} Reference of the controlled input in Grid-connected mode inverter.

r_{gcr} Reference of the controlled input in Grid-connected mode rectifier.

r_{ism} Reference of the controlled input in islanded-mode.

T_a Accelerating torque.

T_e Electromagnetic torque.

T_m Mechanical torque.

t_{event} Time at the event occurrence.

t_{holistic} Time where the error between P^*_{ab} and P_{ab_holistic} is $< 1\%$.

$t_{\text{improved\_holistic}}$ Time where the error between P^*_{ab} and $P_{ab\_\text{improved\_holistic}}$ is $< 1\%$.

$v_{a'}$ Voltage in node a'.

$v_{ab_{gci}}$ Control law wich modifies the inverter ab_{L-L} output in grid-connected mode inverter.

$v_{ab_{gcr}}$ Control law wich modifies the inverter ab_{L-L} output in grid-connected mode rectifier.

$v_{ab_{ism}}$ Control law wich modifies the inverter ab_{L-L} output in islanded-mode.

v_{ab} Delta-connected output AB voltage of the power converter.

v_{AB} Delta-connected grid AB voltage.

$v_{b'}$ Voltage in node b'.

v_{bc} Delta-connected output BC voltage of the power converter.

v_{BC} Delta-connected grid BC voltage.

$v_{c'}$ Voltage in node c'.

v_{cAB} Delta-connected AB capacitor voltage.

v_{ca} Delta-connected output CA voltage of the power converter.

v_{CA} Delta-connected grid CA voltage.

v_{cBC} Delta-connected BC capacitor voltage.

v_{cCA} Delta-connected CA capacitor voltage.

V_{DC} DC link capacitor voltage.

V_{DC}^{*} Voltage reference in the DC bus.

$Z_{AB-BESS}$ Delta-connected AB impedance for the BESS in p.u.

$Z_{AB-grid}$ Delta-connected AB impedance for the grid in p.u.

Z_{AB} Delta-connected AB impedance.

$Z_{BC-BESS}$ Delta-connected BC impedance for the BESS in p.u.

$Z_{BC-grid}$ Delta-connected BC impedance for the grid in p.u.

Z_{BC} Delta-connected BC impedance.

$Z_{CA-BESS}$ Delta-connected CA impedance for the BESS in p.u.

$Z_{CA-grid}$ Delta-connected CA impedance for the grid in p.u.

Z_{CA} Delta-connected CA impedance.

Z_{ch} DC link capacitor impedance.

Z_{DC} Impedance in the DC bus.

Z_{load} Rated load value.

k Gain vector.

$\mathbf{k}_{\text{holistic}}$ Gain vector for holistic first approach.

$\mathbf{x}$ State vector.

Índice

Contents

List of Figures

List of Tables

Chapter 1

Introduction

Background

A transformation is taking place in the current electrical power systems. The classic power system previously dominated by large synchronous machines with slow dynamics is evolving. This is due to the significant percentage of penetration of the called "renewable resources" connected using power electronics.

For instance, in 2021 the first 10 % of penetration was achieved, although some countries have documented much higher shares. For example, Uruguay (35%), Ireland (31%), Portugal (32%), Spain (32%), and Denmark (53%), among other countries, produced more than 30% of their electricity from renewable, with variable sources like wind and solar energy [1]. These countries, along with others, attained even higher daily maximum levels of variable renewable electricity penetration, with energy production exceeding 40% of end user demand, as seen in Figure (1.1).

Due to the high penetration of renewable energy in the power system and its variable nature, the energy storage has been increased to guarantee the capacity firming. Currently, pumped hydroelectric storage is still the most widely used. However, the attention over the Battery Energy Storage System (BESS) has raised due mainly to its low cost and good performance. To increase its profitability, the BESS can provide not only one service but a combination of them, such as area regulation, power quality, energy time shift, transmission congestion relief and islanded mode, among others.

The battery energy storage system in the power systems

Energy storage infrastructure can contribute to grid stabilization over timescales generally ranging from minutes to days, offering a number of advantages to the energy system and helping in the decarbonization process.

BESS technology is rapidly developing compared to other energy storage systems types. This is due to lower prices in the last decade, decreasing by about 90%, from over USD 1,200 per kilowatt-hour (kWh) in 2010 to about USD 130 per kWh by

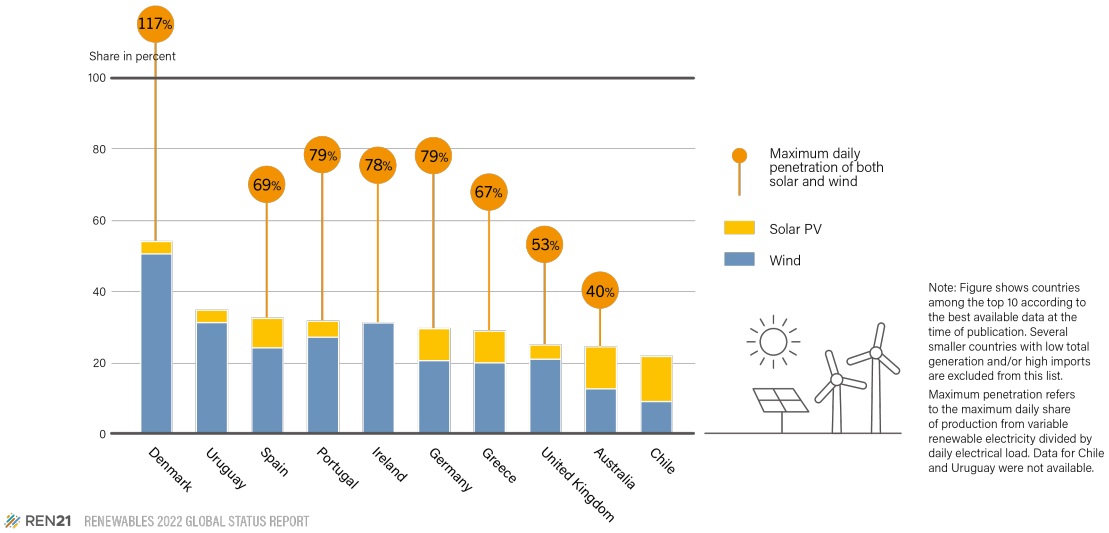

Figure 1.1: Top Countries for Maximum Daily Penetration and Share of Variable Renewable Energy Generation, 2021 [1].

the end of 2021 [8]. Furthermore, the BESS offers more options for better balancing variable renewable electricity penetration fluctuations [1], which is not only used for one application but is also used for multiple applications.

Once a primary, a secondary, or even a third application of the BESS has been chosen, a hierarchical control should be considered for its management.

In Figure 1.2, a typical BESS interconnected to the electrical power system is shown in a block diagram, which consists of the batteries to the left side with a DC/DC power electronic converter, then three-phase full bridge for the adequacy of DC/AC connected to the electrical network and local sensitive loads through a delta LCL filter.

There are numerous applications that use it right now, including frequency regulation, electric energy time-shifting, renewable energy integration, non-spinning electric supply reserve, peak demand, and uninterruptible power systems for sensitive local loads. Among the applications of the BESS, inertial response is also desirable for maintaining the frequency stability of the electrical power system.

To accomplish these applications, the BESS must be able to work in different operation modes; the first one is grid-feeding, in this mode, the BESS can export the specified active or reactive power given by a current reference; the second one is as grid-forming, in this mode, the BESS can regulate its output voltage [9]. These two controllers are part of the level 0 control of the so-called “Hierarchical Control”.

Depending on the level of control being operated, hierarchical control enables the optimization of single or multiple objectives [10]. The hierarchical control triangle for the BESS is shown in Figure 1.2.

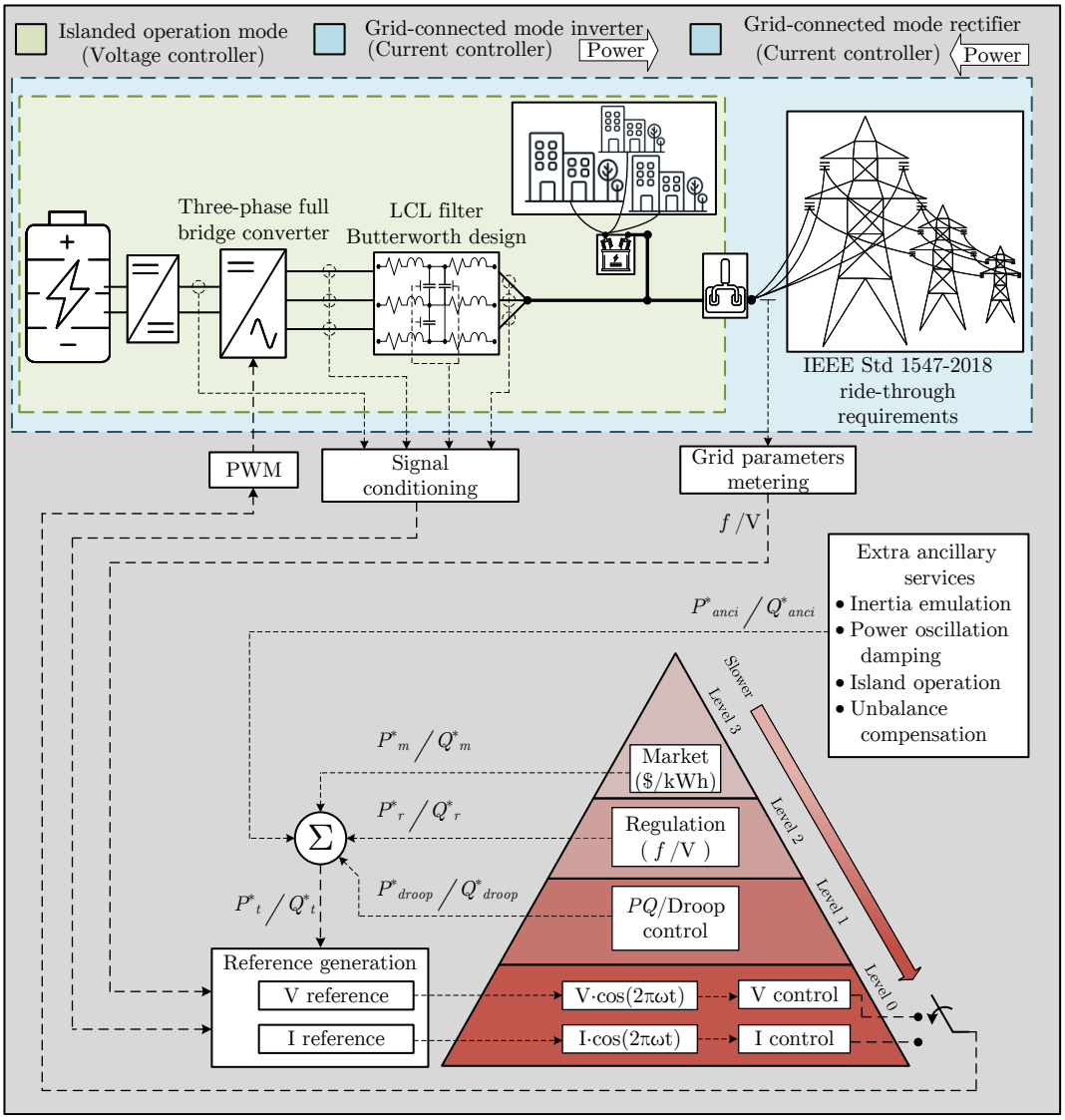

Figure 1.2: BESS interconnected to the grid power system.

Problem statement

The BESS interconnected to the grid must comply with multiple operating tasks so that their interconnection to the electrical grid is profitable and operatively suitable according to the applicable regulations. The hierarchical control provides the operational tasks for all the considered operating modes. This control design should respond seamlessly to each operating mode without exceeding the established thresholds. In both responses, transients and steady state, the control should guarantee

energy efficiency in the power electronics. The problem addressed in this thesis focuses on establishing a control scheme that allows the above in the simplest possible way.

Justification

Working with the grid-connected and island operating modes is an essential requirement in current BESS international projects for performing not one but several applications for the electrical power system. In order to improve the performance during the three modes of operation, a novelty approach is to unify the control scheme by concatenating, through an automatic control standpoint, the requirements of the BESS and the capabilities of the power electronics. Furthermore, the transition among the modes has to be seamless, staying bounded in the continuous operation thresholds established by IEEE 1547-2018. If this is achieved, it is possible to obtain a synergy of the whole system, which means the power system operates smoothly and the power electronics converts energy efficiently.

Hypothesis

By an adequate concatenation between the design of the filtering scheme of a BESS and its control, it is possible to develop a unified control scheme whose tuning based on the knowledge of the physical limits of the BESS results in a unique tuning for all the proposed modes of operation of the BESS and the seamless transition among all modes and load steps.

Thesis objectives

The objective of this thesis is to propose a methodology in the design of the control of the DC/AC converter in conjunction with the LCL filter connected to the electrical power system that fulfills the following characteristics.

- Seamless transition among three different modes such as: grid-connected mode as inverter, grid-connected mode as rectifier, and islanded operation mode.
- Use a single set of gains for all three modes of operation.
- Design the LCL interconnection filter using a Butterworth approach and maintain that dynamic in the control closed loop.
- The addition of virtual inertia as an extra ancillary service.

Particular objectives:

1. Analyse and design concatenating the LCL filter and the control scheme considering a seamless transition.

2. Analyze the performance of the DC/AC converter in all the operation modes, including the virtual inertial as an extra ancillary service, by simulations.

3. Build a three-phase DC/AC converter and the LCL filter to validate experimentally the closed-loop system performance for all the operation modes.

Thesis scope

This thesis aims to demonstrate through simulation in PSCAD and MATLAB SIMULINK (2018a) and through a 617 W, 120 V_{L-L} experiment the seamless transition among the different modes of operation of the BESS. Furthermore, the addition of virtual inertia as an extra ancillary service will be demonstrated in the PSCAD simulation.

Thesis outline

This thesis is organized as follows:

Chapter 1 presents the issues related with penetration of renewable resources and the BESS.

Chapter 2 presents a description of the BESS and how it is classified according to its different applications. Besides, the different operation modes, as well as the requirements of the IEEE 1547-2018 that lies in the scope of this thesis.

Chapter 3 presents the mathematical modeling of the three modes of operation addressed in this work, which are: grid-connected mode as inverter, grid-connected mode as rectifier, and islanded-mode.

Chapter 4 presents the architecture of a hybrid control, a unified control, and how the proposed holistic control is conceptualized for the three modes of operation mentioned in the previous chapter, and how it is incorporated into hierarchical control from two different approaches. In addition, two different methods are presented for incorporating virtual inertia as an ancillary service to BESS.

Chapter 5 presents an evaluation of the performance of the two approaches of the holistic controller presented in the previous chapter; firstly, an analytical comparison is made between the transients of the two approaches, secondly, a simulation of the improved approach is carried out, thirdly the construction together with prototype tests, in fourth the two ways of adding virtual inertia are tested and at the end a discussion of results.

Finally the conclusions and the appendix are given.

Chapter 2

Description of battery energy storage systems

BESS are rechargeable batteries that can store energy from various sources and discharge it as needed. One or more batteries make up BESS, which may be used to stabilize the grid, balance the power supply, and provide backup power. Compared to conventional grid storage solutions, battery storage systems have many advantages, including greater flexibility, lower costs, and higher scalability [1]. BESS provides highly effective and affordable energy storage solutions for all types of energy users, including offshore drilling platforms or vessels, conventional thermal power plant operators, grid operators, and renewable energy producers.

BESS enables energy arbitrage, allowing you to directly lower the electricity bill by peak shaving or even create new revenue streams.

2.1 BESS applications

When evaluating the feasibility of a BESS, it is important to consider the type of application it will be used for. In this section, the applications are divided into categories based on two factors: discharge frequency and duration. For both frequent and infrequent discharge, or for both long and short duration, certain applications may be appropriately categorized as can be seen in Table 2.1 and Figure 2.1. Additionally, it can be beneficial to employ a single energy storage system for multiple purposes.

The four categories are defines as:

- Long duration: these can be considered as energy applications and need to have enough storage capacity to support continuous discharges of one or more hours.
- Short duration: these can be thought of as power applications, prioritizing the ability to charge or discharge faster, typically in a matter of seconds to several minutes.

- Infrequent discharge: those which are discharged no more than 20 times a year or a few times per month.
- Frequent discharge: those that are required to continuously cycle or discharge and recharge stored energy more than 20 times per year.

The Department of Energy, Sandia, and EPRI are making an ongoing effort to come to an agreement on the names and definitions of grid applications. In special, the Sandia National Laboratories characterizes the 17 applications indicated in Table 2.1 with the corresponding power and discharge time requirements based on installed systems [11].

Table 2.1: General power and discharge duration specifications for multiple BESS applications [3].

Application	Discharge Duration (hr)		Storage Power	
	Min.	Max.	Low	High
Electric energy time-shift	2	8	1 MW	500 MW
Electric supply capacity	4	6	1 MW	500 MW
Load following	2	4	1 MW	500 MW
Area regulation	15 min.	30 min.	1 MW	40 MW
Electric supply reserve capacity	1	2	1 MW	500 MW
Voltage support	15 min.	1	1 MW	10 MW
Transmission support	2 s	5 s	10 MW	100 MW
Transmission congestion relief	3	6	1 MW	100 MW
T and D upgrade deferral 50th percentile	3	6	250 kW	5 MW
Substation On-site power	8	16	1.5 kW	5 kW
Time-of-use energy cost management	4	6	1 kW	1 MW
Demand charge management	5	11	50 kW	10 MW
Electric service reliability	5 min.	1	0.2 kW	10 MW
Electric service power quality	10 s	1 min.	0.2 kW	10 MW
Renewable energy time-shift	3	5	0.2 kW	10 MW
Renewable capacity firming	2	4	1 kW	500 MW
Wind generation grid integration (short duration)	10 s	15 min.	0.2 kW	500 MW
Wind generation grid integration (long duration)	1	6	0.2 kW	500 MW

The term “synergies” refers to the practice of combining the advantages of two or more applications in Energy Storage (ES) system, giving as a result an improved the

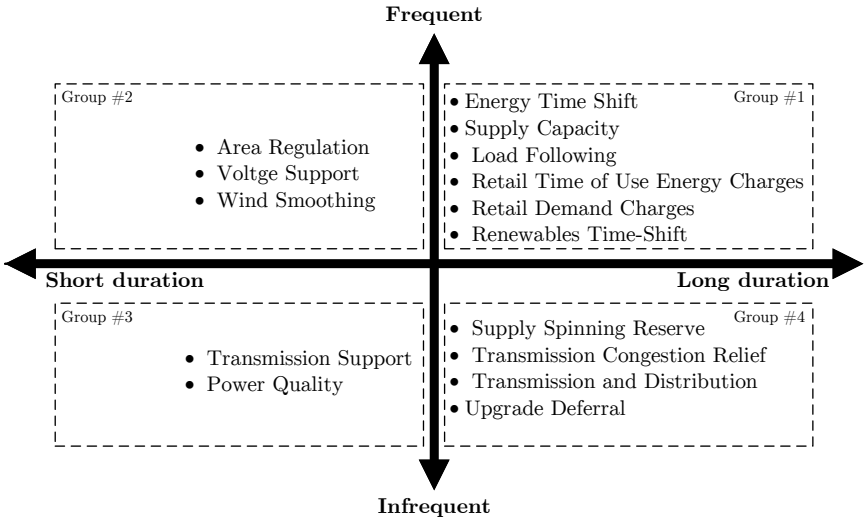

Figure 2.1: BESS application according to discharge frequency and duration.

power system performance. There is only one primary application for this issue, which consumes a significant percentage of operating time, and ancillary applications that can be secondary, tertiary, and successive. Of course, the applications must be compatible with the storage system to be used for all these applications.

2.2 BESS operation modes

All the applications mentioned in the previous section in which the BESS can be used are found within the triangle of a typical BESS control system and auxiliary operations, as shown in Figure 2.2. As can be seen in Figure 2.2, the hierarchical control is divided into four levels, where level zero has the fastest dynamic while level 3 has the slowest dynamic.

Starting at level 0, which is the base for all other control levels, the input of this level are P_t^* and Q_t^* power references, which are the sum of all other references from upper levels of the triangle and extra ancillary services. The input references activate a voltage mode or a current mode, each one with a unique control setup and tuning. At level 1 the P_{droop}^* and Q_{droop}^* references are created through local measurements in the PCC as [12]. Level 2 is associated with the wide-area voltage and frequency regulation references P_r^* and Q_r^*, which support the stability of the power system. Besides, the market variables, such as the price \$/kWh, are related to level 3. When the BESS is desired to participate in the electrical market, the output P_m^* and Q_m^* serve as a reference for the market power dispatch, and as a result, the references vary slowly from this level.

The term "hybrid control" refers to the type of control structure at level 0, where usually, two controllers are designed and tuned separately. One controller allows a

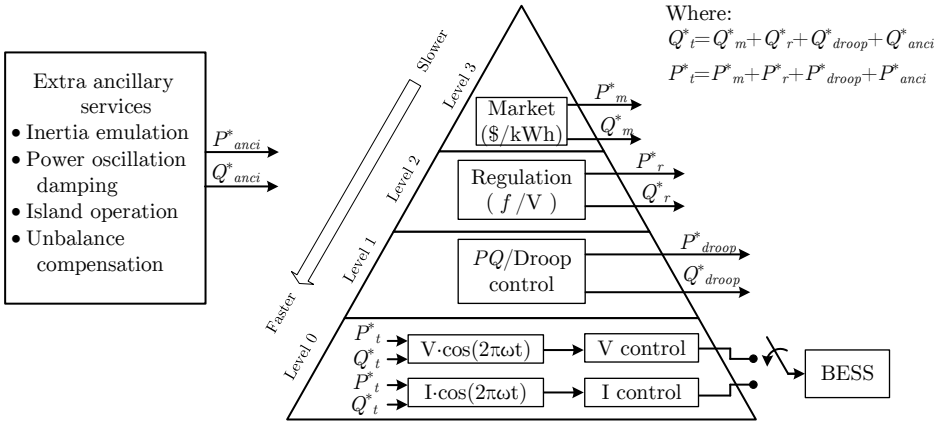

Figure 2.2: Structure of the system and control topology.

sinusoidal output voltage when the island operation mode is needed, and the another keeps the output current in phase with the power system voltage [13, 14, 15, 16]. Additionally, a third controller makes the converter function as a rectifier when the grid-connected mode is necessary to charge the battery. The rectifier controller is typically not included in the BESS references; Nevertheless, it can be found in multiple references devoted to PWM rectifiers, where it is common to find nonlinear control schemes since the nature of the system is bilinear [16, 17, 18].

The unification of the DC/AC power converter controllers in recent years has generated significant interest because it allows the converter to operate in islanded and grid-connected modes using a single control [19, 20]. Level 0 and level 1 are where the called "unified control" operates, which is an improvement of the hybrid control. In level 1, a modified PQ/Droop control is often used, while in level 0, a single V/I control is typically employed, depending on whether voltage or current is desired at the BESS output [17, 19, 21].

In the same manner, the seamless transition among the different modes has become a critical problem for maintaining grid stability [22, 23, 24]. For instance, in [25], the sensitive industrial local loads need an uninterruptible AC power supply, which also minimizes current and voltage spikes during the transients. The voltage and frequency should be kept within the IEEE 1547-2018 standard thresholds to maintain the continuous power system operation while the grid power system is reconnected [2]. Numerous initiatives have addressed the unified control design using various approaches to achieve a seamless transition. Phase-Locked Loop (PLL) design or reconfiguration is one approach. Reference [23] provides a control strategy that uses the inverter as a voltage source and a current source in islanded operation mode and grid-connected mode, respectively. The extension of the PLL, which smoothly switches between the grid reference and an independent reference, is the main accomplishment of that work.

The authors of [26] present a different control strategy based on integrating the PLL into the DC/AC power converter control. The inverter performs pre-synchronization when changing from grid-connected to islanded operation mode. Voltage angle hops are not permitted with this PLL. Another approach is to design or modify the control scheme for the DC/AC converter. In [21], the control strategy uses a voltage droop control strategy to supply the necessary power to local loads while using a feed-forward current control for grid-connected mode. When the inverter is operating in the grid-connected mode, the authors of [27] use a typical control strategy of two cascade controllers into a DQ-frame; however, in this instance, the outer loop is eliminated when the inverter is operating in the islanded operation mode. The authors of [28] suggest a unified control based on a voltage droop control strategy that incorporates power compensation to achieve a smooth changeover between operation modes. In this controller, the saturation is the key for the islanded operation mode, which introduces a power compensation to work as a typical voltage droop control strategy. Reference [29] recommends two distinct controller sets, one for grid-connected mode as a current source and another for islanded operation mode as a voltage source. In the majority of cases, the LCL filter design and the control design are treated separately, according to a recent review of the literature on this subject.

2.3 BESS requirements

The basic structure of a BESS module is shown in Figure 2.3. A battery bank that supplies the necessary energy to the grid and is also charged at a rate that is equal to or greater than that of the discharging one compensates the first stage of a BESS module. For charging and discharging the battery bank, the power conversion is equipped with a battery management DC/DC power converter that determines the appropriate limits. The second stage is the DC/AC power converter and output filter, which satisfy the needs of the grid. The third and last step is the isolation transformer, which connects the BESS to the power system grid providing galvanic isolation.

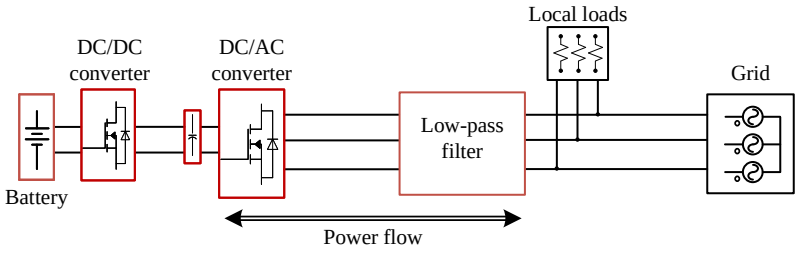

Figure 2.3: Basic structure of a BESS module.

A group of standards and guidelines were looked at in order to identify and specify the BESS requirements based on the operation modes of the previous subsection. This

thesis aimed to provide a common framework for the BESS capabilities for the charging and discharging operating modes.

Accordingly, the contribution focuses on the DC/AC power conversion stage and the low pass filter for interconnection to the electrical power network. Especially in the control of this last stage and the ability of the BESS to work in three different modes, which are: the grid-connected mode as an inverter, the grid-connected mode as a rectifier, and the islanded operation mode. What is aimed in this thesis work is to make a seamless transition among the three operation modes. Therefore the IEEE 1547-2018 standard is taken as a reference and seeks that at all times, the voltage and frequency are maintained in the zone of continuous operation, as shown in Figure 2.4 and Figure 2.5, respectively.

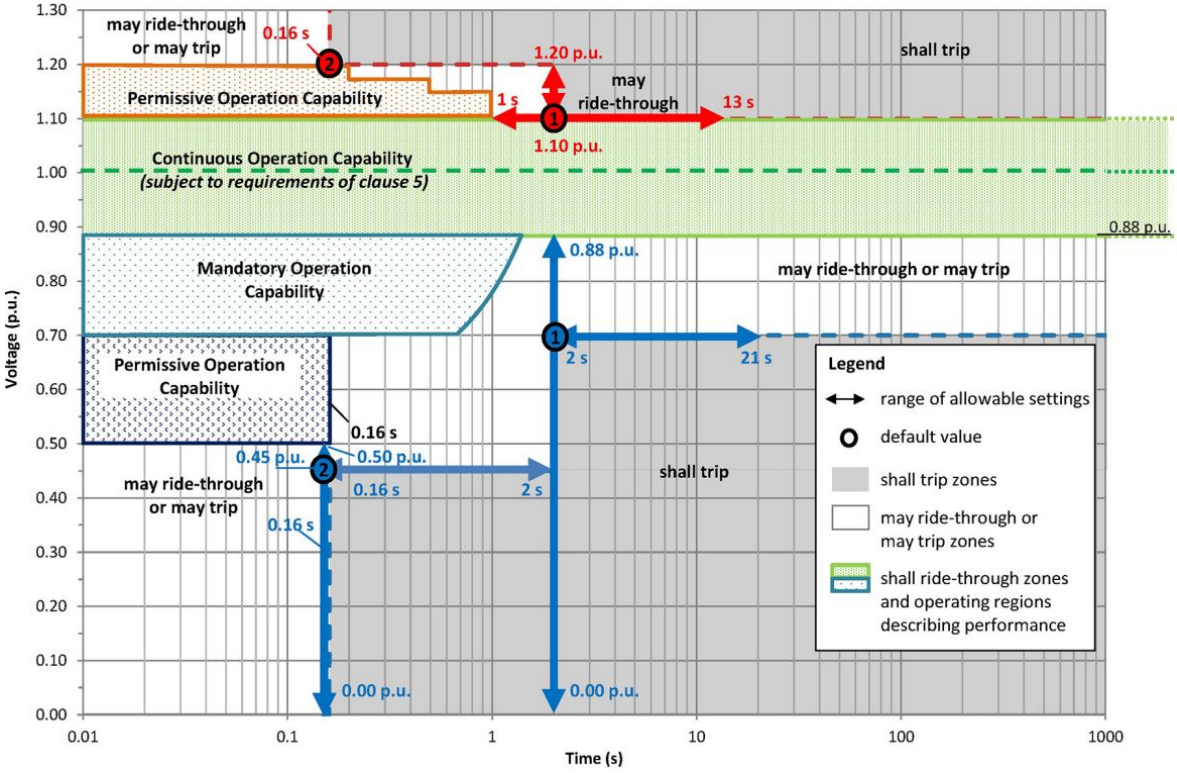

Figure 2.4: Voltage ride-through requirement and DER response to abnormal voltages for Category I DERs [2].

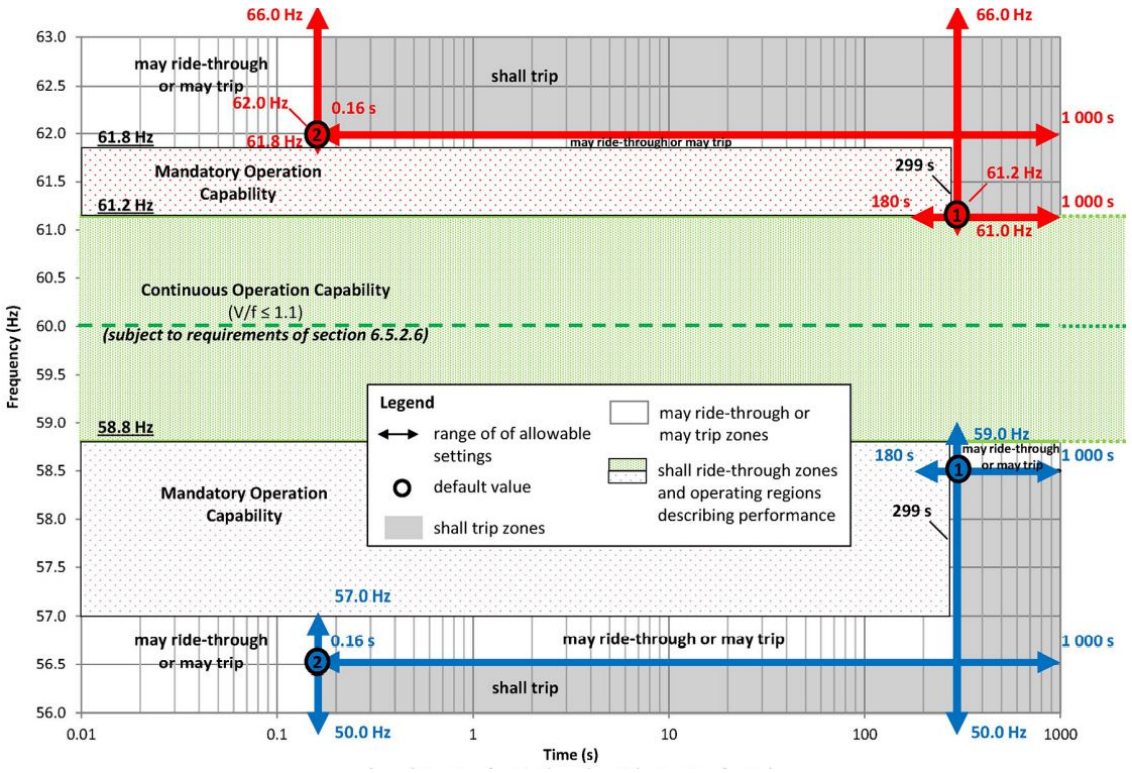

Figure 2.5: Frequency ride-through criteria for DER of abnormal operational performance Category I, Category II, and Category III, as well as DER default response to abnormal frequencies [2].

Chapter 3

Modeling of the DC/AC converter and LCL filter

The proposed BESS is shown in Figure 3.1, with the grid (black), sensors and control stage (green), and power stage (red). This work focuses on the control design of the three-phase full bridge converter, which includes the delta-connected LCL filter, the DC/DC converter, and the battery bank. The last two together are considered an ideal source of DC voltage.

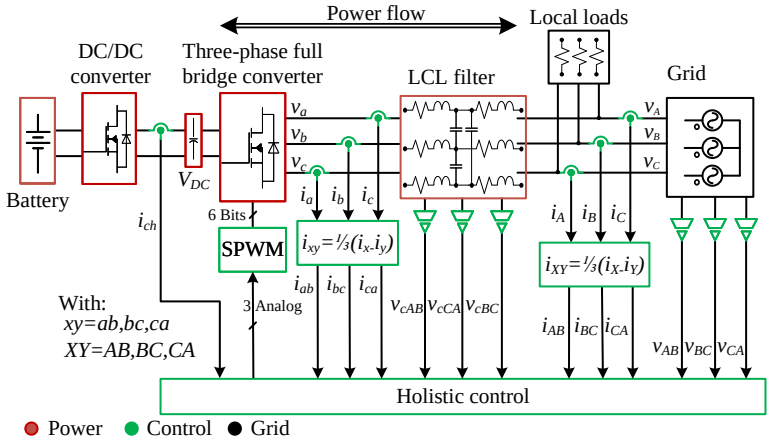

Figure 3.1: Structure of the system and control topology.

Three-phase full bridge converter topology was chosen as the DC/AC converter based on a previous work by [3]. In [3], to select the topology that best met the BESS requirements, several topologies were analyzed based on their failure mode effect analysis and figure of merits. To reduce the current high-frequency harmonics around

the switching frequency, according to the international standards such as IEEE519 and IEC 1000-3-2 for medium power applications, the PWM rectifier usually is connected to the grid through higher value filter reactors. However, the dynamic system response becomes more reduced. Then a solution is to use an LCL filter. This type of filter has lower inductances, has good ripple attenuation, and also allows to accomplish voltage source or current source control modes, in the point of common coupling (PCC) [30, 31].

This work proposes that the three-phase full bridge converter structure be able to operate along with an LCL filter using the same control scheme for all the operation modes, which are: a) islanded operation mode, b) grid-connected mode (rectifier), and c)grid-connected mode (inverter). Therefore, choosing the mode of operation is the first step for designing the LCL filter and tuning the control.

3.1 Mathematical model of the DC/AC converter

For mathematical modeling, the following assumptions are established:

1. A balanced three-phase system.
2. Line-to-line modeling is taken into consideration.
3. The analysis is based on the average mathematical model.
4. The voltage of the DC link capacitor is not regarded as a state variable. Furthermore, the magnitude of this voltage V_{DC} is always greater than the highest input voltage v_{AB}.
5. If the current i_{AB} and voltage v_{AB} are in phase, the grid-connected converter works as an inverter. Due to the operation of the DC/DC converter and the battery bank, active power, in this case, flows from V_{DC} to the grid without discharging the capacitor.
6. If the current i_{AB} is 180 degrees off from the voltage v_{AB}, the grid-connected converter operates as a rectifier. In this case, the grid provides active power to the V_{DC}, and because the DC/DC converter is charging the battery bank, the link capacitor is not overcharged.
7. Phase AB is taken into account when performing the complete analysis. Then using the first assumption as a guide, the remaining control signals are generated by shifting their phases by 120° and 240°, respectively.
8. LCL filter topology can deliver the energy corresponding to that power in both directions.
9. According to [7], a linear polynomial can be used to describe the LCL filter; as a result, to take advantage of that filter synthesis approach, which takes into

account a resistive load, the islanded mode is selected as the main mode for design.

Now, in the following section, the modeling for the three operation modes is developed.

3.1.1 Islanded mode

For this mode, the control objective is the sinusoidal voltage tracking with a constant amplitude. In Figure 3.2, the black line represents the line-to-line equivalent circuit for islanded operating mode as seen from the three-phase circuit, taking assumptions 2. and 3. into account.

The following variables will be defined using Figure 3.2:

- Currents through inductors L_{f1} as i_a, i_b, i_c.
- Currents through inductors L_{f2} as i_A, i_B, i_C.
- Delta-connected output voltages of the power converter as v_{ab}, v_{bc}, v_{ca}.
- Delta-connected grid voltages are defined as v_{AB}, v_{BC}, v_{CA}.
- Delta-connected capacitors voltage as v_{cAB}, v_{cBC}, v_{cCA}.
- Delta-connected capacitors currents as $i_{a'b'}$, $i_{b'c'}$, $i_{c'a'}$.

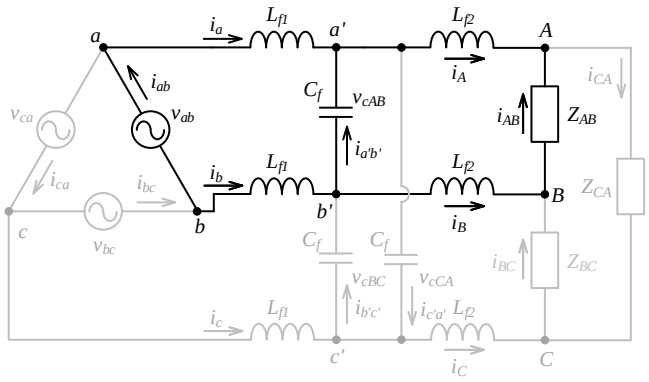

Figure 3.2: Equivalent circuit for islanded operation mode in the average model.

In addition, considering that:

$$i_{ab} = \frac{1}{3}\left(i_a - i_b\right) \tag{3.1}$$

$$i_{AB} = \frac{1}{3}\left(i_A - i_B\right) \tag{3.2}$$

$$v_{cAB} = \frac{1}{3}\left(v_{a'} - v_{b'}\right) \tag{3.3}$$

the mathematical model for the islanded mode is given in (3.4) by using the definitions of the selected variables and the circuit shown in Figure 3.2:

$$\begin{bmatrix} \dot{x}_1 \\ \dot{x}_2 \\ \dot{x}_3 \end{bmatrix} = \begin{bmatrix} 0 & 0 & \frac{-1}{3L_{f1}} \\ 0 & \frac{-Z_{AB}}{3L_{f2}} & \frac{1}{3L_{f2}} \\ \frac{3}{C_f} & \frac{-3}{C_f} & 0 \end{bmatrix} \begin{bmatrix} x_1 \\ x_2 \\ x_3 \end{bmatrix} + \begin{bmatrix} \frac{1}{3L_{f1}} \\ 0 \\ 0 \end{bmatrix} v_{ab}$$

$$\mathbf{y} = \begin{bmatrix} 0 & 0 & 1 \end{bmatrix} \begin{bmatrix} x_1 \\ x_2 \\ x_3 \end{bmatrix} \tag{3.4}$$

where $\mathbf{x} = \begin{bmatrix} i_{ab} & i_{AB} & v_{cAB} \end{bmatrix}^{\mathrm{T}}$.

3.1.2 Grid-connected (inverter) mode

For this mode, the control objective is the sinusoidal current tracking of i_{AB} in phase with v_{AB} and the same for other two phases. According to higher levels in the hierarchical control structure, the rated current i_{AB} corresponds to an active power flow from the grid-connected converter to local loads to support the RoCoF equilibrium or contribute to the grid in order to achieve peak shaving. To describe the procedure to obtain the mathematical model, let us consider the circuit of Figure 3.3, where local loads specified by resistances are included in the grid-connected (inverter) mode. Therefore $i_{AB} = i_{AB-BESS}$.

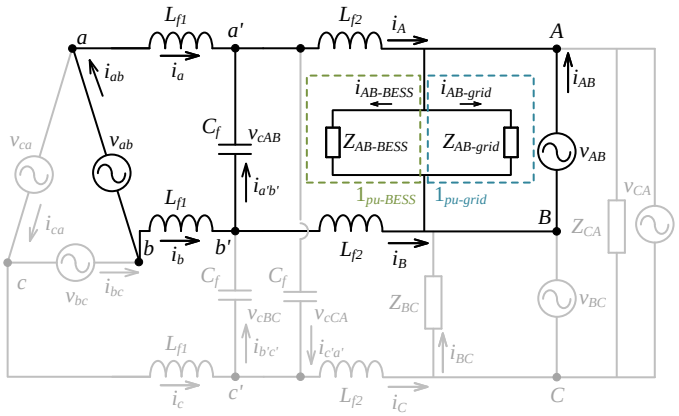

Figure 3.3: Equivalent average circuit for grid-connected (inverter) mode.

Figure 3.3 illustrates that while the BESS has a $1_{\mathrm{pu}-BESS}$ power delivery capability, the grid has a $1_{\mathrm{pu}-grid}$ power delivery capability. The current reference for the BESS will always be zero as long as the load is within the grid's capacity. The BESS additionally

supplies power to the load when the load exceeds the grid's capacity, whereas the power does not exceed the BESS's capacity. An i^*_{AB} current should be calculated as a reference and supplied by the BESS through L_{f2} in order to deliver that power. The aforementioned it is considered to obtain the mathematical model.

Considering the circuit shown in Figure 3.3, the mathematical model is as follows:

$$\begin{bmatrix} \dot{x}_1 \\ \dot{x}_2 \\ \dot{x}_3 \end{bmatrix} = \begin{bmatrix} 0 & 0 & \frac{-1}{3L_{f1}} \\ 0 & \frac{-Z_{AB-BESS}}{3L_{f2}} & \frac{1}{3L_{f2}} \\ \frac{3}{C_f} & \frac{-3}{C_f} & 0 \end{bmatrix} \begin{bmatrix} x_1 \\ x_2 \\ x_3 \end{bmatrix} + \begin{bmatrix} \frac{1}{3L_{f1}} \\ 0 \\ 0 \end{bmatrix} v_{ab} \tag{3.5}$$

$$\mathbf{y} = \begin{bmatrix} 0 & 1 & 0 \end{bmatrix} \begin{bmatrix} x_1 \\ x_2 \\ x_3 \end{bmatrix}$$

3.1.3 Grid-connected (rectifier) mode

The control objective is a sinusoidal current tracking i_{AB} shifted 180° from main voltage v_{AB} and the same for other two phases. To examine this mode, let us just focus at the equivalent average circuit in Figure 3.4. As can be seen, the load on the DC side is defined as Z_{ch}. This load represents the consumes of the battery bank active power to charge it until the state of charge (SOC) reaches 100%. It is important to point out that the current i_{ch} is required by a DC/DC stage, which is outside the scope of this work. The relevance of this contribution comes from the fact that although the voltage in C_{DC} is not considered a state variable, one-third of the power demand will be fulfilled by the current i_{AB}, which is 180 degrees off from v_{AB} and has the necessary amplitude to maintain regulated V_{DC}.

The mathematical model of the circuit shown in Figure 3.4 is:

$$\begin{bmatrix} \dot{x}_1 \\ \dot{x}_2 \\ \dot{x}_3 \end{bmatrix} = \begin{bmatrix} 0 & 0 & \frac{-1}{3L_{f1}} \\ 0 & 0 & \frac{1}{3L_{f2}} \\ \frac{3}{C_f} & \frac{-3}{C_f} & 0 \end{bmatrix} \begin{bmatrix} x_1 \\ x_2 \\ x_3 \end{bmatrix} + \begin{bmatrix} \frac{1}{3L_{f1}} \\ 0 \\ 0 \end{bmatrix} v_{ab} + \begin{bmatrix} 0 \\ \frac{-1}{3L_{f2}} \\ 0 \end{bmatrix} v_{AB} \tag{3.6}$$

$$\mathbf{y} = \begin{bmatrix} 0 & 1 & 0 \end{bmatrix} \begin{bmatrix} x_1 \\ x_2 \\ x_3 \end{bmatrix}$$

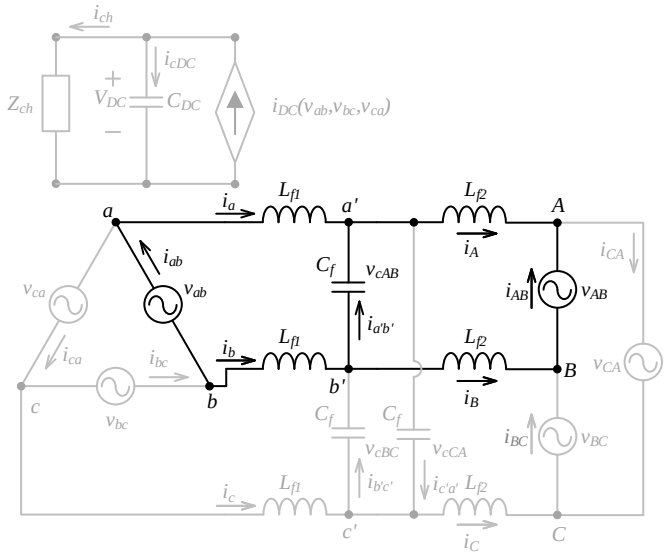

Figure 3.4: Equivalent average circuit used for rectifier operation analysis.

3.2 Butterworth LCL Filter Design

The LCL filter is responsible for preserving the electrical requirements according to the standard IEEE 1547-2018 [2]. Furthermore, it is important to point out that this filter determines the dynamic during transients or mode changes. According to the Butterworth polynomial, which was originally defined in [32], the LCL filter was designed.

The islanded operation mode at rated active power is considered for the LCL filter design. This selection was made because the method used in [7] treats the rated load as a resistive load. This selection is valid for any other mode of operation considering the same maximum active power.

The Butterworth filter synthesis technique described by [7] is used in this thesis to benefit from its straightforwardness, standardized design, and applicability to communications or grid-connected filters. Before the designing of the LCL filter, the following input parameters are established using Sinusoidal Pulse Width Modulation (SPWM) as the modulation method:

1. Switching frequency $f_{sw} = 12,060$ Hz; $\omega_{sw} = 75.7$ krad/s.
2. Amplitude and frequency modulation indexes; $m_a = 0.85$ and $m_f = 201$, respectively.
3. First relevant harmonic amplitude $h_{199(11940\text{Hz})} = 0.289$.
4. The double-edge naturally sampled PWM for the three-phase full-bridge converter

is used for this work. As a result, the first carrier harmonic group has the more significant harmonic at $m_f - 2 = 199$, being $\omega_{\text{h}199} = 75.02$ krad/s.

5. According to IEEE-1159, THD voltage at the PCC should be lower than 3 %, to fulfill this requirement, an attenuation for the first relevant harmonic was proposed of $|G(jw)_{\text{h}199}| = -32$ dB.

6. The rated load value $Z_{load} = Z_{AB} = 70\ \Omega$ is selected for the rated power. It is important to see that this technique considers a resistive load; it means active power transference. Of course, the BESS works under different modes and operating conditions, and the filter should be able to transfer the necessary power in both directions.

The transfer function of the Butterworth filter is given by [7]:

$$G_{\text{BT}}(s) = \frac{1}{Q(s)} \tag{3.7}$$

where the normalized Butterworth polynomial is denoted by $Q(s)$. The first four normalized polynomials are shown in Table 3.1.

Table 3.1: Normalized Butterworth polynomials [7].

Filter order	Polynomial $Q(s)$
1.	$s + 1$
2.	$s^2 + 1.4142s + 1$
3.	$s^3 + 2.000s^2 + 2.0000s + 1$
4.	$s^4 + 2.6131s^3 + 3.4142s^2 + 2.6131s + 1$

The polynomial $Q(s)$ and the cutoff frequency ω_c are two additional parameters required for the LCL filter design. Given that there are three energy storage elements, the third-order polynomial has been chosen. The third-order Butterworth filter transfer function can be divided into a simple pole and two complex conjugate poles. The following shows the denormalized transfer function in terms of ω_c.

$$G_{\text{BT}}(s) = \frac{\omega_c}{s + \omega_c} \frac{\omega_c^2}{s^2 + \omega_c s + \omega_c^2} \tag{3.8}$$

The magnitude frequency response equation for (3.8) when $s = j\omega$ is then given as follows:

$$|G\left(j\omega\right)_{h199}| = 20\log\left(\frac{\omega_c}{\sqrt{\omega_c^2+\omega_{h_{199}}^2}}\frac{\omega_c^2}{\sqrt{\left(\omega_c^2-\omega_{h_{199}}^2\right)^2+(\omega_c\omega_{h_{199}})^2}}\right) \tag{3.9}$$

Solving ω_c from equation (3.9) and given that $G\left(j\omega\right)_{h_{199}} = -32\,\text{dB}$ of attenuation for the first relevant harmonic $\text{h}_{199(11940)}$, ω_c is calculated as follows:

$$\omega_c = -\frac{(-1)^{5/6}\omega_{h_{199}}10^{G(jw)_{h199}/60}}{\sqrt[6]{10^{G(jw)_{h199}/10}-1}} \tag{3.10}$$

With the frequency of $\omega_c = 21.97\,\text{krad/s}$, according to [7], the reference passive elements L_r and C_r can be calculated as follows:

$$L_r = \frac{Z_{load}}{\omega_c} = 3.18\,\text{mH} \tag{3.11}$$

$$C_r = \frac{1}{Z_{load}\omega_c} = 0.65\,\mu\text{F} \tag{3.12}$$

with $Z_{load} = 70\,\Omega$.

Once L_r and C_r are calculated the LCL filter elements are:

$$L_{f1} = \frac{1.5}{3L_r} = 1.59\,\text{mH} \tag{3.13}$$

$$L_{f2} = \frac{0.5}{3L_r} = 530.95\,\mu\text{H} \tag{3.14}$$

$$C_f = 3\times 1.3333C_r = 2.60\,\mu\text{F} \tag{3.15}$$

The denormalized transfer function of the Butterworth filter is given by:

$$G_{\text{BT}}(s) = \frac{v_{AB}(s)}{v_{ab}(s)} = \frac{Z_{load}}{L_{f1}C_fL_{f2}s^3 + L_{f1}C_fZ_{load}s^2 + (L_{f1}+L_{f2})\,s + Z_{load}} \tag{3.16}$$

Figure 3.5 shows the third-order filter Bode diagram considering the desired attenuation. The proposed wideband, which contains the candidate eigenvalues for the closed-loop system, is also shown in Figure 3.5.

Once the filter has been created for the islanded operation mode, it can also be used in the grid-connected inverter and grid-connected rectifier modes. The following section makes this statement completely clear.

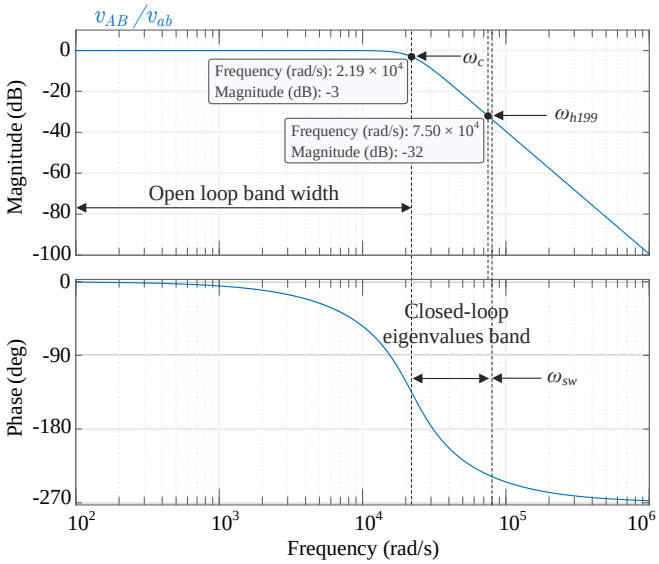

Figure 3.5: $G_{\mathrm{BT}}(s)$ bode diagram in islanded-mode.

Chapter 4

Holistic control scheme design

For controlling the two specific operating modes (current and voltage) individually, many control strategies have been proposed [33]. The difficulty is that the two operating modes follow different dynamic and steady-state properties, which may result in an abrupt transition mode [34].

The hybrid technique [35] is one method for managing both operating modes. A common alternative is the hybrid voltage and current mode control, which uses two different sets of controllers. In the grid-tied mode, one set of controllers controls the inverter as a current source, while in the islanded mode, the other set of controllers regulates it as a voltage source. As a result, the level 0 and level 1 of the hierarchical control can be seen in Figure (4.1).

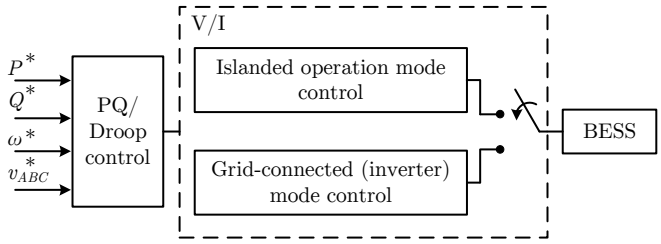

Figure 4.1: Hybrid control architecture.

Figure (4.2) shows an example of a typical hybrid control implementation practice given in [3]. Two independent PI controllers are used, the first one on the right side is for the grid-connected mode as a current source, where P and Q are set as references, and the another one on the left side is for the island mode as a voltage source, where the voltage is set as a reference. Both controllers are implemented employing the park transformations of the three-phase voltages and currents.

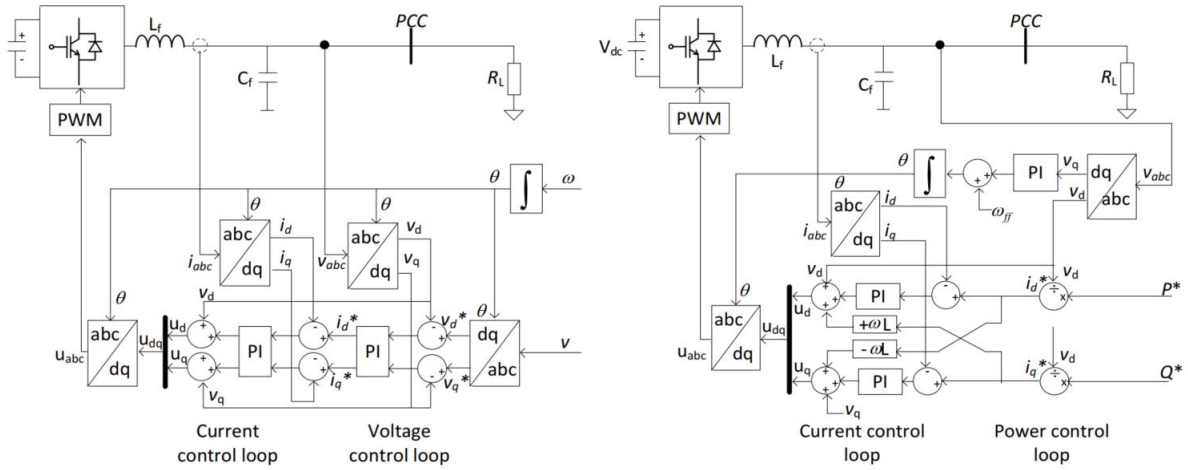

Figure 4.2: Typical hybrid control [3]

4.1 Classical unified control

The so-called unified control, which enables grid-connected and islanded operations in one single control architecture, is the most recent strategy to address the issues with the previously described systems. This method is based on combining and slightly altering the control structures for V/f and PQ of Figure 4.1 with droop controls characteristics to create one control architecture, as illustrated in Figure 4.3. A BESS and DER should also use the same circuit designs, feedback signals, and transducers for the two modes of operation from the perspectives of product development and production [36].

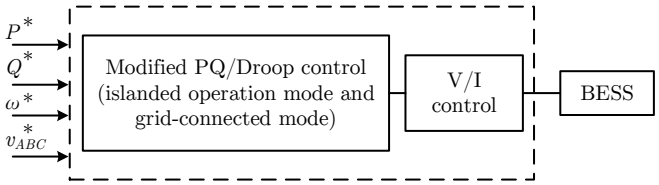

Figure 4.3: Unified control architecture.

4.2 Conceptualization

The conceptualization of the thesis contribution begins with the proposed unified control architecture, shown in Figure 4.4. The operation modes of interest are; islanded

operation mode, the grid-connected mode as an inverter, and the grid-connected mode as a rectifier. In the first mode of operation, the output is controlled in voltage mode, whilst in the other two modes the output is controlled in current mode.

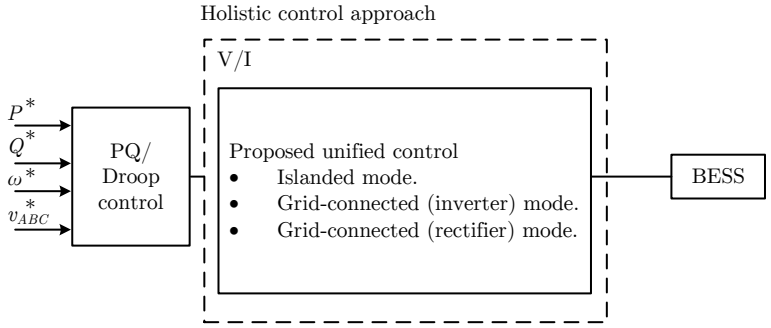

Figure 4.4: Proposed unified control architecture.

The proposal is based on using a single controller for all the operation modes, designing the closed-loop eigenvalue locus strategically regarding the open-loop eigenvalue locus for preserving the natural Butterworth behavior given to the system. This unified control architecture was presented in [37] as a "Holistic control approach", as shown in Figure 4.4. Figure 4.5 shows how holistic control is included in the typical herarchical control, it is assumed that in level 0 of the control; all the states variables are available, even when those are not shown.

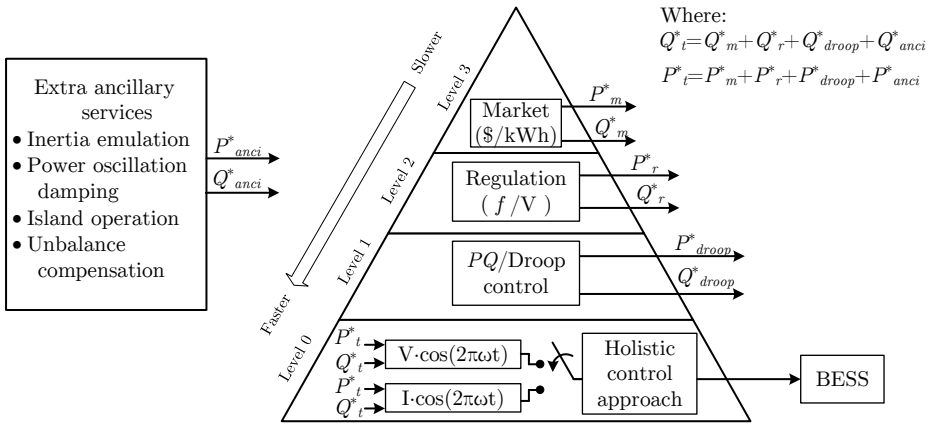

Figure 4.5: Proposed holistic control scheme.

It is necessary to make a distinction between the following operation modes, grid-connected (inverter) control and grid-connected (rectifier). This consists in that as an inverter, the current is in phase with the voltage in order to inject power into the

electrical power system, while in the rectifier mode, the current is out of phase by 180° in order to recharge the BESS batteries, as can be seen in Figure 4.6.

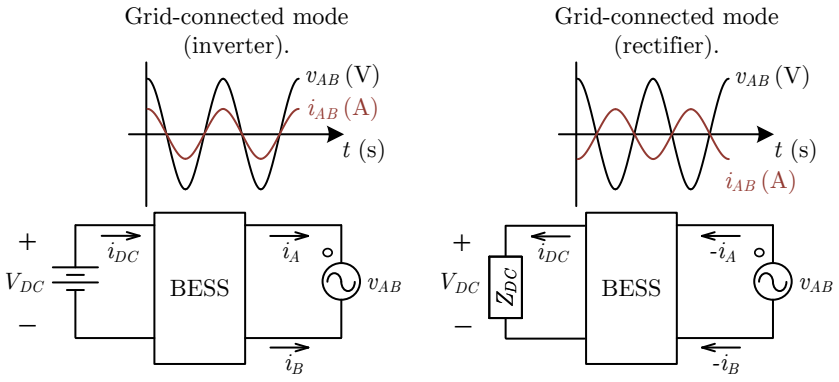

Figure 4.6: Block diagram of the controller.

In the grid-connected mode as a rectifier, it is also required to control the DC bus voltage, and this is accomplished from the estimation of the current that the rectifier must absorb in the following way.

The power balance between the AC and DC sides to calculate the current references is considered. Then the input power P_{AC} is described by (4.1), and the output power P_{DC} is described by (4.2).

$$P_{AC} = \frac{v_{AB_{peak}} i_{AB_{peak}}}{2} + \frac{v_{BC_{peak}} i_{BC_{peak}}}{2} + \frac{v_{CA_{peak}} i_{CA_{peak}}}{2} \tag{4.1}$$

$$P_{DC} = V^*_{DC} i_{DC} \tag{4.2}$$

where $v_{AB_{peak}}$, $v_{BC_{peak}}$, and $v_{CA_{peak}}$ are the three peak grid voltage line-to-line, V^*_{DC} is the desired DC bus voltage, and i_{DC} is the load current. Also, as can be observed from Figure 3.1.

The three peak currents $i^*_{AB_{peak}}$, $i^*_{BC_{peak}}$, and $i^*_{CA_{peak}}$, are obtained as shown (4.3),(4.4), and (4.5), respectively.

$$i^*_{AB_{peak}} = \left(\frac{1}{3} V^*_{DC} i_{DC}\right) \frac{2}{v_{AB_{peak}}} \tag{4.3}$$

$$i^*_{BC_{peak}} = \left(\frac{1}{3} V^*_{DC} i_{DC}\right) \frac{2}{v_{BC_{peak}}} \tag{4.4}$$

$$i^*_{CA_{peak}} = \left(\frac{1}{3} V^*_{DC} i_{DC}\right) \frac{2}{v_{CA_{peak}}} \tag{4.5}$$

Given $i^*_{AB_{peak}}$, $i^*_{BC_{peak}}$, and $i^*_{CA_{peak}}$, the instantaneous currents references i^*_{AB}, i^*_{BC}, and i^*_{CA}, respectively, are computed with (4.6),(4.7), and (4.8) where $f = 60$ Hz and

the reference must be in phase Φ_{AB} with the line-to-line voltage v_{AB}, to approach a unitary power factor and the same for the other two phases.

$$i^*_{AB} = i^*_{AB_{peak}} \sin_{AB}(2\pi ft + \Phi_{AB}) \tag{4.6}$$

$$i^*_{BC} = i^*_{BC_{peak}} \sin_{BC}(2\pi ft + \Phi_{BC}) \tag{4.7}$$

$$i^*_{CA} = i^*_{CA_{peak}} \sin_{CA}(2\pi ft + \Phi_{CA}) \tag{4.8}$$

Once each mode of operation and how it operates have been established, the control design is addressed. In this thesis work, two different designs to tuning the controller gains.

The first design addresses the problem from a holistic viewpoint to achieve a seamless transition among three different operation modes. It is possible to provide seamless overshoots during transient responses by choosing a Butterworth behavior from the LCL filter to the control design. This specific behavior is preserved by tuning the feedback-controller gains while the transient-response speed is improved by increasing the bandwidth. The control design takes advantage of the principal attributes of a low-order Butterworth filter: maximally flat in the passband in the amplitude response, fast response and small overshoots [38], good relationship between attenuation and phase response [39], and there is not passband ripple [40]. This holistic control has the advantage of using a single set of controller gains the three operation modes. In contrast to conventional multi-loop controllers, this controller uses just one feedback loop, which is a significant additional feature [27]. The first design uses state feedback with an integrator, with the integrator tuned independently. The state feedback is tuned using a Butterworth polynomial as was reported in [37].

The second design considers the gains of the integrator and state feedback concatenated in the same Butterworth polynomial with the aim of reducing energy consumption when transitions from one operation mode to another occur. Although the tuning processes for the two tuning methods differ slightly, as this thesis will show, the impact on energy consumption is remarkable.

4.3 First tuning for the holistic control

Table 4.1 lists the open-loop matrices with the values on the LCL filter given in (3.13) - (3.15), and eigenvalues.

where:

Table 4.1: Open-loop matrixes and eigenvalues.

Operation mode	State matrix	Input matrix	Output matrix	Eigenvalues (rad/s)
Islanded mode (ism)	$\mathbf{A}_{\text{ism}}$	$\mathbf{B}_{\text{ism}}$	$\mathbf{C}_{\text{ism}}$	$\alpha_{1\_\text{ism}} = -15.70 \times 10^3$ $\alpha_{2,3\_\text{ism}} = (-7.85 \pm j13.6) \times 10^3$
Grid-connected (inverter) mode (gci)	$\mathbf{A}_{\text{gci}}$	$\mathbf{B}_{\text{gci}}$	$\mathbf{C}_{\text{gci}}$	$\alpha_{1\_\text{gci}} = -15.70 \times 10^3$ $\alpha_{2,3\_\text{gci}} = (-7.85 \pm j13.6) \times 10^3$
Grid-connected (rectifier) mode (gcr)	$\mathbf{A}_{\text{gcr}}$	$\mathbf{B}_{\text{gcr\_1}}$ $\mathbf{B}_{\text{gcr\_2}}$	$\mathbf{C}_{\text{gcr}}$	$\alpha_{1\_\text{gcr}} = 0$ $\alpha_{2,3\_\text{gcr}} = (\pm j22.21) \times 10^3$

$$\mathbf{A}_{\text{ism}} = \begin{bmatrix} 0 & 0 & -1,515 \\ 0 & -31.41 \times 10^3 & 4,545 \\ 81.43 \times 10^3 & -81.43 \times 10^3 & 0 \end{bmatrix} \tag{4.9}$$

$$\mathbf{B}_{\text{ism}} = \begin{bmatrix} 1,515 \\ 0 \\ 0 \end{bmatrix} \tag{4.10}$$

$$\mathbf{C}_{\text{ism}} = \begin{bmatrix} 0 & 0 & 1 \end{bmatrix} \tag{4.11}$$

$$\mathbf{A}_{\text{gci}} = \begin{bmatrix} 0 & 0 & -1,515 \\ 0 & -31.41 \times 10^3 & 4,545 \\ 81.43 \times 10^3 & -81.43 \times 10^3 & 0 \end{bmatrix} \tag{4.12}$$

$$\mathbf{B}_{\text{gci}} = \begin{bmatrix} 1,515 \\ 0 \\ 0 \end{bmatrix} \tag{4.13}$$

$$\mathbf{C}_{\text{gci}} = \begin{bmatrix} 0 & 1 & 0 \end{bmatrix} \tag{4.14}$$

$$\mathbf{A}_{\text{gcr}} = \begin{bmatrix} 0 & 0 & -1,515 \\ 0 & 0 & 4,545 \\ 81.43 \times 10^3 & -81.43 \times 10^3 & 0 \end{bmatrix} \tag{4.15}$$

$$\mathbf{B}_{\text{gcr\_1}} = \begin{bmatrix} 1,515 \\ 0 \\ 0 \end{bmatrix} \tag{4.16}$$

$$\mathbf{B}_{\text{gcr\_2}} = \begin{bmatrix} 0 \\ -4.5451 \\ 0 \end{bmatrix} \tag{4.17}$$

$$\mathbf{C}_{\text{gcr}} = \begin{bmatrix} 0 & 1 & 0 \end{bmatrix} \tag{4.18}$$

The eigenvalues in the inverter as islanded and grid-connected (inverter) modes are the same, as can be seen. It is also crucial to note that $|\alpha_{1\_\text{im}}|$ and $|\alpha_{1\_\text{gci}}|$ coincides with the bandwidth similarly to $|\alpha_{2,3\_\text{im}}|$ and $|\alpha_{2,3\_\text{gci}}|$.

The controller proposal is based on state feedback plus integral action after the prior observation has been made. The block diagram of the proposal used for the islanded mode is shown in Figure 4.7.

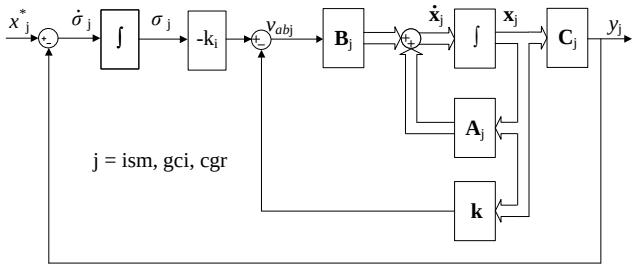

Figure 4.7: Block diagram of the controller.

The integrator ensures the system's robustness against constant disturbances, while $\mathbf{k}_{\text{mi}}$ modifies the system performance according to [41].

To design the controller, let us consider the islanded mode let us present an expanded model taking into account the islanded mode as follows:

$$\begin{bmatrix} \dot{\mathbf{x}} \\ \dot{\sigma}_{\text{ism}} \end{bmatrix} = \begin{bmatrix} \mathbf{A}_{\text{ism}} & \mathbf{0} \\ -\mathbf{C}_{\text{ism}} & 0 \end{bmatrix} \begin{bmatrix} \mathbf{x} \\ \sigma_{\text{ism}} \end{bmatrix} + \begin{bmatrix} \mathbf{B}_{\text{ism}} \\ 0 \end{bmatrix} v_{ab_{\text{ism}}} + \begin{bmatrix} \mathbf{0} \\ 1 \end{bmatrix} x_3^* \tag{4.19}$$

where:

$\mathbf{x}$ is the state vector.

$\mathbf{A}_{\text{ism}}$, $\mathbf{B}_{\text{ism}}$, and $\mathbf{C}_{\text{ism}}$ are the matrices of state, input and output, respectively.

$\dot{\sigma}_{\text{ism}}$ is the error between the voltage reference and measured voltage.

$v_{ab_{\text{ism}}}$ is the control law which modifies the inverter output.

$\mathbf{k}$ is the gain vector.

k_i is the gain of the integral action.

Considering the control law as:

$$v_{ab} = \begin{bmatrix} \mathbf{k} & \text{k}_\text{i} \end{bmatrix} \begin{bmatrix} \mathbf{x} \\ \sigma_{\text{ism}} \end{bmatrix} \tag{4.20}$$

The closed-loop system is:

$$\begin{bmatrix} \dot{\mathbf{x}} \\ \dot{\sigma}_{\text{ism}} \end{bmatrix} = \begin{bmatrix} \mathbf{A}_{\text{ism}} - \mathbf{B}_{\text{ism}}\mathbf{k} & \mathbf{B}_{\text{ism}}\text{k}_\text{i} \\ -\mathbf{C}_{\text{ism}} & 0 \end{bmatrix} \begin{bmatrix} \mathbf{x} \\ \sigma_{\text{ism}} \end{bmatrix} + \begin{bmatrix} \mathbf{0} \\ 1 \end{bmatrix} x_3^*$$
$$\begin{bmatrix} \dot{\mathbf{x}} \\ \dot{\sigma}_{\text{ism}} \end{bmatrix} = \hat{\mathbf{A}} \begin{bmatrix} \mathbf{x} \\ \sigma_{\text{ism}} \end{bmatrix} + \begin{bmatrix} \mathbf{0} \\ 1 \end{bmatrix} x_3^* \tag{4.21}$$

Theoretically, the linear system is asymptotical and exponentially stable if the matrix $\hat{\mathbf{A}}$ is Hurwitz. However, this theoretical statement is restricted by the physical limitations of the system. Therefore, let us present the following straightforward formulation for tuning the control scheme. The open-loop LCL-filter bandwidth, which is defined by 15.70 krad/s, indicates the lower limit for estimating the closed-loop eigenvalues. Any eigenvalue below that threshold will use the energy inefficiently because the system would tend to be slower than its own dynamic, which does not make sense. The switching frequency of 77.5 krad/s specifies the upper limit for calculating the closed-loop eigenvalues. Any eigenvalue beyond that limit will be irrelevant because the system could not follow those fast dynamics.

Following the establishment of the preceding limits, the open-loop eigenvalues for the state feedback are multiplied by a constant M. To put it in its proper place, the multiplicand $\omega_c \times M$ is used to obtain the closed-loop eigenvalue introduced by the integral action. The proposed closed-loop location of the eigenvalues in this work is $M = 2$ (which fulfills the prior limits considerations).

$$\begin{aligned} \alpha_{\text{ismcl(states feedback)}} &= M \times (\alpha_{1\text{ism}}, \alpha_{2,3,\text{ism}}) \\ \alpha_{\text{ismcl(integral action)}} &= \frac{1}{M} \times \omega_c \end{aligned} \tag{4.22}$$

Then, the tuning constants of (4.20), by using Ackerman formula,

$$\begin{aligned} \mathbf{k} &= \begin{bmatrix} -5.18 & 25.92 & 6.00 \end{bmatrix} \\ \text{k}_\text{i} &= -62.8319 \times 10^3 \end{aligned} \tag{4.23}$$

Therefore, the control law for the islanded mode has the form:

$$\begin{aligned} v_{ab\text{ism}} &= \mathrm{k}_1 x_1 + \mathrm{k}_2 x_2 + \mathrm{k}_3 x_3 + \mathrm{k}_\mathrm{i} \sigma_\text{ism} \\ \dot{\sigma}_\text{ism} &= x_3^* - x_3 \end{aligned} \tag{4.24}$$

Considering the same tuning constants, the controllers for the other modes follow the holistic control concept as follows:

$$\begin{aligned} v_{ab\text{gci}} &= \mathrm{k}_1 x_1 + \mathrm{k}_2 x_2 + \mathrm{k}_3 x_3 + \mathrm{k}_\mathrm{i} \sigma_\text{gci} \\ \dot{\sigma}_\text{gci} &= x_2^* - x_2 \end{aligned} \tag{4.25}$$

$$\begin{aligned} v_{ab\text{gcr}} &= \mathrm{k}_1 x_1 + \mathrm{k}_2 x_2 + \mathrm{k}_3 x_3 + \mathrm{k}_\mathrm{i} \sigma_\text{gcr} \\ \dot{\sigma}_\text{gcr} &= x_2^* - x_2 \end{aligned} \tag{4.26}$$

The matrices $\hat{\mathbf{A}}$ and the closed-loop eigenvalues for each mode are summarized in Table 4.2. As can be seen, every eigenvalue has a negative real part and satisfies the application-defined physical limits.

Table 4.2: Closed-loop matrixes and eigenvalues.

Operation mode	Closed-loop matrix	Eigenvalues (rad/s)
Islanded-mode (ism)	$\hat{\mathbf{A}}_\text{ism}$	$\alpha_{1\_\text{ism\_cl}} = -7.85 \times 10^3$ $\alpha_{2,3\_\text{ism\_cl}} = (-15.70 \pm j27.20) \times 10^3$ $\alpha_{4\_\text{ism\_cl}} = -31.41 \times 10^3$
Grid-connected (inverter) mode (gci)	$\hat{\mathbf{A}}_\text{gci}$	$\alpha_{1\_\text{gci\_cl}} = -30.19 \times 10^3$ $\alpha_{2,3\_\text{gci\_cl}} = (-19.75 \pm j28.56) \times 10^3$ $\alpha_{4\_\text{gci\_cl}} = -966.92$
Grid-connected (rectifier) mode (gcr)	$\hat{\mathbf{A}}_\text{gcr}$	$\alpha_{1,2\_\text{gcr\_cl}} = (-13.53 \pm j26.06) \times 10^3$ $\alpha_{3,4\_\text{gcr\_cl}} = (-6.09 \pm j1.91) \times 10^3$

where:

$$\hat{\mathbf{A}}_\text{ism} = \begin{bmatrix} -39.27 & 7.85 & -10.60 & 95193 \\ 0 & -31.416 & 4.54 & 0 \\ 81.43 & -81.43 & 0 & 0 \\ 0 & 0 & -0.001 & 0 \end{bmatrix} \times 10^3 \tag{4.27}$$

$$\hat{\mathbf{A}}_{\text{gci}} = \begin{bmatrix} -39.27 & 7.85 & -10.60 & 95193 \\ 0 & -31.416 & 4.54 & 0 \\ 81.43 & -81.43 & 0 & 0 \\ 0 & -0.001 & 0 & 0 \end{bmatrix} \times 10^3 \tag{4.28}$$

$$\hat{\mathbf{A}}_{\text{gcr}} = \begin{bmatrix} -39.27 & 7.85 & -10.60 & 95193 \\ 0 & 0 & 4.54 & 0 \\ 81.43 & -81.43 & 0 & 0 \\ 0 & -0.001 & 0 & 0 \end{bmatrix} \times 10^3 \tag{4.29}$$

4.4 Second tuning for the holistic control: improved tuning

In this improved design, it was considered that a complete Butterworth dynamic should be also maintained for the integral action. Therefore the following procedure was employed.

The open-loop eigenvalues of the three operation modes, which are listed in Table 4.3, must be determined before beginning the procedure.

Table 4.3: Open-loop matrices and eigenvalues.

Operation mode	State matrix	Input matrix	Output matrix	Eigenvalues (rad/s)
Islanded mode (ism)	$\mathbf{A}_{\text{ism}}$	$\mathbf{B}_{\text{ism}}$	$\mathbf{C}_{\text{ism}}$	$\alpha_{1\_\text{ism}} = -21.97 \times 10^3$ $\alpha_{2,3\_\text{ism}} = (-10.98 \pm \text{j}19.03) \times 10^3$
Grid-connected (inverter) mode (gci)	$\mathbf{A}_{\text{gci}}$	$\mathbf{B}_{\text{gci}}$	$\mathbf{C}_{\text{gci}}$	$\alpha_{1\_\text{gci}} = -21.97 \times 10^3$ $\alpha_{2,3\_\text{gci}} = (-10.98 \pm j19.03) \times 10^3$
Grid-connected (rectifier) mode (gcr)	$\mathbf{A}_{\text{gcr}}$	$\mathbf{B}_{\text{gcr\_1}}$ $\mathbf{B}_{\text{gcr\_2}}$	$\mathbf{C}_{\text{gcr}}$	$\alpha_{1\_\text{gcr}} = 0$ $\alpha_{2,3\_\text{gcr}} = (\pm j31.10) \times 10^3$

In the same way that the first approach, it is important to note that in Table 4.3, the eigenvalues are the same in islanded and grid-connected (inverter) modes. Furthermore,

$|\alpha_{1\_ism}|$ and $|\alpha_{1\_gci}|$ correspond to bandwidth in the same way as $|\alpha_{2,3\_ism}|$ and $|\alpha_{2,3\_gci}|$ do, implying that the grid-connected mode inverter is also Butterworth. The grid-connected mode rectifier has distinct eigenvalues, as seen in the counterpart.

The same control proposal presented in Figure 4.8 is used. The difference between this design concerning the previous consists of considering a Butterworth polynomial that includes the integral action, this implies that the degree of the polynomial will increase by one. This change will improve the closed-loop tuning and reduce the energy consumption of the system when mode changes and load transients occur.

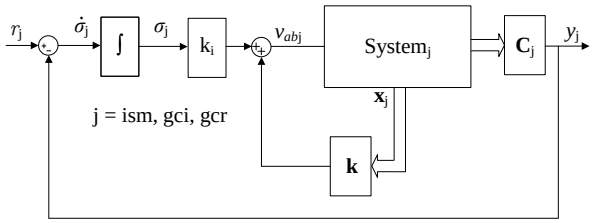

Figure 4.8: Block diagram of the controller.

For islanded operation mode, the closed-loop system is:

$$\begin{bmatrix} \dot{\mathbf{x}} \\ \dot{\sigma}_{\text{ism}} \end{bmatrix} = \begin{bmatrix} \mathbf{A}_{\text{ism}} - \mathbf{B}_{\text{ism}}\mathbf{k} & \mathbf{B}_{\text{ism}}\mathrm{k_i} \\ -\mathbf{C}_{\text{ism}} & 0 \end{bmatrix} \begin{bmatrix} \mathbf{x} \\ \sigma_{\text{ism}} \end{bmatrix} + \begin{bmatrix} \mathbf{0} \\ 1 \end{bmatrix} r \tag{4.30}$$

or

$$\begin{bmatrix} \dot{\mathbf{x}} \\ \dot{\sigma}_{\text{ism}} \end{bmatrix} = \hat{\mathbf{A}} \begin{bmatrix} \mathbf{x} \\ \sigma_{\text{ism}} \end{bmatrix} + \begin{bmatrix} \mathbf{0} \\ 1 \end{bmatrix} r \tag{4.31}$$

where:

- $\mathbf{x}$ is the state vector.
- r is the reference of the controlled output.
- $\mathbf{A}_{\text{ism}}$, $\mathbf{B}_{\text{ism}}$, and $\mathbf{C}_{\text{ism}}$ are the state, input and output matrices, respectively.
- $\dot{\sigma}_{\text{ism}}$ is the error between the voltage reference and measured voltage.
- $v_{ab_{\text{ism}}}$ is the control law which modifies the inverter output.
- $\mathbf{k}$ are the gain vector.
- $\mathrm{k_i}$ is the gain of the integral action.

As already proved in the first approach, the system is controllable and the limits to place the closed-loop poles are given by the open-loop LCL filter bandwidth and the switching frequency as $\omega_c = 21.97$ krad/s and $\omega_{sw} = 75.7$ krad/s, respectively.

In comparison to [37] and the first design, the eigenvalues position will be chosen to maintain the fourth-order Butterworth filter dynamic.

According to [42], the poles of the transfer function will be distributed in a normalized form in the left half of a unit circle centered at the origin of the complex plane based on the normalized Butterworth polynomials displayed in Figure 4.9 and Table 3.1. Since an integrator is included in the closed control loop, it is crucial to note that the system order will increase by one.

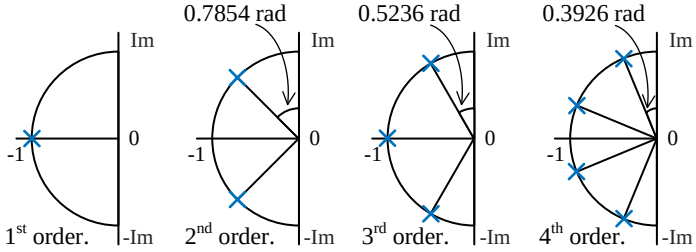

Figure 4.9: Butterworth root locus.

The factor M for tuning has been introduced, which multiplies the $|\omega_c|$, which is the magnitude of the open-loop wideband, to get ω_{cl}, which is the frequency of the closed-loop wideband, in order to determine the new position of the poles of the augmented fourth-order system.

The value of the factor M should be chosen considering the physical limitations of the system given before. In this work, $M = 1.8$ for fulfilling the limits previously established; therefore, we can calculate the proposed closed-loop eigenvalues in the polar form as:

$$\alpha_{\mathrm{i\_ism\_cl}} = |\omega_c|\, M \angle \left(\frac{\pi}{2n_{\mathrm{ext}}}(2\mathrm{i} - 1) + \frac{\pi}{2} \right) \text{ for i=1,2,3,4} \tag{4.32}$$

where the closed-loop system order, which in this case is 4, is denoted by n_{ext} .

Figure 4.10 shows the eigenvalue transition from the open loop to the closed loop while preserving semicircular shape, shown in Figure 4.9.

Using the Ackerman formula, tuning gains are:

$$\begin{aligned} \mathbf{k} &= \begin{bmatrix} -166.17 & 283.86 & 7.30 \end{bmatrix} \\ \mathrm{k_i} &= -230.63 \times 10^3 \end{aligned} \tag{4.33}$$

The holistic control law then takes the following form for the three operating modes:

$$\begin{aligned} v_{abj} &= \mathrm{k}_1 x_1 + \mathrm{k}_2 x_2 + \mathrm{k}_3 x_3 + \mathrm{k_i}\sigma_{\mathrm{j}} \\ \dot{\sigma}_{\mathrm{j}} &= x_{\mathrm{j}}^* - x_{\mathrm{j}} \end{aligned} \tag{4.34}$$

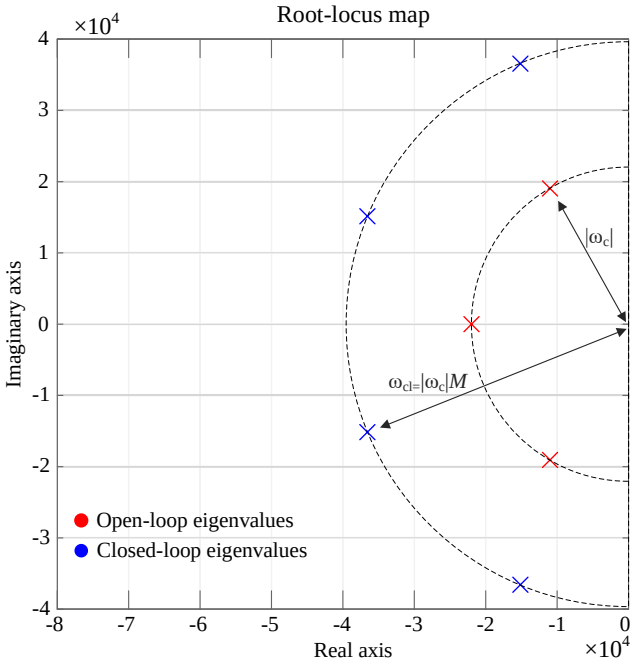

Figure 4.10: Movement of the root locus in closed loop.

with j = ism, gcr, and gci.

The matrices $\hat{\mathbf{A}}$ and the closed-loop eigenvalues for each mode are summarized in Table 4.4. As can be seen, all of the eigenvalues are constrained by the physical frequency boundaries of the system and have a negative real part.

The three legs of the three-phase full bridge converter shift by 120° and 240° following control law (4.34) for the remaining two phases.

Table 4.4: Closed-loop matrices and eigenvalues.

Operation mode	Closed-loop matrix	Eigenvalues (rad/s)
Islanded mode (ism)	$\hat{\mathbf{A}}_{\text{ism}}$	$\alpha_{1,2\_\text{ism\_cl}} = -36.55 \pm j15.13 \times 10^3$
		$\alpha_{3,4\_\text{ism\_cl}} = -15.13 \pm j36.54 \times 10^3$
Grid-connected (inverter)		$\alpha_{1\_\text{gci\_cl}} = -36.02 \times 10^3$
inverter (gci)	$\hat{\mathbf{A}}_{\text{gci}}$	$\alpha_{2,3\_\text{gci\_cl}} = (-33.49 \pm j42.08) \times 10^3$
		$\alpha_{4\_\text{gci\_cl}} = -335$
Grid-connected (rectifier)	$\hat{\mathbf{A}}_{\text{gcr}}$	$\alpha_{1,2\_\text{gcr\_cl}} = (-26.04 \pm j40.69) \times 10^3$
mode (gcr)		$\alpha_{3,4\_\text{gcr\_cl}} = (-3.65 \pm j1.27) \times 10^3$

where:

$$\hat{\mathbf{A}}_{\text{ism}} = \begin{bmatrix} -59.40 & 34.77 & -1.73 & 48263.88 \\ 0 & -43.94 & 0.62 & 0 \\ 1153.60 & -1153.60 & 0 & 0 \\ 0 & 0 & -0.001 & 0 \end{bmatrix} \times 10^3 \tag{4.35}$$

$$\hat{\mathbf{A}}_{\text{gci}} = \begin{bmatrix} -59.40 & 34.77 & -1.73 & 48263.88 \\ 0 & -43.94 & 0.62 & 0 \\ 1153.60 & -1153.60 & 0 & 0 \\ 0 & -0.001 & 0 & 0 \end{bmatrix} \times 10^3 \tag{4.36}$$

$$\hat{\mathbf{A}}_{\text{gcr}} = \begin{bmatrix} -59.40 & 34.77 & -1.73 & 48263.88 \\ 0 & 0 & 0.62 & 0 \\ 1153.60 & -1153.60 & 0 & 0 \\ 0 & -0.001 & 0 & 0 \end{bmatrix} \times 10^3 \tag{4.37}$$

4.5 Inertia in the power systems

Due to the high penetration of systems based on power electronics, the stability of the electrical power system is being compromised [43]. The most significant impact is reflected in reducing the constant inertia H_{sys}.

The ability of bodies to maintain their relative motion or state of rest, or the resistance to changing their state of motion, is defined as inertia in physics. Most of the inertia in conventional electrical power systems is generated by the rotating parts of the synchronous generators and their turbines. Conventional generators can resist frequency changes during imbalances between the power demanded and the power generated because of the kinetic energy they store due to this inertia.

It reveals how well the system can withstand various disturbances and maintain steady behavior.

As shown in Figure 4.11, the traditional power systems that rely on nuclear, coal, or hydroelectric generation with high inertia are currently evolving into inverter-dominated power systems that have little to no inertia.

Power electronics do not provide an inertial response in the system. Therefore the transient of the power system frequency is altered [44, 45]. Especially in systems with a high percentage of renewable energy penetration combined with low demand [46, 47]. This is due to the lack of an adequate energy balance within an adequate time interval, which is reflected in the frequency, as shown in Figure 4.12, [48, 49].

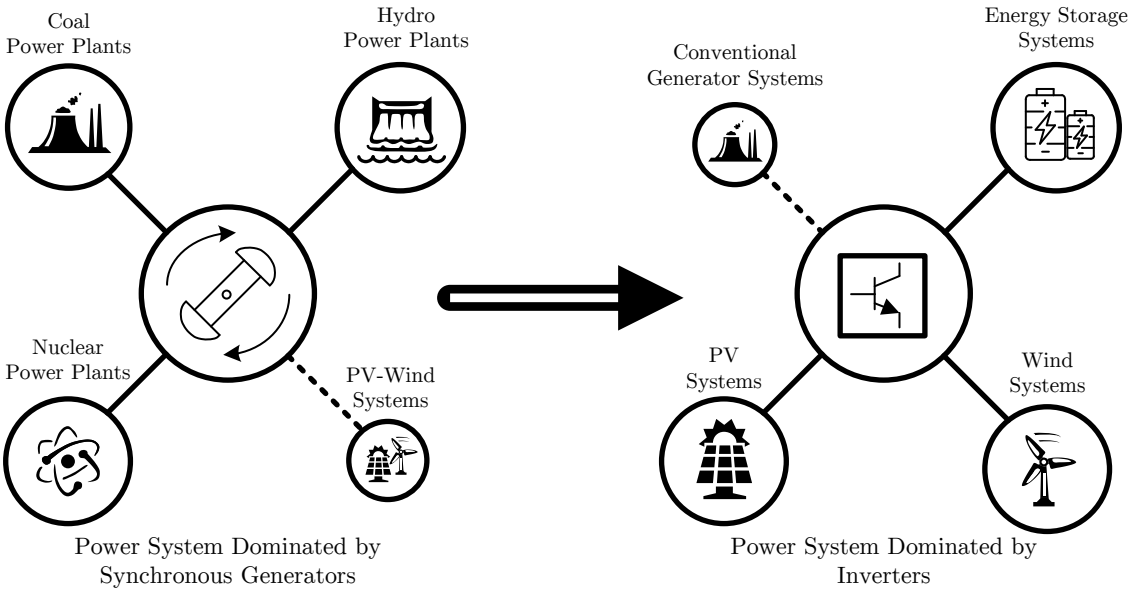

Figure 4.11: Evolution of traditional power systems towards systems dominated by inverters [4].

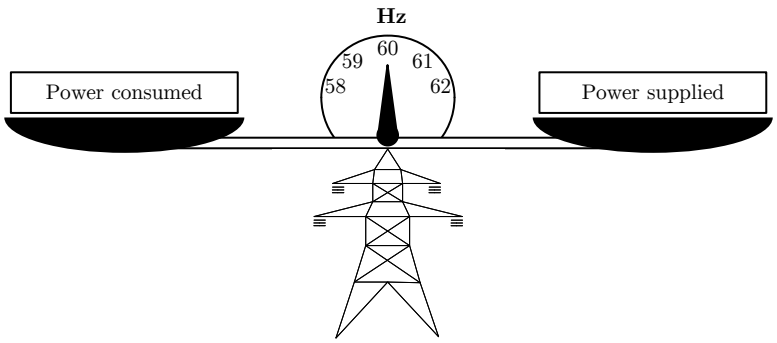

Figure 4.12: Power balance physics for a constant frequency system.

To understand the relationship between the frequency and power unbalance, we can begin by expressing the Equation (4.38) that describes how much rotational or kinetic energy is stored in synchronous generators E_{Keq}.

$$E_{Keq} = \frac{1}{2} J_g \omega_m^2 \tag{4.38}$$

where ω_m is the angular speed of the rotor and J_g is the moment of inertia of the synchronous machine. Based on the rated power of the generator S_{base} in VA, the kinetic energy can be expressed as a constant called H_{eq} that represents the period of time in seconds for which the generator can supply its rated power using only its stored

kinetic energy as:

$$H_{eq} = \frac{E_{Keq}}{S_{\text{base}}} = \frac{J_g \omega_m^2}{2 S_{\text{base}}} \tag{4.39}$$

in terms of H_{eq}, the moment of inertia J_g can be defined as:

$$J_g = \frac{2H_{eq}}{\omega_m^2} S_{\text{base}} \tag{4.40}$$

A fundamental dynamical principle states that an accelerating torque results from multiplying the rotor's moment of inertia by its angular acceleration. This fundamental dynamical principle forms the basis of the equation that governs the rotor motion of a synchronous machine as:

$$J_g \frac{d\omega_m}{dt} = T_a = T_m - T_e \tag{4.41}$$

where:

- T_a is the accelerating torque.
- T_e is the electromagnetic torque.
- T_m is the mechanical torque.

The equation of motion for a synchronous machine is shown in Equation (4.42). The "swing equation" can be obtained by using Equations (4.40), (4.41), and $P = T\omega$.

$$\frac{2H_{eq}}{\omega_0} \frac{d\omega_m}{dt} = \frac{P_{mec} - P_e}{S_{\text{base}}} \tag{4.42}$$

where:

- P_{mec} is the mechanical active power.
- P_e is the electromagnetic active power.
- ω_0 is the rated angular velocity.

More specifically, without sufficient inertia in the system, it leads to a higher Rate of Change of Frequency (RoCoF); that is, it further weakness the capacity of isolated power systems to handle generation outages [50]. This means that the grid frequency and/or the derivative of the frequency with respect to the RoCoF can go beyond acceptable ranges upon system failure, leading to rotor angle stability problems, disconnection of undesirable load or even the complete collapse of the system [51].

When there is a change in a load that demands a power greater than what is generated, a transient in the frequency occurs. To mitigate this effect, the frequency of the electrical network is monitored, if it is less than certain previously predefined values, the load disconnection is activated (the lower the frequency, the more load is disconnected) [50].

Several solutions have been proposed to address the lack of inertia, such as adding extra masses to the power system by rotating through condensers synchronous [52].

Another solution is to make the power electronics capable of mimicking the rotational inertia of a conventional synchronous generator. This is also called "virtual" or "synthetic" inertia and needs to be added in generation systems [46, 50, 52, 53].

Traditionally, in renewable energies there were not storage service at the distribution level. Technologies and operating concepts to effectively integrate renewable energy into existing power systems continue being developed to earn additional benefits and avoid negative impacts on system reliability and safety [2].

Several proposals have raised in different references. A general classification of the state of the art for virtual inertia topologies is shown in Figure 4.13. From the topologies mentioned, the synchronverter [54], the Ise lab's topology [49, 55, 56, 57], and the virtual synchronous generator [58] are the most popular.

Some topologies are shown in [49, 57, 58] that attempt to mimic the exact dynamics of synchronous machines through an elaborate mathematical model. Other techniques aim to make this more straightforward by approximating the behavior of the synchronous machines using only the oscillation equation, as is shown in [4, 52, 53, 55]. Other topologies, in contrast, use a strategy that forces renewable generation units to respond to shifts in frequency in the power system [59, 60].

A comparison of a power system with no virtual inertia on the dotted red line and a system with added virtual inertia on the green line is shown in Figure 4.14.

In Figure 4.14, several control actions can also be observed that are implemented during various time intervals to guarantee a stable operation in the power systems and maintain the balance between the energy demanded and the energy generated, as shown in Figure 4.12. First, the inertia is responsible for counteracting the initial imbalance between generation and consumption due to transient events, typically within first 10 s. Second, the governor feedback is the main control action that takes place typically within 10-30 s and is intended to reduce frequency deviation. Third, the automatic generation control is the action that takes place in minutes, typically within 10-30 min, and restores the system frequency to the nominal value. Then control action is the reserve deployment when measures are taken to obtain the necessary resources to face present or future disturbances in the system.

The penetration of the power system by power electronics is such that the formal definition: "*Power system stability is the ability of an electric power system, for a given initial operating condition, to regain a state of operating equilibrium after being subjected to a physical disturbance, with most system variables bounded so that practically the entire system remains intact*" given in [5]. This term has been extended but not modified to address the fast transients that begin to affect the dynamic system behavior [61].

Figure 4.15 reports the previous classification in gray. Furthermore, it can be seen that two additional stability classes: "Resonance stability" and "Converter-driven stability," have been added in blue.

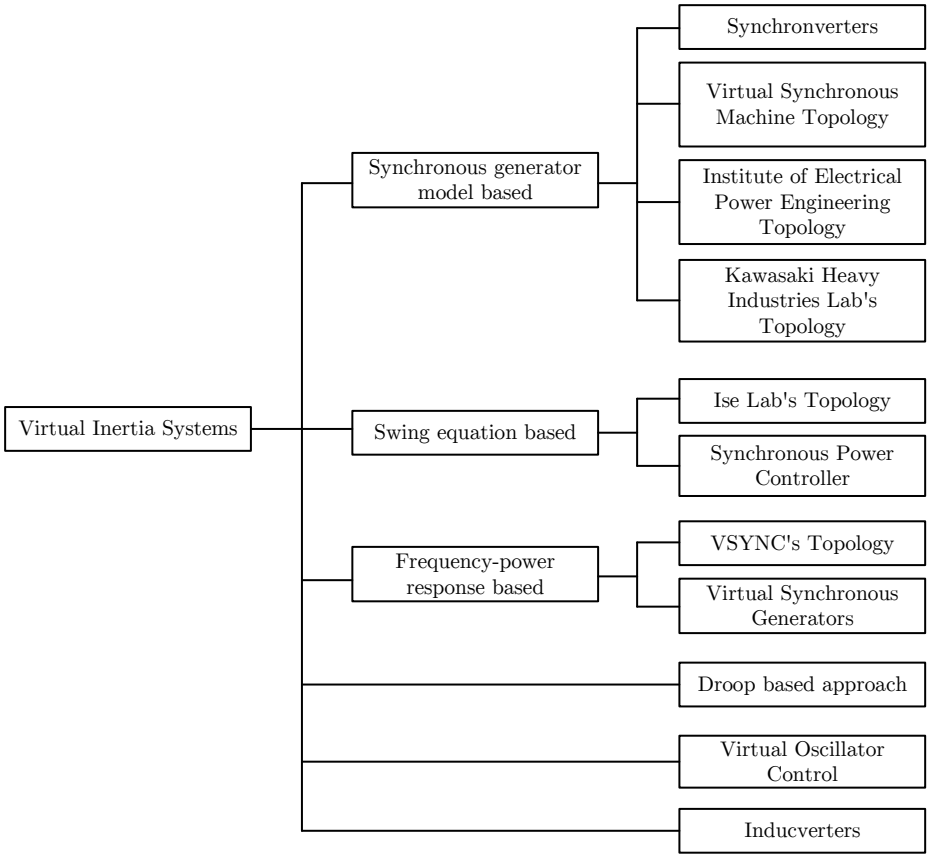

Figure 4.13: Classification of topologies used for virtual inertial control [4].

4.6 Holistic control with virtual inertia as ancillary service

This section presents the incorporation of virtual inertia in the BESS as an extra ancillary service to the electrical network by using the same holistic control. As can be seen in Figure 4.5, the virtual inertia is incorporated into the reference signal.

For this work, two different methods were used to add virtual inertia to the BESS. Both methods use the oscillation equation presented in (4.43) to generate the active power reference that must be delivered or absorbed from the electrical power system to replicate the inertia of the synchronous machine.

$$\frac{2H_{eq}}{\omega_0}\frac{d\omega_m}{dt} = \frac{P_{mec} - P_e}{S_{\text{base}}} \tag{4.43}$$

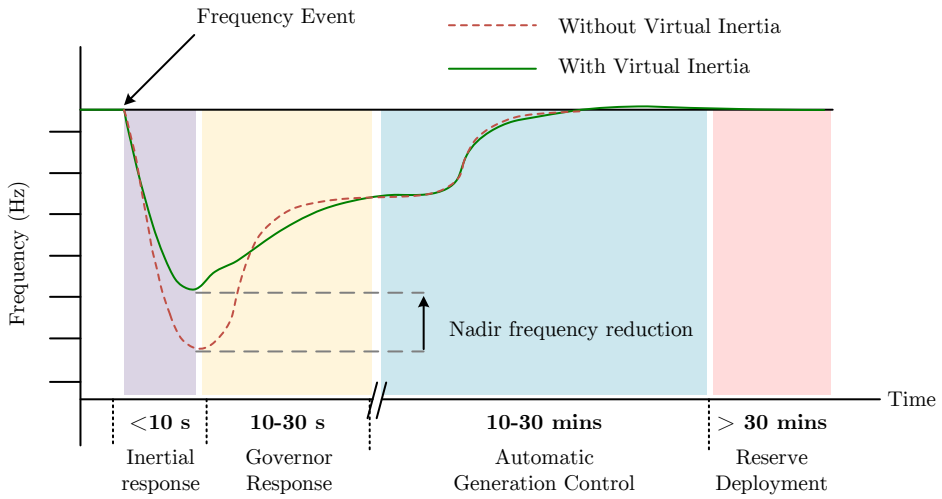

Figure 4.14: Comparison of a power system with virtual inertia and one without virtual inertia [4].

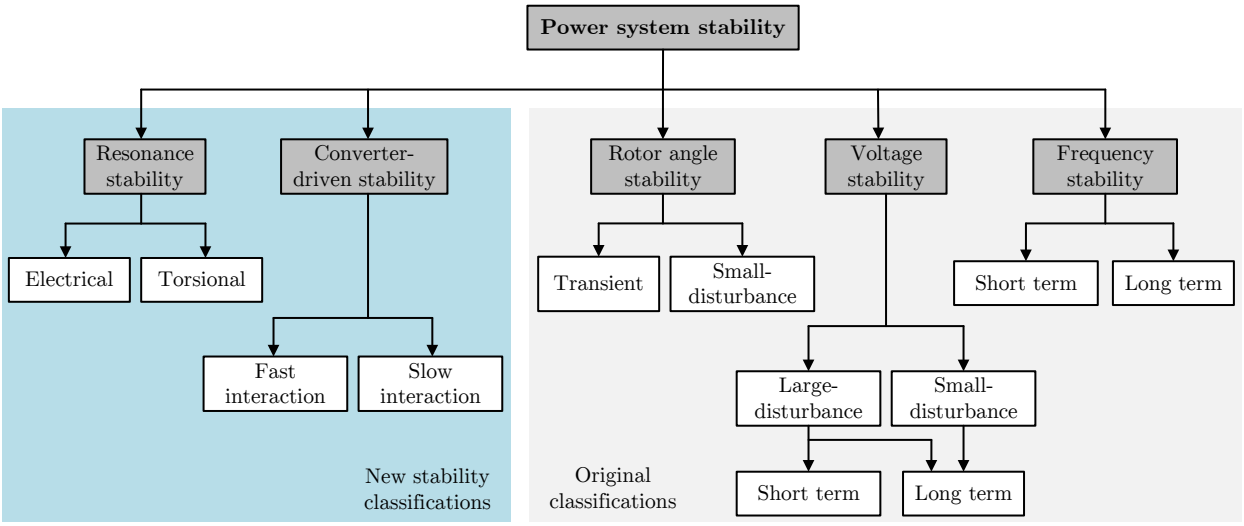

Figure 4.15: Power system stability classification. New stability [5], and original stability [6].

where P_{mec} is the mechanical power, P_e is the electrical power, H_{eq} is the virtual inertial constant, ω_m is the angular velocity of the rotor in rad/s, ω_0 is the rated angular velocity of the rotor in rad/s, and the apparent rated power is S_{base} in VA.

By using the swing equation (4.43), which defines the relation between the stored

kinetic energy of the rotating mass and active power mismatch [62], the virtual inertia reference is included as P^*_{anci} in the layer of control called "extra ancillary services", it is added to P^*_t as:

$$P^*_t = P^*_{mec} + P^*_r + P^*_{droop} + P^*_{anci} \tag{4.44}$$

As can be seen in Figure 4.5.

4.6.1 First method for calculating virtual inertia as ancillary service

The first method to create the active power reference and generate virtual inertia in the BESS is taken from [48] and [63], where, by means of the swing equation (4.45) that describes the relationship between the stored kinetic energy of the rotating mass, and active power mismatch [6].

$$\frac{2E_{keq}}{\omega_0}\frac{d\omega_m}{dt} = P_{mec} - P_e = P^*_{anci} \tag{4.45}$$

where $E_{keq} = H_{eq}S_{\text{base}}$ is the stored kinetic energy, and P^*_{anci} is the amount of electrical energy produced by the generator through the inertia response, which for this work will be taken as a reference for extra ancillary services.

The kinetic energy stored in the generator E_{keq} is:

$$E_{keq} = \frac{1}{2}J_g\omega^2_{mec} = 2\pi^2 J_g f^2_{mec} \tag{4.46}$$

were J_g is the inertia moment of the rotating components, f_{mec} is the frequency of the rotor in Hz.

By means of Equations (4.45) and (4.46) can be obtained the equation for the inertial response from a synchronous generator in terms of J_g and ω_{mec}, as:

$$P^*_{anci} = \frac{4\pi^2 J_g f^2_{mec}}{f_0}\frac{df_{mec}}{dt} \tag{4.47}$$

were f_0 is the rated frequency in Hz.

The power system maintains a few percent deviations of the rated frequency even during significant disturbances, which forms the basis for the approximation of equality between rated and actual frequency as $f_{mec} \approx f_0$, then the equation (4.47) is:

$$P^*_{anci} = \frac{4\pi^2 J_g f^2_{mec}}{f_0}\frac{df_{mec}}{dt} \approx 4\pi^2 J_g f_0 \frac{df_{mec}}{dt} = K_{inertia_J}\frac{df_{mec}}{dt} \tag{4.48}$$

where:

$$K_{inertia_J} = 4\pi^2 J_g f_0 \tag{4.49}$$

Besides, the $K_{inertia}$ can be expressed in terms of the constant inertia H_{eq}, combining (4.43) and (4.45):

$$H_{eq} = \frac{E_{keq}}{S_{\text{base}}} = \frac{J_g \omega_{mec}^2}{2S_{\text{base}}} = \frac{2\pi^2 J_g f_{mec}^2}{S_{\text{base}}} \tag{4.50}$$

rewriting (4.43):

$$S_{\text{base}} \frac{2H_{eq}}{\omega_0} \frac{d\omega_{mec}}{dt} = P_{mec} - P_e = P^*_{anci} \tag{4.51}$$

then by means of the equations (4.50) and (4.51) can be obtained the inertial response from a synchronous generator in terms of H_{eq} and ω_m, taking into account the approximation $f_{mec} \approx f_0$, as:

$$P^*_{anci} = \frac{2S_{\text{base}} H_{eq}}{f_0} \frac{df_{mec}}{dt} \approx K_{inertia} \frac{df_{mec}}{dt} \tag{4.52}$$

where:

$$K_{inertia} = \frac{2S_{\text{base}} H_{eq}}{f_0} \tag{4.53}$$

Droop response it is also added, the following expression describes the relation about how many extra active power a generator will supply in response to a system frequency deviation.

$$P^*_{droop} = \frac{S_{\text{base}}}{R} \frac{(f_e - f_0)}{f_0} = K_{droop} (f_e - f_0) \tag{4.54}$$

Where P^*_{droop} is the extra amount of power to recover the f_0, R is a system-specific droop constant, f_e is the electrical frequency in Hz, and K_{droop} is the droop constant.

Since the frequency is considered a global parameter of the power system, f_{mec} can be taken from electrical measurement as f_e, to reproduce the virtual synchronous machine, and the following relations can be established:

$$P^*_{anci} = K_{inertia} \frac{df_e}{dt} \tag{4.55}$$

$$P^*_{droop} = K_{droop} (f_e - f_0) \tag{4.56}$$

P^*_{droop} and P^*_{anci} are the references for the BESS to incorporate the virtual inertia as an extra ancillary service. A typical configuration of inertia and droop control is presented in Figure 4.16, it can be seen the addition of a low pass filter to eliminate the high-frequency noise and avoid amplified noise in the derivative calculation of RoCoF.

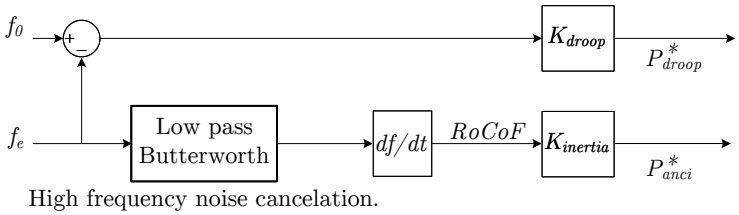

Figure 4.16: Inertia and droop control working principle.

4.6.2 Second method for calculating virtual inertia as ancillary service

For the second virtual inertia method, it will not only emulate inertia but also damping. For this, an extension of the concept must be carried out where a virtual governor and a virtual turbine are also included in the reference creation of power to inject or absorb into the electrical grid.

Hydraulic turbines at waterfalls, steam turbines powered by the combustion of coal, gas, or nuclear fuel, and gas turbines can all be used as the source of mechanical power, also referred to as the prime mover. The turbine model relates the steam valve position P_v and mechanical power output $P_{mec_{p.u.}}$. The characteristics of various turbine types differ greatly. With just one time constant, T_{CH}, the most basic prime mover model for the steam turbine, can be approximated obtaining the transfer function shown below [64]:

$$G_T(s) = \frac{P_{mec_{p.u.}}}{P_v} = \frac{1}{1 + sT_{CH}} \tag{4.57}$$

where the time constant T_{CH} ranges between 0.2 s and 2.0 s.

The governors are designed to allow the speed to decrease as the load increases for stable operation. According to [64], the governor is given by:

$$P_v = \frac{1}{1 + sT_G} P_g \tag{4.58}$$

where T_G represents the steam valve position time constant for the hydraulic amplifier.

$$P_g(s) = P^*_{r_{p.u.}} - \frac{1}{R}\left(\omega_{mec_{p.u.}} - \omega_{0_{p.u.}}\right) \tag{4.59}$$

where $P^*_{r_{p.u.}}$ is the power reference given to the virtual governor.

This second method calculates the active power reference and generates the virtual inertia in the BESS, taken from [65].A typical inertia configuration in conjunction with the virtual governor and the virtual turbine is presented in Figure (4.17), where k_D is the damping constant, $T_{mec_{p.u.}}$ in the mechanical torque, $T_{e_{p.u.}}$ is the electrical torque, and $P_{mec_{p.u.}}$ is the mechanical power of the virtual turbine that will be the reference of the droop and damping as $P^*_{droop_{p.u.}}$.

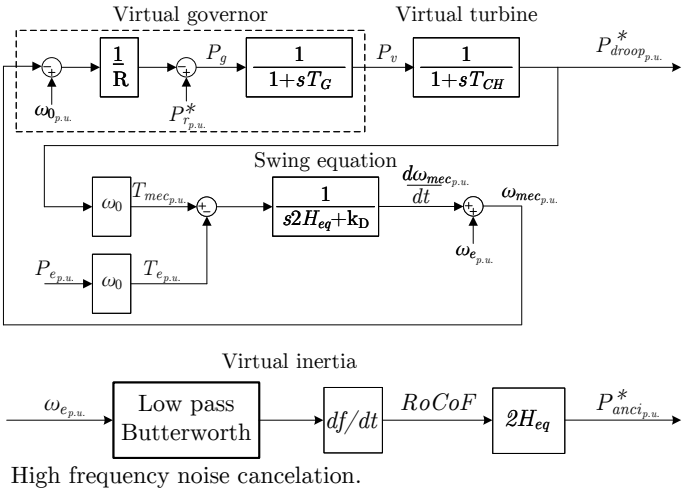

Figure 4.17: Block diagram of the inertia and governor control.

Chapter 5

Performance evaluation

In this chapter, the performance of the BESS with the holistic controller is evaluated by simulation and experiments, the last ones for specific cases. A protocol of tests has been formulated to reveal the properties of the holistic control.

The configuration of the experiment is based on Figure 5.25. This experiment considers several scenarios highlighting the control properties for achieving the standard IEEE 1547-2018.

Those scenarios include changes of mode from interconnected mode to islanded mode, islanded mode to interconnected mode, interconnected mode as an inverter to interconnected mode as a rectifier, and the protocol includes load steps as well. All the mode changes are executed on the fly to demonstrate the capability of the holistic control under the most demanding transients.

Additionally, simulations in a steady state for showing the BESS performance incorporating virtual inertia into the grid power system are included.

At the end of this chapter, the results are discussed.

5.1 Simulation results with the first tuning

To demonstrate the performance of the first tuning, consider the circuit shown in Figure 5.1, which is implemented in the PSCAD/EMTDC software. This circuit is designed to operate under duty class II [66], with a rated power of 100 kW. Table 5.1 presents the parameters and specifications of the BESS, including the controller gains using the first holistic control, whilst Table 5.2 shows the timeline used for commuting through all the proposed operation modes and load steps. The mode changes are enabled by the breakers BRK_1, BRK_2, and BRK_3.

Following the summarized protocol shown in Table 5.2, the simulations are performed as follows:

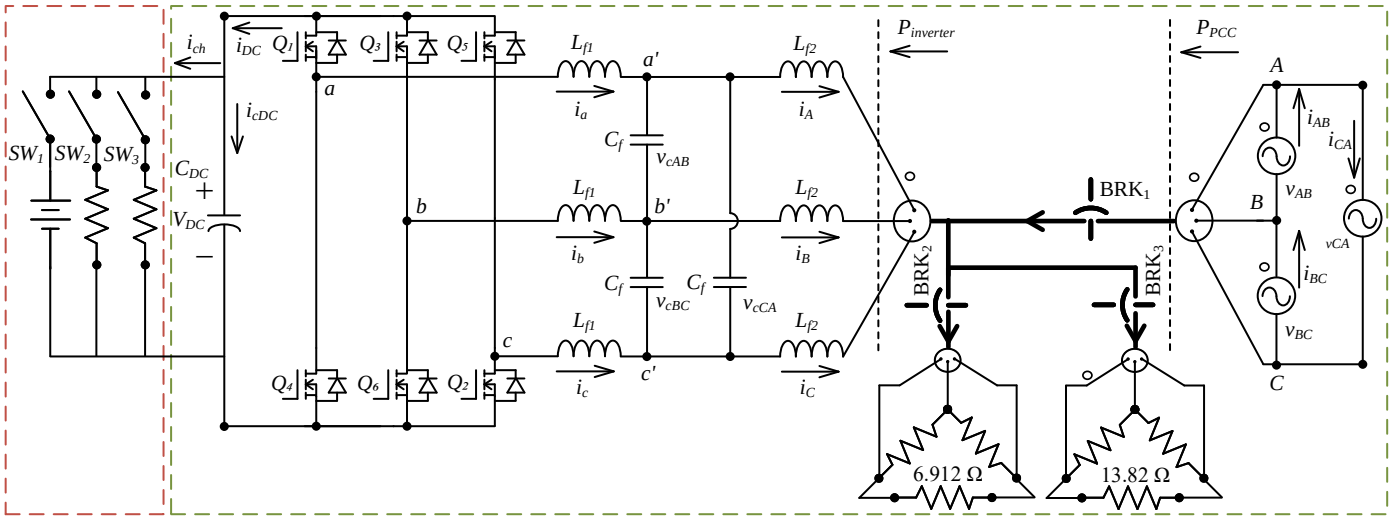

Figure 5.1: Whole BESS scheme used for simulations.

Table 5.1: Electrical specification and parameters.

Specifications/parameters	Value
Grid voltage (AC: L-L, RMS)	480 V
Rated power	100 kW
Power factor	Near to unity
V_{DC}	920 V ($\pm 3\%$)
THD of current (i_{AB}, i_{BC}, i_{CA})	$< 5\%$
THD of voltage (v_{AB}, v_{BC}, v_{CA})	$< 5\%$
Switching frequency	12 060 Hz
Delta-LCL filter: (L_{f1}, L_{f2}, C_f)	(220 μH, 73 μH 37 μF)
Tuning gains	$\mathbf{k} = \begin{bmatrix} -5.18 & 25.92 & 6.00 \end{bmatrix}$ $\mathrm{k_i} = -62.8319 \times 10^3$

5.1.1 Timeline from 0 to 1.2 s

This timeline is used to demonstrate operation mode changes, load steps, and reference changes, always working as an inverter.

As can be seen in Figure 5.2, first from 0 s to 0.1 s, the closed-loop inverter works delivering -1.56 p.u. of active power at the $P_{inverter}$ node, where the negative sign

Table 5.2: Test protocol according to timeline for holistic first tuning design control.

Time (s)	Mode	$P_{\text{base}} = 100\,\text{kW}$	BRK_1	BRK_2	BRK_3
0−0.1	Grid-connected (inverter) mode	−1.56 p.u.	Closed	Closed	Open
0.1−0.3	Grid-connected (inverter) mode	−1.06 p.u.	Closed	Closed	Open
0.3−0.5	Islanded mode	−0.99 p.u.	Open	Closed	Open
0.5−0.7	Islanded mode	−1.48 p.u.	Open	Closed	Closed
0.7−1.0	Islanded mode	−0.99 p.u.	Open	Closed	Open
1.0−1.2	Grid-connected (inverter) mode	−1.06 p.u.	Closed	Closed	Open
1.2−1.6	Grid-connected (rectifier) mode	1.06 p.u.	Closed	Closed	Open
1.6−2.0	Grid-connected (rectifier) mode	1.53 p.u.	Closed	Open	Open

indicates that the power flow is coming out of the inverter. Since BRK_1 is closed, there is a local load consumption of 1 p.u., therefore, in the P_{PCC} only -0.56 p.u. are being injected into the electrical power system. In 0.1 s, a reference change occurs. Second, from 0.1 s to 0.3 s the power delivered by the inverter to the $P_{inverter}$ node is -1.06 p.u because the three breakers remain in the same position, the local load of 1 p.u. is kept, therefore, in the P_{PCC}, only -0.06 p.u. are being injected to the electrical power system. Next an operation change from grid-connected mode to islanded mode take place at t = 0.3 s, where now the P_{PCC} is 0 and the $P_{inverter}$ is -0.99 p.u. Then, two local load changes occur at t = 0.5 s and t = 0.7 s being -1.48 p.u. and -0.99 p.u. the power delivered to the local loads, respectively. Finally, an operation change from islanded mode to grid connected mode occurs at t = 1.0 s with -1.06 p.u.

The power factor is an important electrical requirement that must be satisfied. The performance of this parameter is displayed in Figure 5.3. It is significant to note that the power factor reaches unity when the islanded mode is operating because the load is purely resistive.

The THD of voltage and current are other parameters associated with power quality and required by IEEE 1547-2018. Figure 5.4 depicts the voltage THD at the top and the current THD at the bottom. As can be seen, both values remains within the limits specified in Table 5.1. In comparison to islanded mode, the voltage THD is lower in grid-connected mode, because the grid has a stronger influence than the inverter.

Figures 5.5 and 5.6 show the transient that occurs in voltage and current for operation changes between grid-connected and islanded mode, respectively. Observe that Figure 5.6 on the left shows a strong current variation during the transient. That phenomenon is explained because at the beginning of the test the reference of the inverter is current and the grid voltage dominates the performance of the capacitor voltage at v_{cAB}, besides this mode change implies a change of reference from current

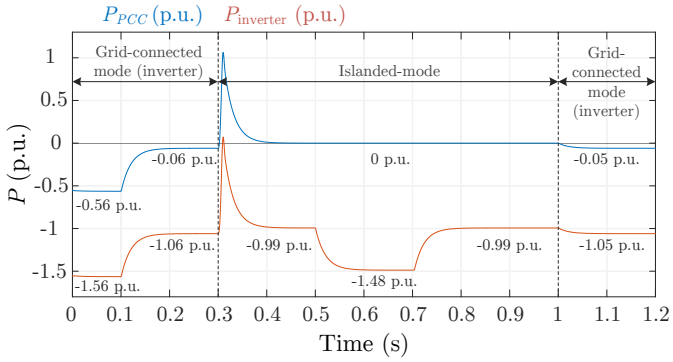

Figure 5.2: Active power duty class during timeline from 0 s to 1.2 s.

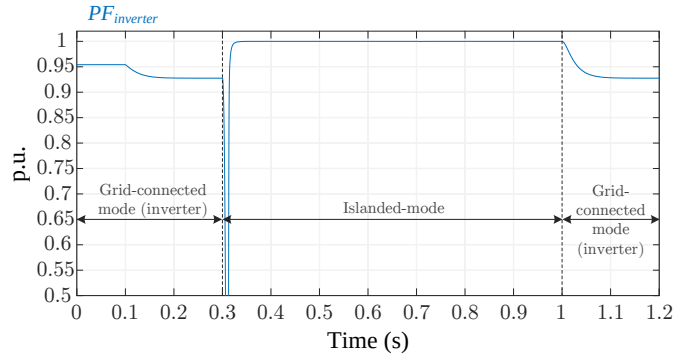

Figure 5.3: Power factor from timeline 0 s to 1.2 s.

to voltage; so the current stops being controlled producing that variation shown on the left side of Figure 5.6. Following the same idea, the voltage begins to be controlled due to the reference change, which can be observed as a minimum effect on the left side of Figure 5.5. This phenomenon does not occur on the right side of Figures 5.5 and 5.6 because the grid imposes its strong over the capacitor voltage.

To illustrate the grid-connected performance when load steps occur, Figures 5.7 and 5.8 display the evolution of the voltage and current, respectively. On the left side of these figures it is show the performance facing load steps during the grid-connected (inverter) mode. On the right the islanded-mode behavior is shown. It can be seen that the reference tracking control is suitable.

5.1.2 Timeline from 1 to 2 s

This timeline considers a operation change from grid-connected (inverter) to grid-connected (rectifier) modes, including a load step.

The following simulations confirm the holistic feature of the closed-loop grid-

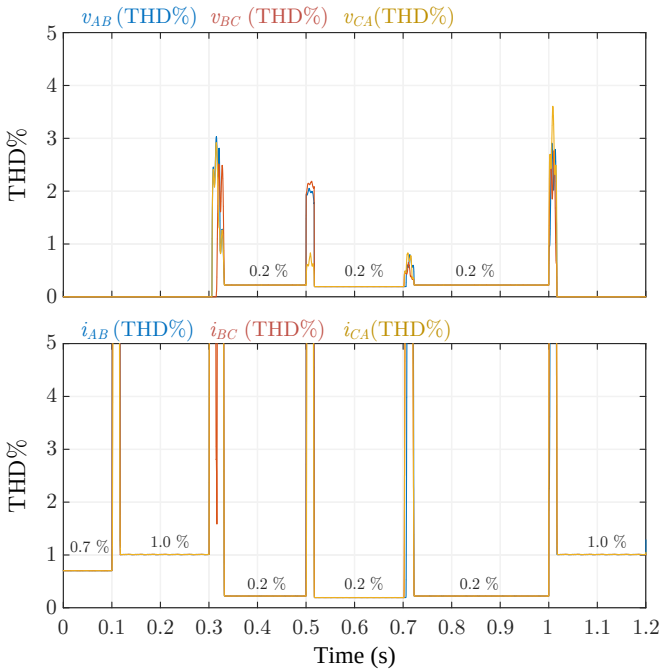

Figure 5.4: Voltage and current THD from timeline 0 s to 1.2 s.

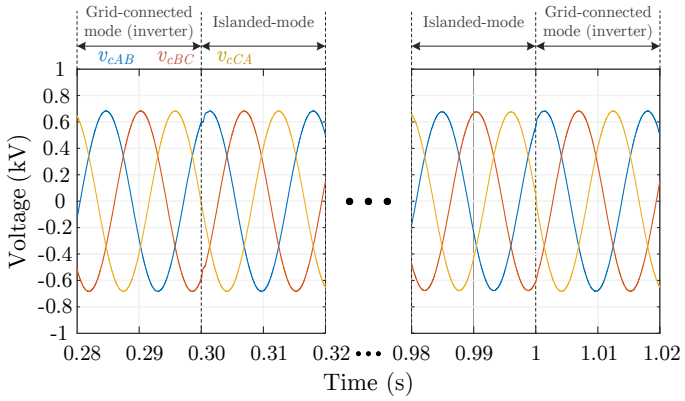

Figure 5.5: Voltage transients when mode changes occur.

connected converter working as a rectifier.

In Figure 5.9 the DC capacitor voltage V_{DC} is shown to validate the capability of the proposed controller to maintain the DC voltage regulated around $V^*_{DC} = 920\,V$. It can be observed that as for mode changes as for load steps the DC voltage is regulated within the threshold of ±3% required in Table 5.5.

In Figure 5.10 the power performance is plotted to show the capability to change from grid-connected (inverter) mode to grid-connected (rectifier) mode fulfilling the duty class II. It is important to correlate Figures 5.9 and 5.10 and to observe that in

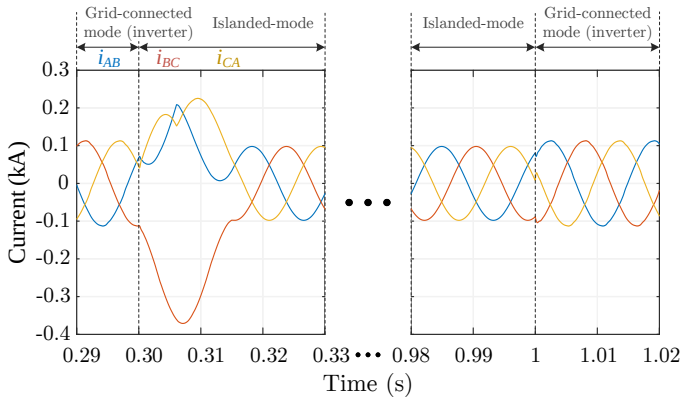

Figure 5.6: Current transients when mode changes occur.

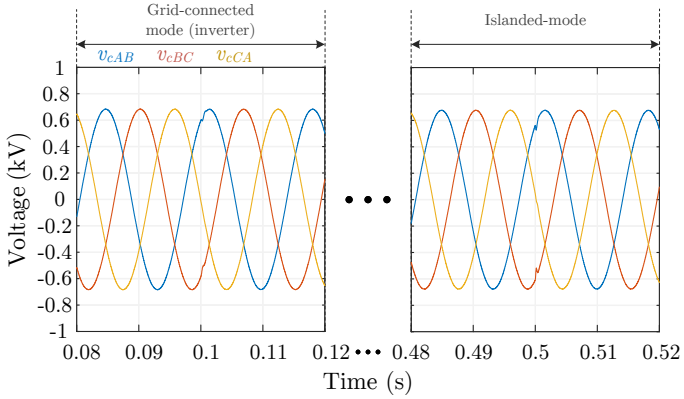

Figure 5.7: Voltage transients when load changes occur.

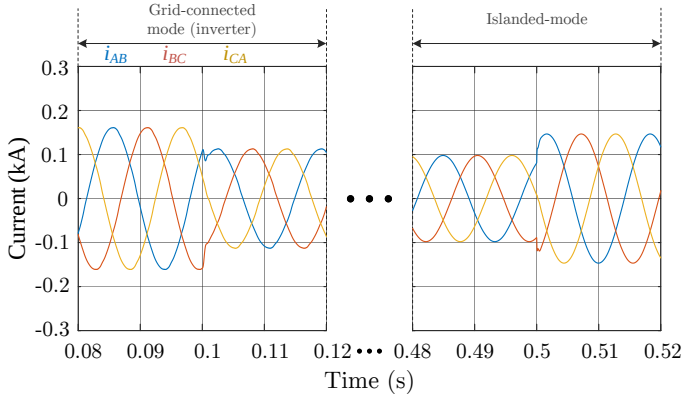

Figure 5.8: Current transients when load changes occur.

the power transients the DC voltage regulation is maintained.

The power factor is a relevant parameter to be accomplished in all the operation

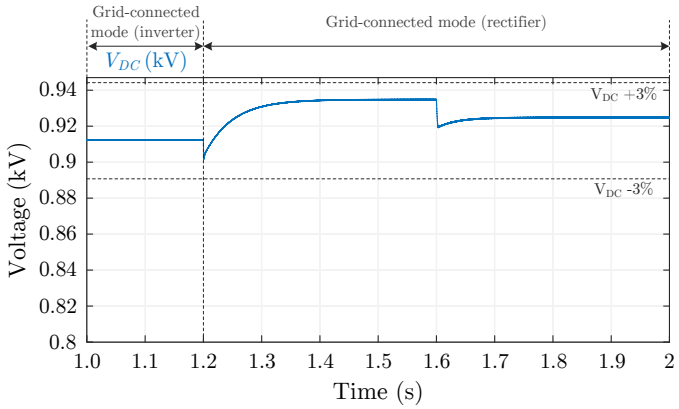

Figure 5.9: Voltage V_{DC}, for timeline from 1.0 s to 2.0 s.

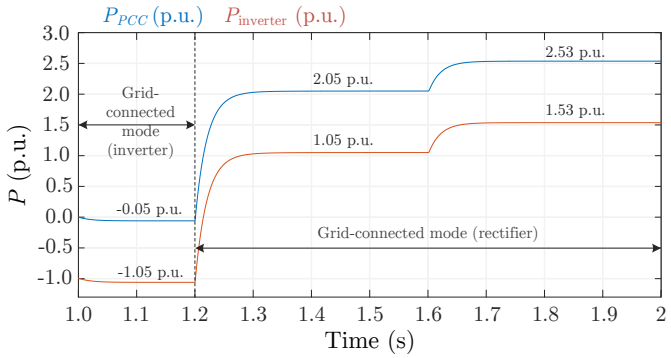

Figure 5.10: Active power duty class II during timeline from 1.0 s to 2.0 s.

modes. Thus, Figure 5.11 presents the grid-connected mode (rectifier) power factor performance. It can be appreciated the capability to maintain a high power factor over 0.95 and near to 1.

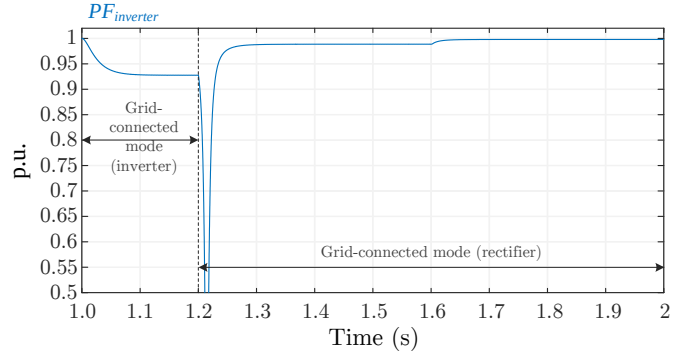

Figure 5.11: Power factor from 1.0 s to 2.0 s.

The voltage and current harmonic distortions are important in the grid-connected (rectifier) mode. Hence, Figure 5.12 shows at the top the THD voltage while at the bottom the THD current. It is possible to notice that during the steady state of the test, the limits established in Table 5.1 are satisfied.

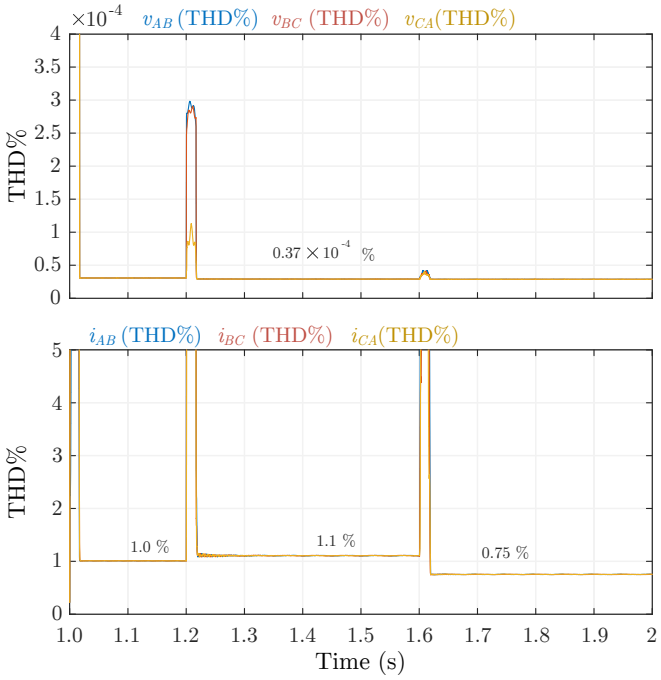

Figure 5.12: Voltage and current THD from 1.0 s to 2.0 s.

In Figures 5.13 and 5.14, the instantaneous voltage and current when an operation mode from inverter to rectifier occurs at $t = 1.2$ s and a load transient occurs at $t = 1.6$ s, are shown respectively.

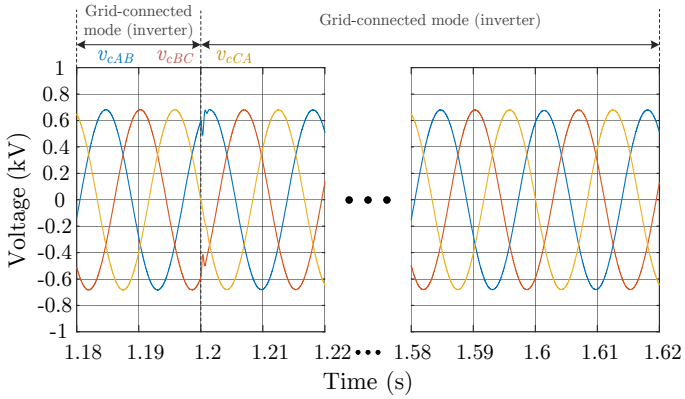

Figure 5.13: Voltage transients when a mode change occurs and when load changes occur.

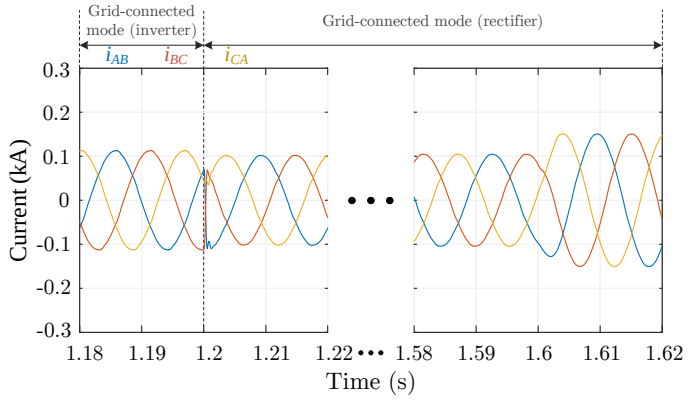

Figure 5.14: Current transients when a mode change occurs and when load changes occur.

It can be appreciated the adequate response of the grid-connected converter for both, mode changes and load transients in rectifier mode.

Table 5.3 summarizes the electrical specifications achieved by using the holistic control. It can be observed the capability to fulfill for each mode.

Table 5.3: Electrical specifications achieved for each operation mode.

$P_{inverter}$ $P_{\text{base}} = 100\,\text{kW}$	Specification	Islanded mode	Grid-connected (inverter) mode	Grid-connected (rectifier) mode
1.0 p.u.	P.F.	1	0.93	0.93
1.0 p.u.	$\text{THD}_{\text{current}}$	0.20%	1.00%	1.11%
1.0 p.u.	$\text{THD}_{\text{voltage}}$	0.20%	Near to 0	Near to 0
1.0 p.u.	$\text{Error}_{V_{DC}}$	NA	NA	1.4%
1.5 p.u.	P.F.	1	0.95	0.92
1.5 p.u.	$\text{THD}_{\text{current}}$	0.20%	0.70%	0.75%
1.5 p.u.	$\text{THD}_{\text{voltage}}$	0.20%	Near to 0	Near to 0
1.5 p.u.	$\text{Error}_{V_{DC}}$	NA	NA	0.32%

Table 5.4 reveals the relevant features of the holistic control, the features are basically the same with exception of the reference although certainly, references are not part of the controller tuning.

Table 5.4: Holistic control features.

Features	Islanded mode	Grid-connected (inverter) mode	Grid-connected (rectifier) mode
DQ frame transformation	No	No	No
Double-loop controllers	No	No	No
Different control schemes	No	No	No
References	v^*_{cAB}	i^*_{AB}	i^*_{AB}
Tuning constant k_1	-5.18	-5.18	-5.18
Tuning constant k_2	25.92	25.92	25.92
Tuning constant k_3	6.00	6.00	6.00
Tuning constant k_i	-62.83×10^3	-62.83×10^3	-62.83×10^3

5.2 Simulation results with the first tuning fulfilling IEEE 1547-2018 ride-through

In this section simulation results are faced to the IEEE 1547-2018 by using the test protocol given in Table 5.2. According to this protocol, the PCC frequency lies within the thresholds established by the "continuous operation capability" of the IEEE 1547-2018 abnormal frequency ride-through for DER's, as can be seen in Figure 5.15. In Figure 5.16 can be seen that the PCC voltage lies within the thresholds established by the "continuous operation capability" of the IEEE 1547-2018 abnormal voltage ride-through for DER's.

5.3 Simulation results with the first method of virtual inertia

To validate the effectiveness of adding virtual inertia as an extra ancillary service to the BESS using holistic control, simulations in PSCAD/EMTDC were performed. The two-generator power system network shown in Figure 5.17 is used. This system is commonly used for illustrating the operating principle of virtual inertia [67].

The power system network can be seen in Figure 5.17 which consists of two buses, on the left side in the BUS_1 are connected the generator 1 G_1 rated at 100 kW in parallel

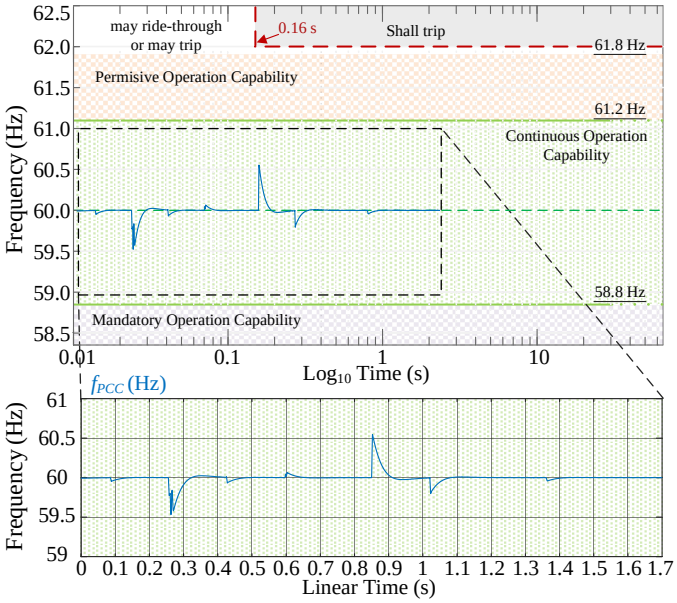

Figure 5.15: System response on frequency measured at the PCC.

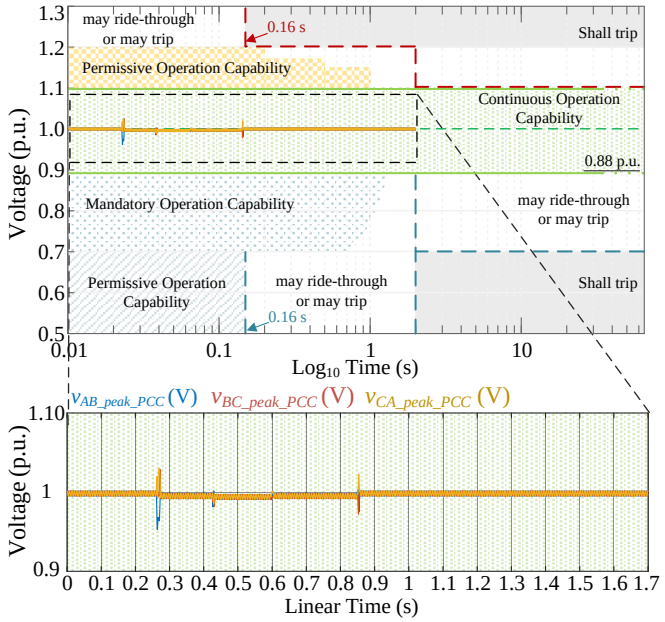

Figure 5.16: System response in the voltage amplitude measured at the PCC.

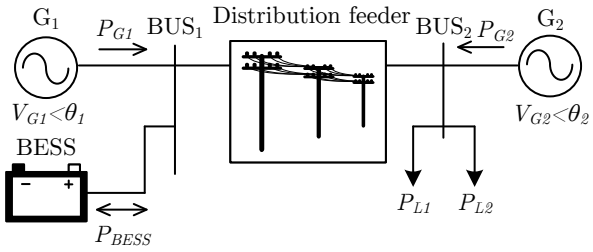

Figure 5.17: Two buses power system with a distribution feeder.

with a BESS system rated at 100 kW, on the right side in the BUS_2 are connected the generator 2 G_2 rated at 500 kW, and the loads P_{L1} and P_{L2}, both buses are tied to each other through a 100 km distribution feeder. Furthermore, the synchronous generators were equipped with turbine governor and excitation systems.

Two case studies were simulated; case 1 is a benchmark system where only the two generators are working without the BESS, there is also a resistive load connected to the system drawing $P_{L1} = 200$ kW, then at t=100 s a large load change of $P_{L2} = 100$ kW is connected.

From Figure 5.18, we can see that with higher H_{eq} value, the frequency nadir becomes closer to the f_0.

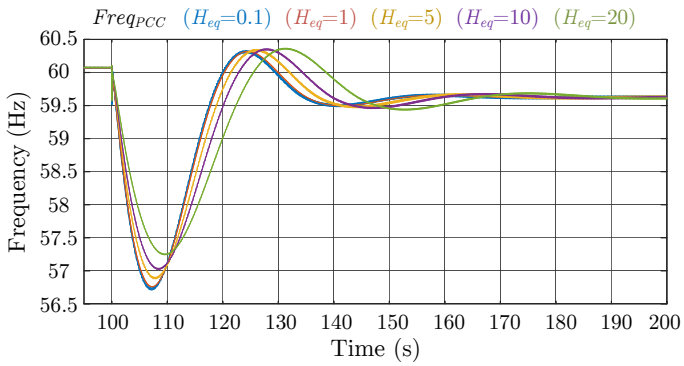

Figure 5.18: Frequency response under different H_{eq} values for case 1.

Figure 5.19 shows the active power injected by G_1 to the grid during a load change; it can be seen that according to (4.45) when a load change is presented, the ROCOF is multiplied by H_{eq} value, giving a higher active power with higher H_{eq} value. Figure 5.20 presents the active power delivered by the G_2, being smoother with higher H_{eq} value.

In the case 2 the G_1 is replaced by the BESS, in this case in t = 125 s the load $P_{L2} =$ 100 kW is connected. Figure 5.21 presents the frequency response under different H_{eq} values for case 2, while a close-up of the nadir of the frequency is shown in Figure 5.22. As can be seen like in the case 1 with higher H_{eq} value, the frequency nadir becomes

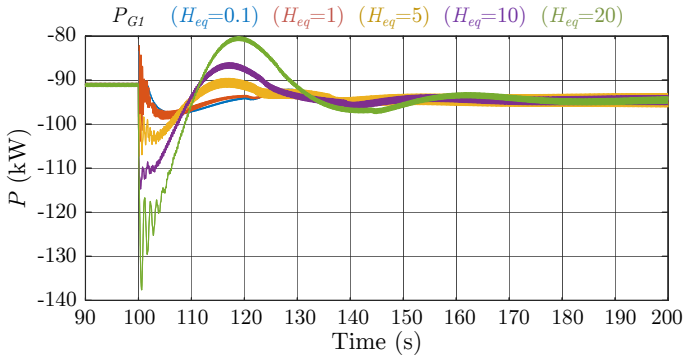

Figure 5.19: Active power generation response from G_1 under different H_{eq} values for case 1.

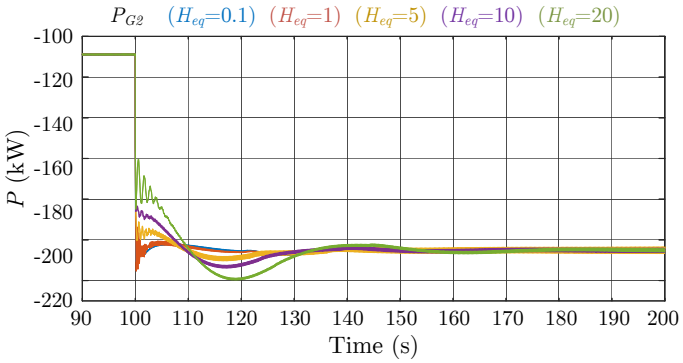

Figure 5.20: Active power generation response from G_2 under different H_{eq} values for case 1.

closer to the f_0.

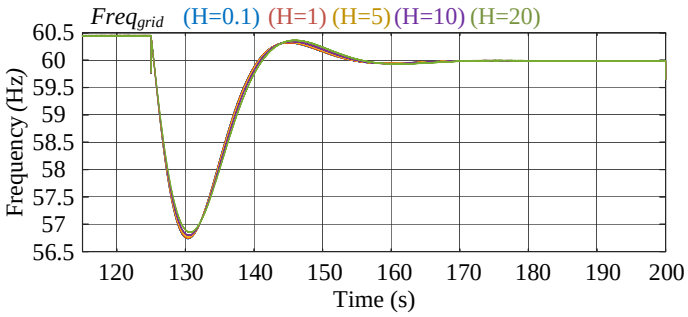

Figure 5.21: Frequency response under different H_{eq} values for case 2.

Besides, the behavior of the power delivered by BESS, according to (4.45), can be seen in Figure 5.23, and can be observed the qualitative behavior similar to the synchronous machine (Figure 5.19).

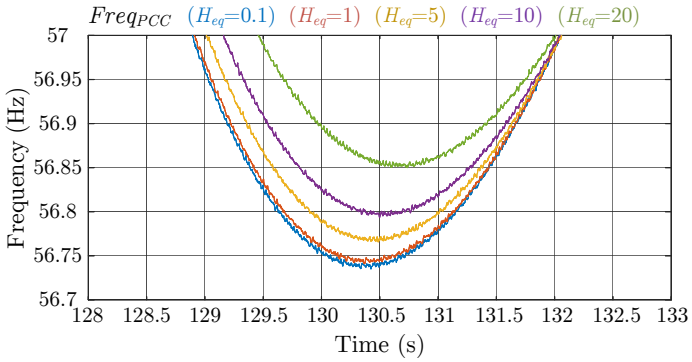

Figure 5.22: Close-up of the nadirs of Figure 5.21.

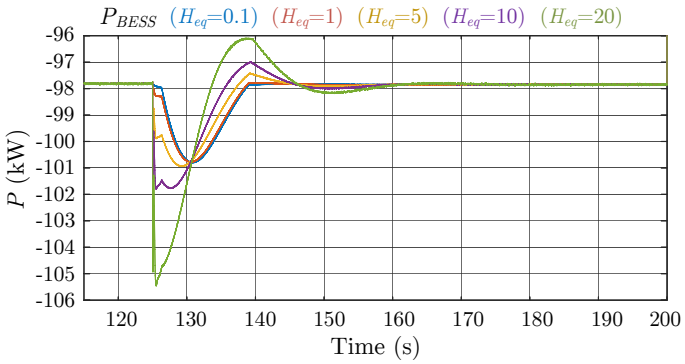

Figure 5.23: Active power generation response from BESS under different H_{eq} values for case 2.

Figure 5.24 presents the active power delivered by the G_2 for case 2, being smoother with higher H_{eq} value.

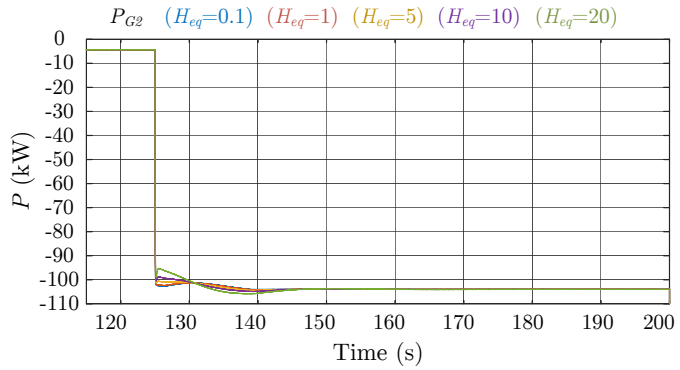

Figure 5.24: Active power generation response from G_2 under different H_{eq} values for case 2.

5.4 Simulation results with the second tuning

Consider the BESS scheme shown in Figure 5.25 for 617 W of rated power and duty class II [66], which is configured in the PSCAD/EMTDC software, to illustrate how the BESS performs with the second tuning. The power of 617 W used for this second tuning is because the validation is also tested in a prototype of that power. The parameters and specifications of the BESS are shown in Table 5.5, along with the controller gains.

The timeline for commuting through all proposed operation modes and load steps is shown in Table 5.6. To accomplish the test protocol according to the timeline, the BRK_1 at the PCC switches between grid-connected and islanded modes. The local load steps are handled by BRK_2 and BRK_3. While SW_1 commands the turning off the DC source, this command implies that the DC/AC converter should regulate V_{DC}, SW_2 and SW_3 command the load steps in the DC bus V_{DC}.

The simulations are presented as follows:

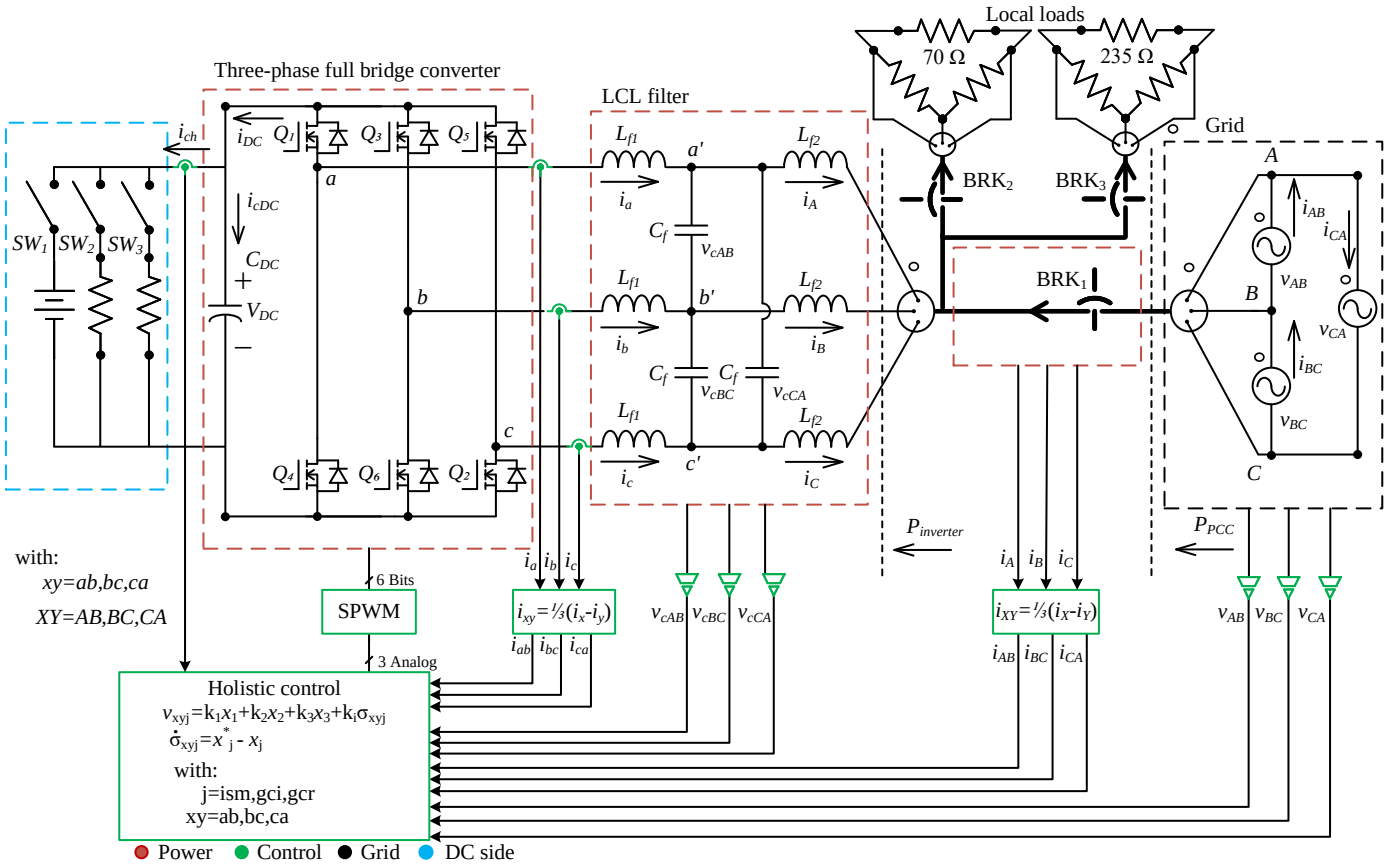

Figure 5.25: Whole BESS scheme used for simulations.

Table 5.5: Electrical specification and parameters for the second tuning.

Specifications/parameter	Value
Grid voltage (AC: L-L, RMS)	$120\,V$
Rated power	617 W
Power factor	Near to unity
V_{DC}	$300\,V$ ($\pm 3\%$)
THD of current (i_{AB}, i_{BC}, i_{CA})	$< 5\%$
THD of voltage (v_{AB}, v_{BC}, v_{CA})	$< 5\%$
Switching frequency	12 060 Hz
Delta-LCL filter: (L_{f1}, L_{f2}, C_f)	(1.59 mH, 530.95 μH 2.60 μF)
Tuning gains	$\mathbf{k} = \begin{bmatrix} -166.17 & 283.86 & 7.30 \end{bmatrix}$ $\mathrm{k_i} = -230.63 \times 10^3$

Table 5.6: Test protocol according to timeline.

Time (s)	Mode	$P_{\text{base}} = 617$ W	BRK_1	BRK_2	BRK_3
0 − 0.1	Grid-connected (inverter) mode	−1.47 p.u.	Closed	Closed	Open
0.1 − 0.3	Grid-connected (inverter) mode	−1.11 p.u.	Closed	Closed	Open
0.3 − 0.5	Islanded mode	−1.11 p.u.	Open	Closed	Open
0.5 − 0.7	Islanded mode	−1.44 p.u.	Open	Closed	Closed
0.7 − 1.0	Islanded mode	−1.11 p.u.	Open	Closed	Open
1.0 − 1.2	Grid-connected (inverter) mode	−1.11 p.u.	Closed	Closed	Open
1.2 − 1.6	Grid-connected (rectifier) mode	1.07 p.u.	Closed	Closed	Open
1.6 − 2.0	Grid-connected (rectifier) mode	1.31 p.u.	Closed	Open	Open

5.4.1 Timeline from 0 to 1.2 s

This timeline section taken from Table 5.6 is used to demonstrate operation mode changes, load steps, and reference changes, always working as an inverter.

As can be seen in Figure 5.26 first, from 0 s to 0.1 s, the closed-loop inverter works delivering -1.47 p.u. of active power at the $P_{inverter}$ node, where the negative sign indicates that the power flow is coming out of the inverter. Since BRK_1 is closed, there

is a local load consumption of 1 p.u., therefore, in the P_{PCC} only -0.47 p.u. are being injected into the electrical power system. In 0.1 s, a reference change occurs. Second, from 0.1 s to 0.3 s the power delivered by the inverter to the $P_{inverter}$ node is -1.11 p.u because the three breakers remain in the same position, the local load of 1 p.u. is kept, therefore, in the P_{PCC}, only -0.11 p.u. are being injected to the electrical power system. Next an operation change from grid-connected mode to islanded mode take place at t = 0.3 s, where now the P_{PCC} is 0 and the $P_{inverter}$ is -1.11 p.u. Then, two local load steps occur at t = 0.5 s and t = 0.7 s being -1.44 p.u. and -1.11 p.u. the power delivered to the local loads, respectively. Finally, an operation change from islanded mode to grid connected mode occurs at t = 1.0 s with a power of -1.11 p.u.

The power factor should remain above 0.95% in steady state, according to the IEEE 157-2018 standard. The performance of this parameter is shown in Figure 5.27, which fulfill with the aforementioned in steady state. It is significant to note that the power factor reaches unity when the islanded mode is operating because the load is purely resistive.

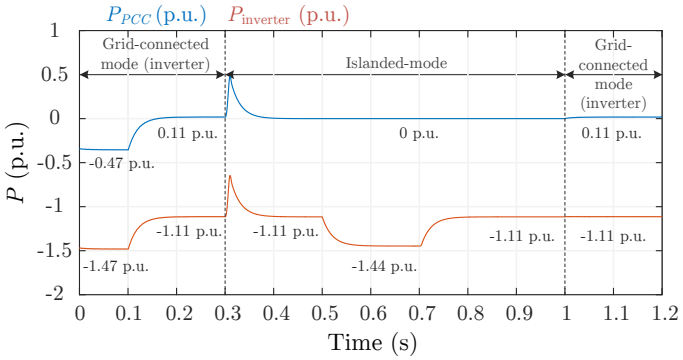

Figure 5.26: Active power duty class during timeline from 0 s to 1.2 s.

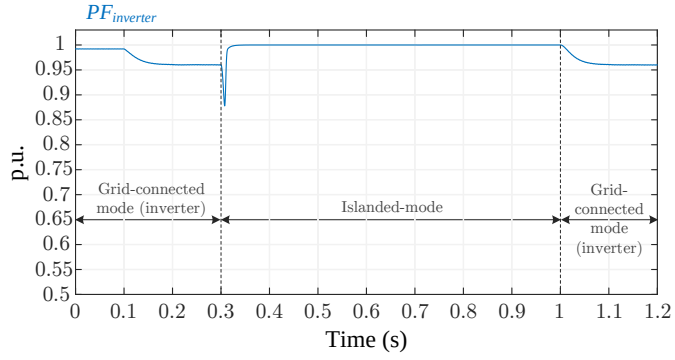

Figure 5.27: Power factor from timeline 0 s to 1.2 s.

The THD of voltage and current are other parameters associated with power quality

and required by IEEE 1547-2018. Figure 5.28 depicts the voltage THD at the top and the current THD at the bottom. As can be seen, both values remains within the limits specified in Table 5.5 for steady state.

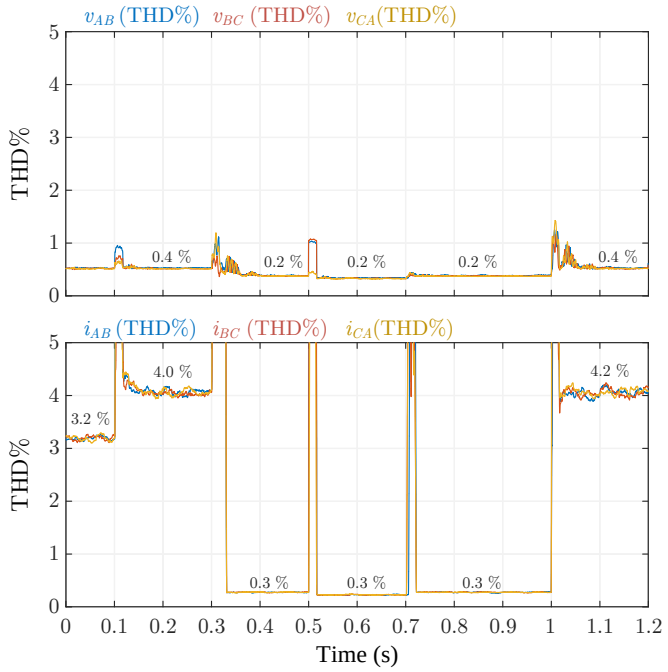

Figure 5.28: Voltage and current THD from timeline 0 s to 1.2 s.

Figures 5.29 and 5.30 show the transient that occurs in voltage and current for operation changes between grid-connected and islanded mode, respectively. Observe that Figure 5.30 on the left shows a strong current variation during the transient. That phenomenon is explained because at the beginning of the test the reference of the inverter is current and the grid voltage dominates the performance of the capacitor voltage at v_{cAB}, besides this mode change implies a change of reference from current to voltage; so the current stops being controlled producing that variation shown on the left side of Figure 5.30. Following the same idea, the voltage begins to be controlled due to the reference change, which can be observed as a minimum effect on the left side of Figure 5.29. This phenomenon does not occur on the right side of Figures 5.29 and 5.30 because the grid imposes its strong over the capacitor voltage.

To illustrate the grid-connected performance when load steps occur, Figures 5.31 and 5.32 display the evolution of the voltage and current, respectively. On the left side of these figures it is shown the performance facing load steps during the grid-connected (inverter) mode. On the right the islanded-mode behavior is shown. It can be seen that the reference tracking control is suitable.

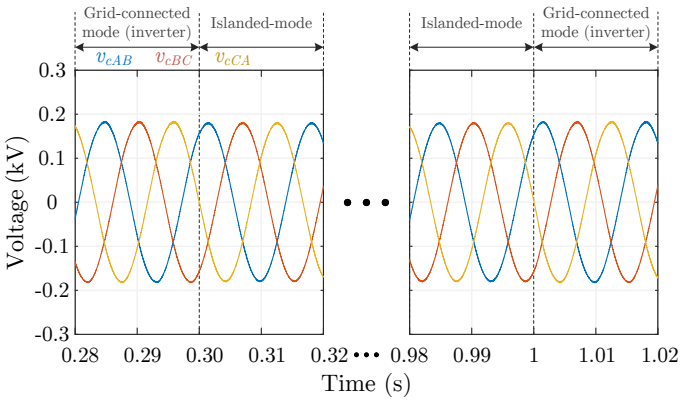

Figure 5.29: Voltage transients when mode changes occur.

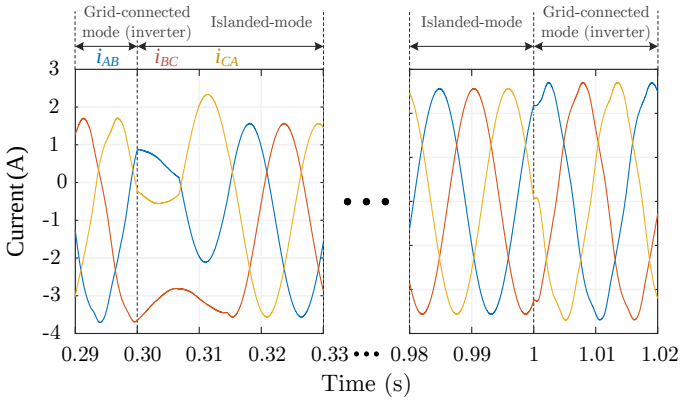

Figure 5.30: Current transients when mode changes occur.

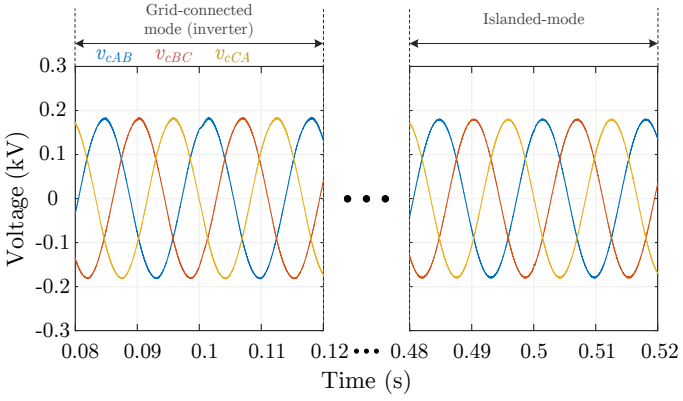

Figure 5.31: Voltage transients when load changes occur.

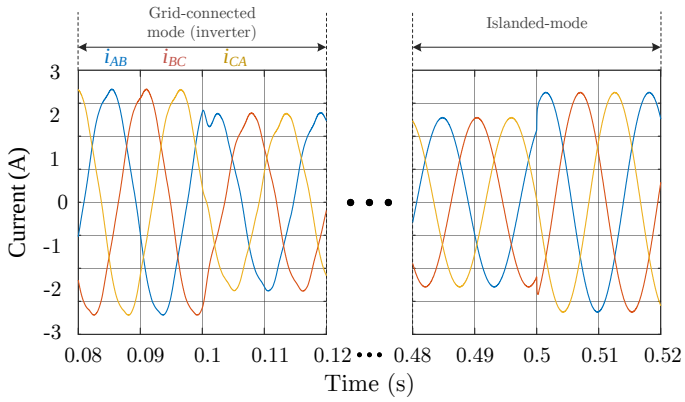

Figure 5.32: Current transients when load changes occur.

5.4.2 Timeline from 1 to 2 s

This timeline considers an operation change from grid-connected (inverter) to grid-connected (rectifier) modes, including a load step.

The following simulations confirm the holistic feature of the closed-loop grid-connected converter working as a rectifier.

In Figure 5.33 the DC capacitor voltage V_{DC} is shown to validate the capability of the proposed controller to maintain the DC voltage regulated around $V_{DC}^{*} = 300\,V$. It can be observed that as for mode changes as for load steps the DC voltage is regulated out of the threshold of ±3% required in Table 5.5. Being 4.60% and 5.47% at 1.07 p.u. and 1.31 p.u., respectively. This evidence of DC voltage error indicates that the reference for calculating it should be refined considering the parasitic influence of the LCL filter when (4.1) and (4.2) are equalized (the DC and AC powers). This evidence of DC voltage error indicates that the reference for calculating it should be refined considering the parasitic influence of the LCL filter when (4.1) and (4.2) are equalized (the DC and AC powers). The difference regarding the previous controller is that the parasitic elements were not considered, while for the second tuning, they were considered thinking in the implementation of the prototype.

In Figure 5.34 the power performance is plotted to show the capability to change from grid-connected (inverter) mode to grid-connected (rectifier) mode fulfilling the duty class II. It is important to observe Figures 5.33 and 5.34 and to notice that during the power transients the DC voltage regulation is maintained.

The power factor is a relevant parameter to be accomplished in all the operation modes. Thus, Figure 5.35 presents the grid-connected mode (rectifier) power factor performance. It can be appreciated the capability to maintain a high power factor in steady state over 0.95 and near to 1.

The voltage and current harmonic distortions are important in the grid-connected (rectifier) mode. Hence, Figure 5.36 shows at the top the THD voltage while at the bottom the THD current. It is possible to notice that during the steady state of the

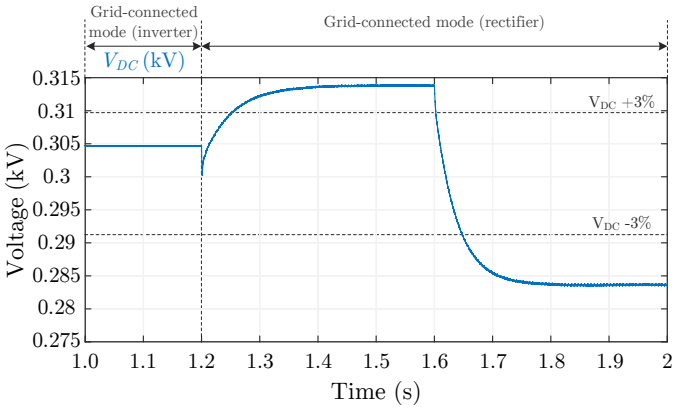

Figure 5.33: Voltage V_{DC}, from 1.0 s to 2.0 s.

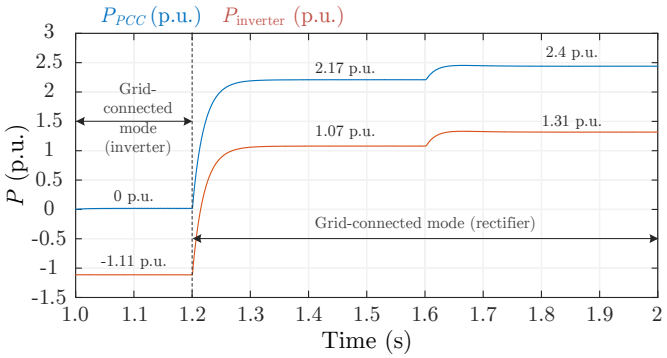

Figure 5.34: Active power duty class during from 1.0 s to 2.0 s.

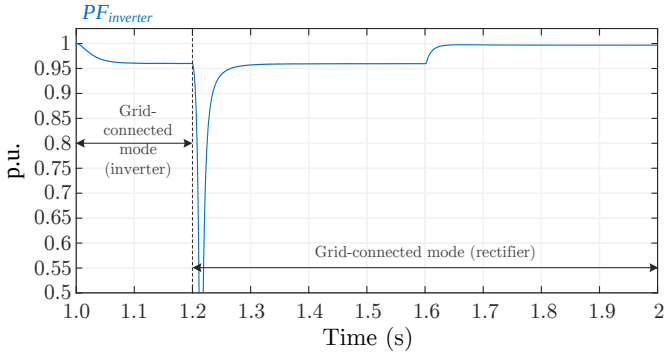

Figure 5.35: Power factor from 1.0 s to 2.0 s.

test, the limits established in Table 5.1 are satisfied.

In Figures 5.37 and 5.38, the instantaneous voltage and current when an operation mode change from inverter to rectifier occurs at $t = 1.2$ s and a load transient occurs at

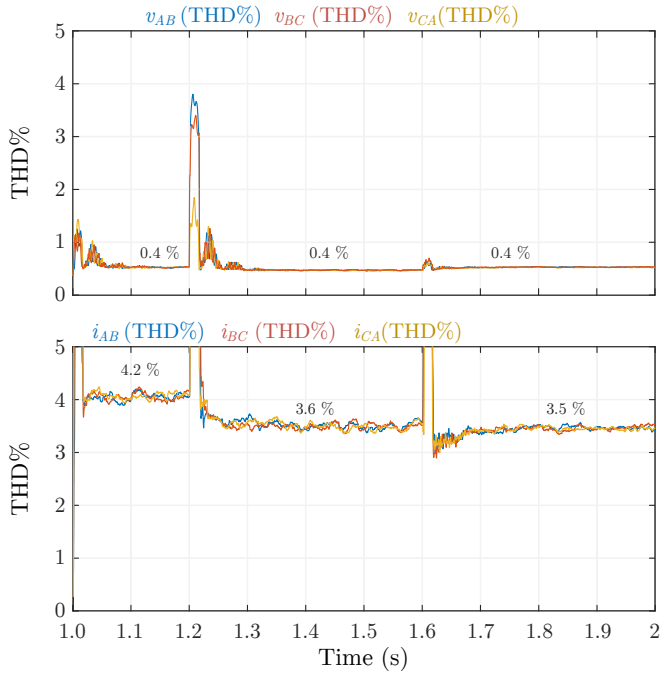

Figure 5.36: Voltage and current THD from 1.0 s to 2.0 s.

$t = 1.6$ s, are shown respectively.

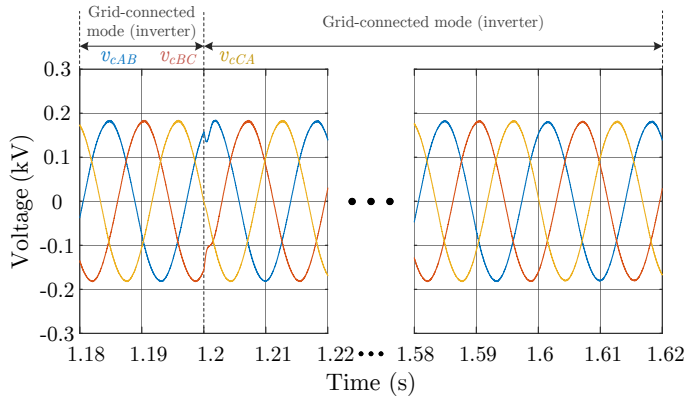

Figure 5.37: Voltage transients when a mode change occurs and when load changes occur.

It can be appreciated the adequate response of the grid-connected converter for both, mode changes and load transients in rectifier mode.

Table 5.7 summarizes the electrical specifications achieved by using the second tuning. It can be observed the capability to cover satisfactorily each mode according to Table 5.5.

Table 5.8 reveals the relevant features of the holistic control, the features are

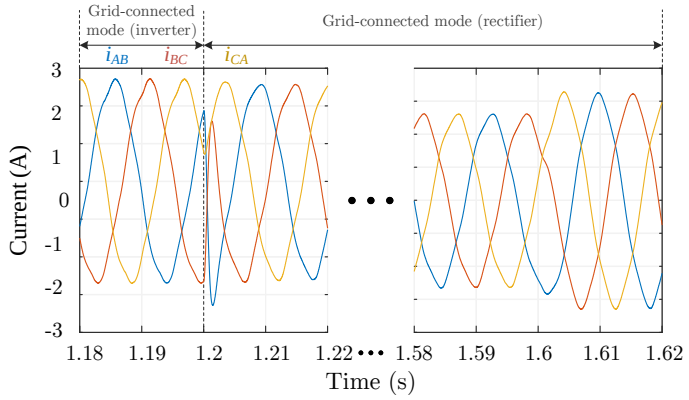

Figure 5.38: Current transients when a mode change occurs and when load changes occur.

Table 5.7: Electrical specifications achieved for each mode.

$P_{inverter}$ $P_{\text{base}} = 617$ W	Specification	Islanded mode	Grid-connected (inverter) mode	Grid-connected (rectifier) mode
1.0 p.u.	P.F.	1	0.96	0.95
1.0 p.u.	$\text{THD}_{\text{current}}$	0.30%	4.00%	3.60%
1.0 p.u.	$\text{THD}_{\text{voltage}}$	0.20%	0.40%	0.40%
1.0 p.u.	$\text{Error}_{V_{DC}}$	NA	NA	4.60%
1.5 p.u.	P.F.	1	0.99	1.00
1.5 p.u.	$\text{THD}_{\text{current}}$	0.30%	3.20%	3.50%
1.5 p.u.	$\text{THD}_{\text{voltage}}$	0.20%	0.40%	0.40%
1.5 p.u.	$\text{Error}_{V_{DC}}$	NA	NA	5.47%

basically the same with exception of the reference although certainly, references are not part of the controller tuning.

Table 5.8: Holistic control features.

Features	Islanded mode	Grid-connected (inverter) mode	Grid-connected (rectifier) mode
DQ frame transformation	No	No	No
Double-loop controllers	No	No	No
Different control schemes	No	No	No
References	v^*_{cAB}	i^*_{AB}	i^*_{AB}
Tuning constant k_1	-166.17	-166.17	-166.17
Tuning constant k_2	283.86	283.86	283.86
Tuning constant k_3	7.30	7.30	7.30
Tuning constant k_i	-230.63×10^3	-230.63×10^3	-230.63×10^3

5.5 Simulation results with the second tuning fulfilling IEEE 1547-2018 ride-through

In this section simulation results are faced to the IEEE 1547-2018 by using the test protocol given in Table 5.6. According to this protocol, the PCC frequency lies within the thresholds established by the "continuous operation capability" of the IEEE 1547-2018 abnormal frequency ride-through for DER's, as can be seen in Figure 5.39. In Figure 5.40 can be seen that the PCC voltage lies within the thresholds established by the "continuous operation capability" of the IEEE 1547-2018 abnormal voltage ride-through for DER's.

For this thesis the meaning of a seamless transition among modes in accordance with IEEE 1547-2018, occurs if the transients do not exceed the threshold for continuous operation.

5.6 Simulation results with the second method of virtual inertia

For the second method of virtual inertia, the BESS was implemented using the software in the loop concept by using the OPAL real-time simulator OP4510. The procedure for programming the power system shown in Figure 5.41 and holistic control with virtual

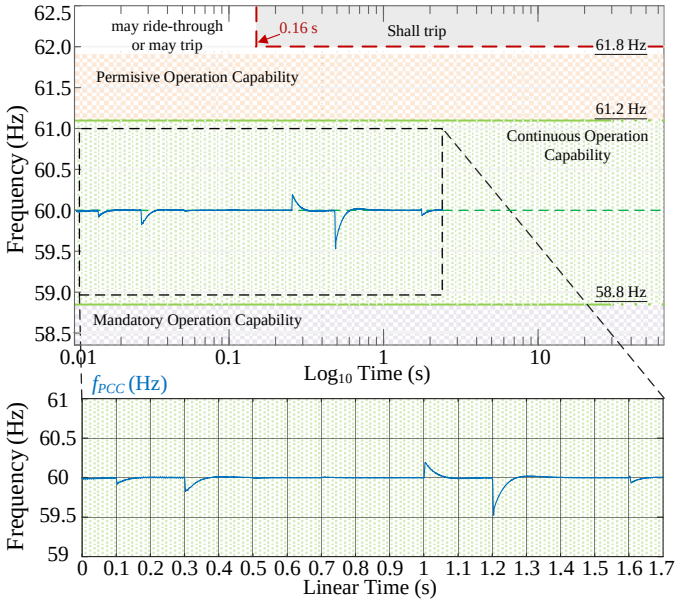

Figure 5.39: System response on frequency measured at the PCC.

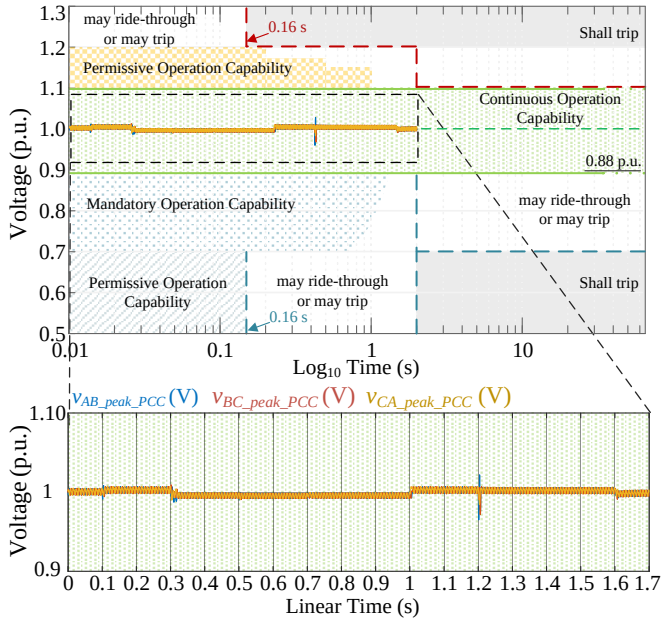

Figure 5.40: System response in the voltage amplitude measured at the PCC.

inertia in the OPAL-RT simulator is by using the MATLAB SIMULINK software.

The conventional two-generator power system network shown in Figure 5.41 is used to validate the efficacy of adding virtual inertia as extra ancillary service to the BESS. This system is usually used to illustrate the operating principle of virtual inertia [68]. The benchmark of the Figure 5.41 was used because of its suitability to be implemented as software in the loop.

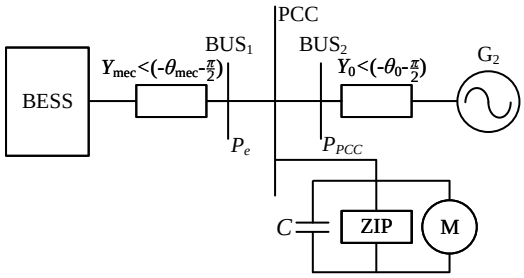

Figure 5.41: Power system model with the BESS.

The system is composed by two buses and one load. The first bus hosts the BESS, the second bus hosts a slack bus generator, and the combination of three loads is nonlinear and is connected to the PCC.

In Figure 5.42 and Figure 5.43 the frequency and the RoCoF of the system are depicted, respectively. It can be seen that at 5 s a load step caused by an asynchronous machine torque occurs.

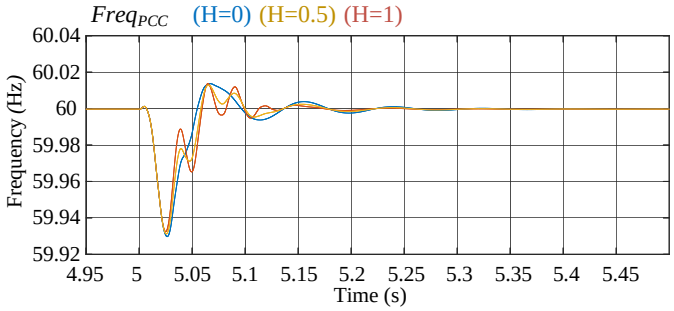

Figure 5.42: Frequency response under different H values.

Analyzing the previous results, they need to be more conclusive regarding virtual inertia since the depth of the nadir does not change beyond a few tenths of Hertz. Nevertheless, it should be firmly stated that the whole design of the controller was carried out in a concatenated manner with the LCL interconnection filter. This controller is located at the zero level of the hierarchical controller, which is the base of the other levels. Thus, the zero level of hierarchical control follows the power references given by the higher levels, including extra ancillary services. Therefore, the conclusion is that there is an opportunity to improve the calculation of the reference given for the creation of virtual inertia. Until this point of the thesis work, the evidence indicates

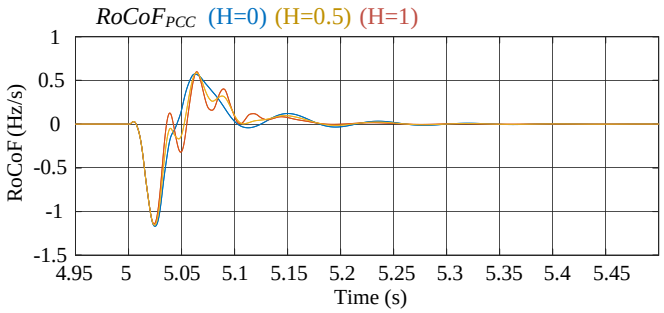

Figure 5.43: RoCoF response under different H values.

that the problem for creating this reference lies in measuring the frequency of the electrical power system, which must be of the best possible quality.

5.7 Experimental results with the second tuning

The prototype implementation is described in Appendix B.

The behavior of the system with the second tuning of the holistic control will be validated through a laboratory implementation for conceptual testing, as shown in Figure 5.44 and taking into account Table 5.5. Furthermore, the description of the prototype experiment is as follows:

- SiC mosfet assembly with three KIT8020CRD8FF1217-P power inverters.
- Air core was used to build the inductors.
- 400 V, polypropylene capacitor.
- The dSPACE platform CP1103 is used to program the controller.

The transition modes highlighted in gray in Table 5.6 have been used to evaluate the seamless transition experimentally; the change of operation from grid-connected (inverter) mode to islanded mode occurs at 0.3 s, and vice versa at 1.0 s, then a change of operation from grid-connected (inverter) mode to grid-connected (rectifier) mode occurs at 1.3 s.

Figure 5.45 shows the measured waveforms of chosen variables when the DC/AC converter changes from grid-connected (inverter) mode to islanded mode. Channel 1 in navy blue shows the frequency of the voltage at PCC, channel 2 in cyan shows the v_{ABrms}, and channel 3 in magenta shows the v_{AB}. Channel 4 in the green line shows the current operating mode of the BESS.

With the same channel ordering as in Figure 5.45, Figure 5.46 shows the DC/AC converter transition from islanded mode to grid connected (inverter) mode.

The change from grid-connected (inverter) mode to a grid-connected (rectifier) mode is shown in Figure 5.47. Channel 1 in navy blue indicates the frequency of the voltage

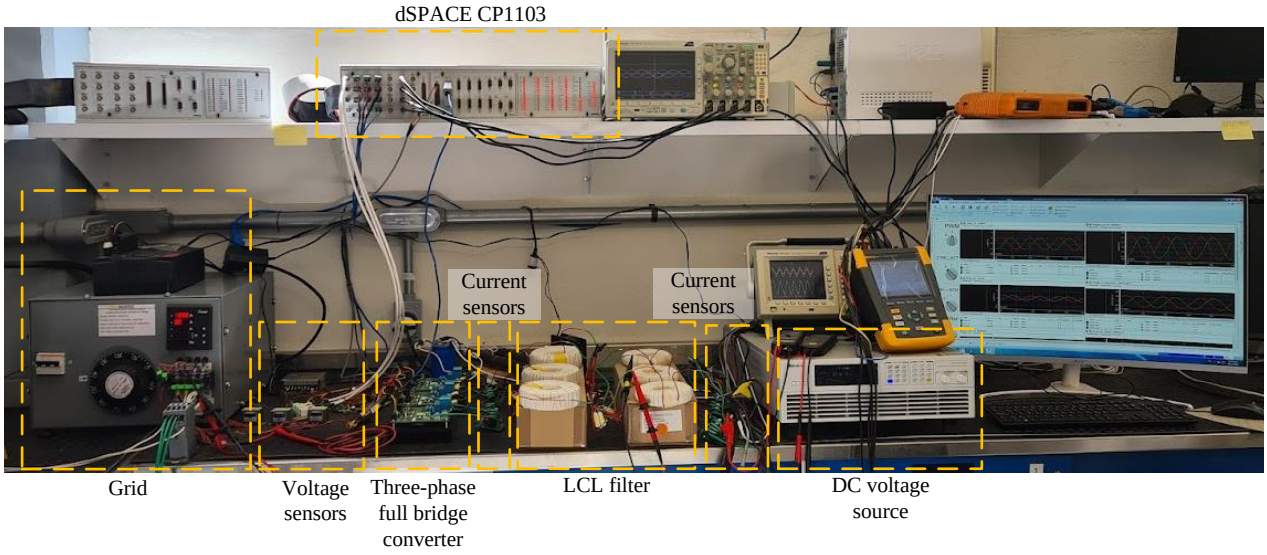

Figure 5.44: Laboratory implementation.

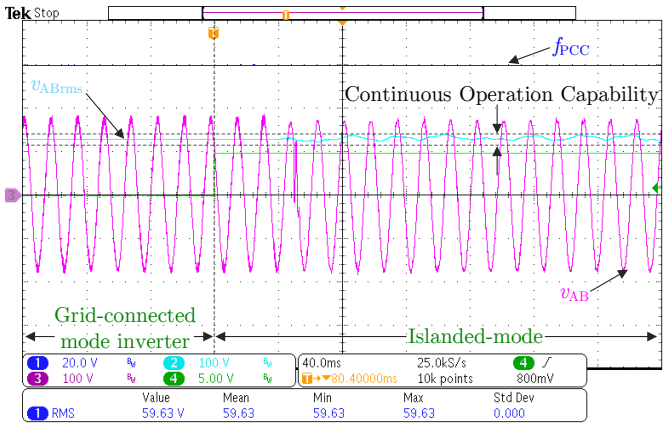

Figure 5.45: The transition from grid-connected mode to islanded operation mode on the prototype.

at PCC, channel 2 in cyan indicates the v_{ABrms}, and channel 3 in magenta indicates the i_{AB}. Channel 4 in the green line indicates the current operating mode of the BESS.

To demonstrate the 180° phase shift caused by the change in current direction caused by the mode transition, the current i_{AB} is shown in Figure 5.47.

It is clear from the three transitions presented in Figures 5.45, 5.46, and 5.47 that the frequency barely experiences a perceptible transient and that the

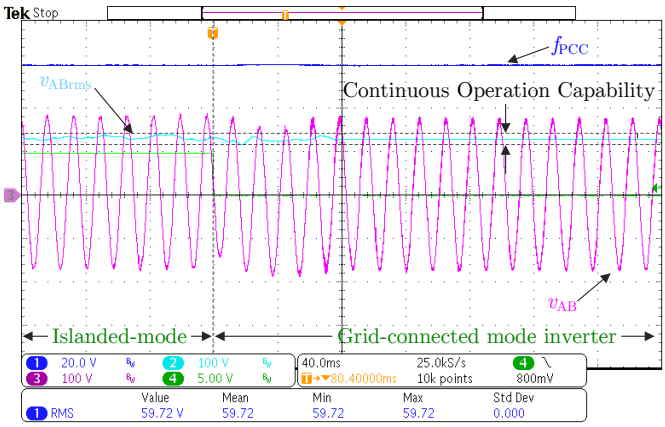

Figure 5.46: The transition from islanded operation mode to grid-connected mode on the prototype.

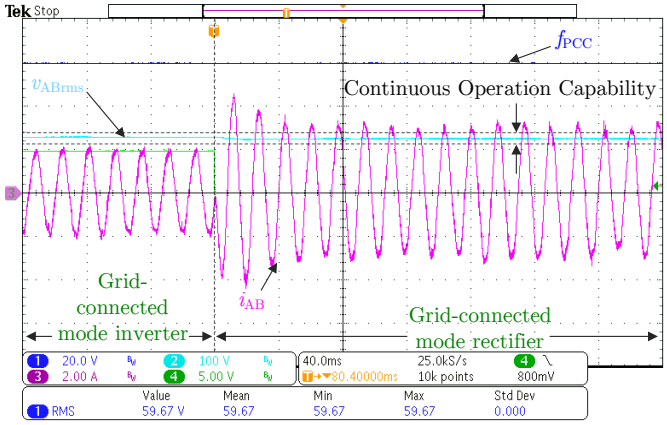

Figure 5.47: The transition of the current from grid-connected mode as inverter to grid-connected mode as rectifier.

voltage amplitude remains within the IEEE 1547-2018 standard "continuous operation capability" thresholds. It is shown that the connection between the LCL filter design and control gains tuning as an integrated design process ensures the seamless transition behavior of the DC/AC power converter at the AC side based on the data presented in this section.

Based on the previous results, it is clear that the experimental results reproduce similarly the behavior presented in simulation results, which confirms the advantages of the concatenated filter design plus the tuning controller.

It is important to highlight that the linear controller works adequately for the grid-connected (rectifier) mode even before operating changes derived from load steps. This result is a relevant simplification of the control concept for the nonlinear system (rectifier).

5.8 Analytical energy consumption comparison between tuning methods

The following analytical evaluation is performed in the closed-loop mathematical model by using MATLAB SIMULINK to demonstrate how a small change in the controller tuning can become so important in the system transients.

The first step is to match the design of the first and the second approach shown above, taking as a reference the parameters of the prototype of 617 W and 120 V_{L-L}. In this section, the subscript "holistic" corresponds to the first tuning, while the "improved holistic" corresponds to the second tuning. For the first tuning, matrices $\hat{\mathbf{A}}$, are given as:

$$\hat{\mathbf{A}}_{\mathrm{ism_{holistic}}}=\begin{bmatrix} -46.14 & 10.19 & -1.07 & 13408 \\ 0 & -43.94 & 0.62 & 0 \\ 1153.60 & -1153.60 & 0 & 0 \\ 0 & 0 & -0.001 & 0 \end{bmatrix} \times 10^3 \tag{5.1}$$

$$\hat{\mathbf{A}}_{\mathrm{gci_{holistic}}}=\begin{bmatrix} -46.14 & 10.19 & -1.07 & 13408 \\ 0 & -43.94 & 0.62 & 0 \\ 1153.60 & -1153.60 & 0 & 0 \\ 0 & -0.001 & 0 & 0 \end{bmatrix} \times 10^3 \tag{5.2}$$

$$\hat{\mathbf{A}}_{\mathrm{gcr_{holistic}}}=\begin{bmatrix} -46.14 & 10.19 & -1.07 & 13408 \\ 0 & 0 & 0.62 & 0 \\ 1153.60 & -1153.60 & 0 & 0 \\ 0 & -0.001 & 0 & 0 \end{bmatrix} \times 10^3 \tag{5.3}$$

with:

$$\begin{aligned} \mathbf{k}_{\mathrm{holistic}} &= \begin{bmatrix} -48.72 & 2.20 & 4.16 \end{bmatrix} \\ \mathrm{k_{i_{holistic}}} &= -64.07 \times 10^3 \end{aligned} \tag{5.4}$$

For the second tuning, the matrices $\hat{\mathbf{A}}$ and gains $[\mathbf{k}\ \mathrm{k_i}]$ were taken from Section 4.3.

Table 5.9 presents an analytical comparison of the two tuning designs to show the advantages of the second one, which considers a complete Butterworth tuning.

Furthermore, a test protocol with input steps, mode changes, and load steps is carried out according to the Table 5.10 timeline to demonstrate the benefits of each gain tuning regarding the required energy to deal with the transients. Equation (4.31) was programmed in Matlab Simulink to run the protocol test.

The BESS operating philosophy implies an effort to enhance both performances, the transient response velocity and the energy transfer. As a result, Table 5.10 shows that the proposed second tuning design reduces the required energy during transients, as can be seen in columns 4 and 5.

To give an analytical comparison, a suggested definition of energy efficiency is given by:

$$\eta = \frac{E_{\text{holistic}} - E_{\text{improved\_holistic}}}{E_{\text{holistic}}} \times 100\% \tag{5.5}$$

with:

Table 5.9: Analytical comparison of holistic control approach and improved holistic control approach.

Holistic approach [37]	Improved holistic approach [69]
$M = 1.8$ and $\omega_c = 21.97\,\text{krad/s}$	$M = 1.8$ and $\omega_c = 21.97\,\text{krad/s}$
Closed-loop state-feedback tuning : $\alpha_{\text{i\_ism\_cl}} = M \times \alpha_{\text{i\_ism}}$ for i=1,2,3 $\alpha_{\text{4\_ism\_cl}} = \frac{1}{M} \times \omega_c$	Closed-loop state-feedback tuning : $\alpha_{\text{i\_ism\_cl}} = \lvert\omega_c\rvert\, M \angle \left(\frac{\pi}{2n_{\text{ext}}}(2\text{i} - 1) + \frac{\pi}{2} \right)$ for i=1,2,3,4
$\alpha_{\text{1\_ism\_cl}} = (-39.55) \times 10^3$ $\alpha_{\text{2,3\_ism\_cl}} = (-19.77 \pm j34.25) \times 10^3$ $\alpha_{\text{4\_ism\_cl}} = (-10.98) \times 10^3$ $\lvert\alpha_{\text{1,2,3\_ism\_cl}}\rvert = -39.55 \times 10^3$ $\lvert\alpha_{\text{4\_ism\_cl}}\rvert = -10.98 \times 10^3$	$\alpha_{\text{1,2\_ism\_cl}} = (-36.55 \pm j15.13) \times 10^3$ $\alpha_{\text{3,4\_ism\_cl}} = (-15.13 \pm j36.55) \times 10^3$ $\lvert\alpha_{\text{1,2,3,4\_ism\_cl}}\rvert = -39.55 \times 10^3$
$\mathbf{k}_{\text{holistic}} = \begin{bmatrix} -48.72 & 2.20 & 4.16 \end{bmatrix}$ $\text{k}_{\text{i}_{\text{holistic}}} = -64.07 \times 10^3$	$\mathbf{k} = \begin{bmatrix} -166.17 & 283.86 & 7.30 \end{bmatrix}$ $\text{k}_{\text{i}} = -230.63 \times 10^3$
Root locus of $\alpha_{\text{1,2,3,4\_ism\_cl}}$ 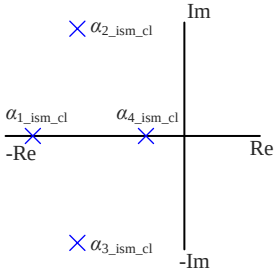 	Root locus of $\alpha_{\text{1,2,3,4\_ism\_cl}}$ 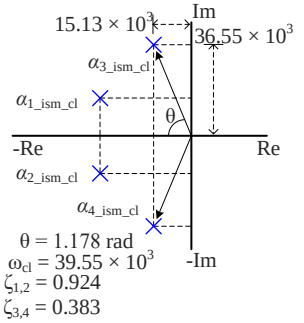
The dominant pole is overdamped, therefore its step response is slow and energy wasting as Figure 5.48 shows.	The dominant poles is under damped, therefore its step response is faster and the energy transferred is improved than [37].

Table 5.10: Test protocol for improved holistic and holistic closed-loop system comparison.

Time (s)	Type of event	Change value according to the event	Holistic energy (J)	Improved Holistic energy (J)	Energy efficiency (%)
0.1	Voltage step ism	$r_{\text{ism}} = 0\text{V}$ to $r_{\text{ism}} = 120\text{V}$	22.58 m	19.87 m	12.00
0.2	Load transient ism	$Z_{AB} = 70\Omega$ to $Z_{AB} = 35\Omega$	16.71 m	12.14 m	27.34
0.3	Mode change ism-gci	$r_{\text{ism}} = 120\text{V}$ to $r_{\text{gci}} = 1.71\text{A}$	1.38	0.42	69.21
0.4	Current step gci	$r_{\text{gci}} = 1.71\text{A}$ to $r_{\text{gci}} = 2.57\text{A}$	4.80	1.48	69.16
0.5	Load transient gci	$Z_{AB} = 35\Omega$ to $Z_{AB} = 70\Omega$	29.08	11.13	61.72
0.6	Mode change gci-gcr	$r_{\text{gci}} = 2.57\text{A}$ to $r_{\text{gcr}} = -1.71\text{A}$	24.22	2.40	90.09

$$E_{\text{improved\_holistic}} = \int_{t_{\text{event}}}^{t_{\text{improved\_holistic}}} |P^*_{ab} - P_{ab\_\text{improved\_holistic}}|\, dt \tag{5.6}$$

$$E_{\text{holistic}} = \int_{t_{\text{event}}}^{t_{\text{holistic}}} |P^*_{ab} - P_{ab\_\text{holistic}}|\, dt \tag{5.7}$$

where:

- $E_{\text{improved\_holistic}}$ is the energy required considering the second tuning.
- E_{holistic} is the energy required considering the first tuning.
- P^*_{ab} is the power at steady state due to the voltage and current reference, respectively.
- P_{ab_holistic} is the power delivered considering the first tuning.
- $P_{ab\_\text{improved\_holistic}}$ is the power delivered considering the second tuning.

- t_{event} is the time at the event occurrence (Column 1 Table 5.10).
- $t_{\text{improved\_holistic}}$ is the settling time where the error is $< 1\%$.
- t_{holistic} is the settling time where the error is $< 1\%$.

The Figure 5.48 shows a voltage step response from $r_{\text{ism}} = 0$ V to $r_{\text{ism}} = 120$ V at 0.1 s to reach the rating power following Table 5.10. The holistic control requires 22.58 mJ, compared to the improved holistic control that requires 19.87 mJ, this last one requires 12.00 % less energy during the transient.

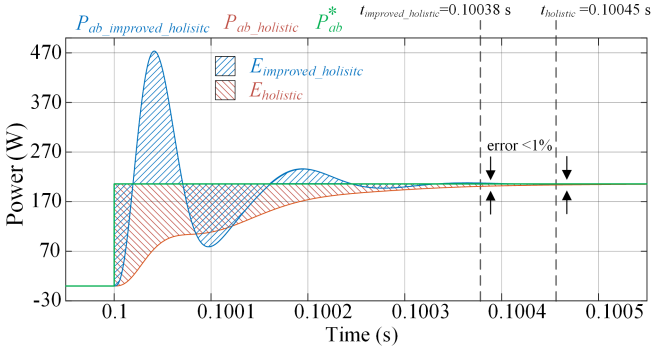

Figure 5.48: Voltage step response in ism going from 0 W to 205.7 W.

In Figure 5.49, a load steps from $P^*_{ab} = 205.7$ W to $P^*_{ab} = 414.4$ W, which leads the system to twice the supplied power, generates a transient at 0.2 s. The holistic control uses 16.71 mJ compared to 12.14 mJ for improved holistic control, using 27.34 % less energy during the transient response.

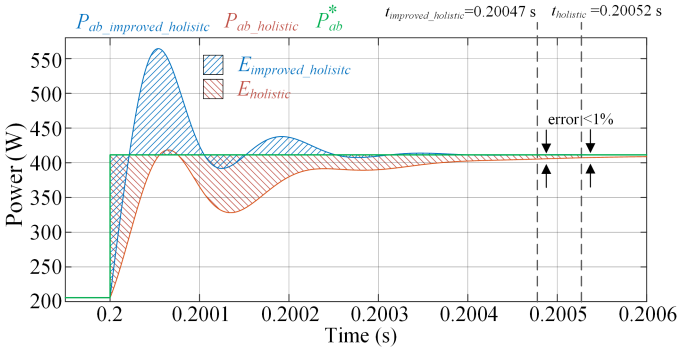

Figure 5.49: Load transient in ism going from 205.7 W to 414.4 W.

Figure 5.50 shows the transition of the inverter from islanded operation to a grid-connected operation mode. In grid-connected (inverter) mode, the reference is a current of $r_{\text{gci}} = 1.71$ A, whereas the reference in islanded mode is a voltage of $r_{\text{ism}} = 120$ V. This implies a power change, with the the holistic control using 1.38 J and the improved

holistic control using 0.42 J, respectively, using 69.21 % less energy during the change mode.

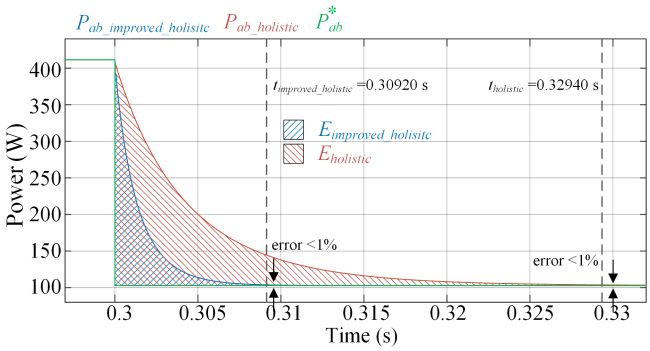

Figure 5.50: Change from ism to gci going from 411.4 W to 102.8 W respectively.

In grid-connected (inverter) mode, a current reference step occurs at 0.4 s, as shown in Figure 5.51, while a load step occurs at 0.5 s, as shown in Figure 5.52. The holistic control consumes 4.80 J in the current step, while the improved holistic control only consumes 1.48 J, resulting in an efficiency of 69.16 %. The holistic control uses 29.08 J during the load transient, whereas the improved holistic control uses 11.13 J, resulting in an efficiency of 61.72 %.

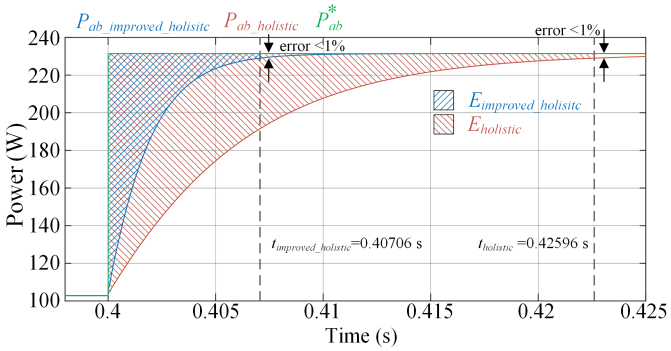

Figure 5.51: Current step in gci going from 102.8 W to 231.4 W.

In order to complete the timeline, a mode change from grid-connected (inverter) mode to grid-connected (rectifier) occurs at 0.6 s. The current reference in grid-connected (inverter) is positive $r_{\text{gci}} = 2.57\text{A}$, whereas it is negative $r_{\text{gcr}} = -1.71\text{A}$ in grid-connected (rectifier), indicating a change in the current direction. Given an energy efficiency of 90.09%, the holistic control, in this case, uses 24.22 J, while the improved holistic control uses 2.40 J.

The most striking finding from the analysis of all the data from the events that were previously presented, was how a slight change in the control tuning, which involves concatenating integrator and state-feedback gains into the Butterworth polynomial,

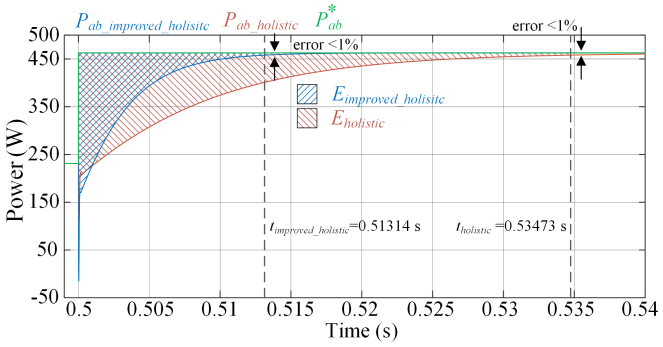

Figure 5.52: Load transient in gci going from 231.4 W to 462.8 W.

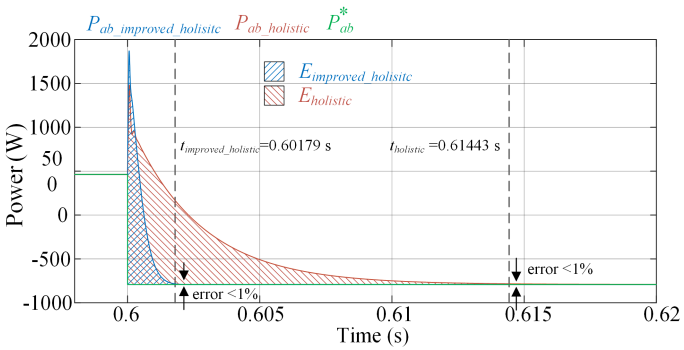

Figure 5.53: Change from gci to gcr from 462.8 W to -791.8 W.

can significantly reduce the amount of energy and transient velocity needed for both mode changes and load transients as well as input steps.

5.9 Results discussion

BESS systems use power electronics converters, which should have multiple operating modes, to transfer, delay, channel, and improve electrical energy. This thesis uses the theory of polynomial filter design [7] to extended its concept for tuning a closed-loop control under the same polynomial premises, allowing the formulation of an integrated design methodology, resulting in the following features:

- Improvement in energy efficiency during mode changes and load changes.
- According to IEEE 1547-2018, which ensures operation in the continuous region restricted by the standard, seamless transition capability is validated.
- One important finding is that, when the converter is used as a rectifier without

tuning modifications, the same polynomial tuning and filter design work as intended.

Figure 5.54 depicts a flowchart with the step-by-step methodology to achieve improved holistic control, summarizing the concatenated design of LCL filter BESS with the closed loop Butterworth polynomial control.

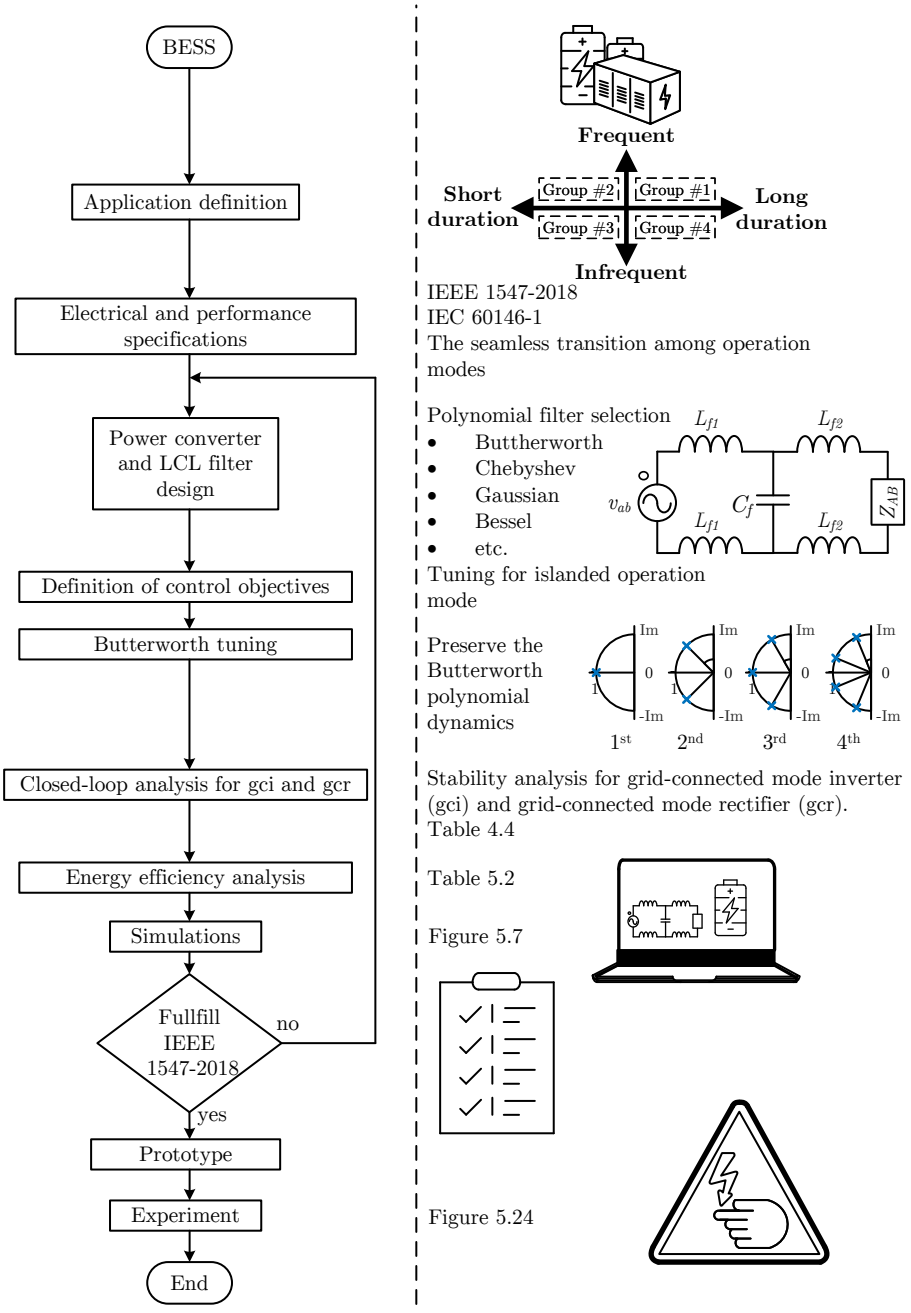

Figure 5.54: holistic control methodology.

Chapter 6

Conclusions

Integrating renewable energy into the electrical power system is a process that requires a high level of control in the energy conversion process. This energy integration occurs between two systems with different time constants. The electrical power system operates at 60 Hz, and the power electronics work at a switching frequency, usually of the kilo Hertz order. The apparently incompatible interaction has generated a whole development of analysis techniques, design procedures, and the development and actualization of regulations and standards, tending to make the different nature of both systems compatible with taking advantage of energy without destabilizing the electrical power system.

This thesis proposes a design methodology for the DC/AC power converter that communicates a BESS to the electrical power system as a result of the aforementioned. In this work, the energy conversion process of the power electronics stage and its passive components are the main topics from the viewpoint of automatic control.

The aim is to determine whether it was feasible to design the LCL filter, which is the primary stage for energy transfer, in a polynomial manner, given the linear nature of the inverter structure. It would bring advantages in the use of energy. However, the input port of the LCL filter is the output port of the inverter, and it is desired to maintain control of this DC/AC conversion stage. Considering the requirements imposed by the application of the BESS interconnected to the power system.

Besides, this thesis work brought up the question of whether it was feasible to control the inverter using the same polynomial theory as the filter. Calling to this procedure a concatenation of the LCL filter design and inverter control. The answer to this question led to the pertinent conclusion that it is possible to combine the polynomial design of the LCL filter with the tuning of the state feedback control with the integrator while maintaining the same dynamic of Butterworth polynomials.

Two distinct tuning modes performed the concatenation in this thesis, but the second tuning made the most significant contribution. When tuning gains are designed, the Butterworth performance is maintained throughout the entire system, and these designs were made with the islanded operation mode in mind. Because the transfer function satisfies the requirement of the dimensional similitude between the input and

output, which refers to the input voltage and output voltage, the island operation mode served as the point of reference. This approach suggests a tuning factor for the closed-loop system while considering the wideband and the switching frequency, which shows how the LCL filter design and control gains tuning are connected as a part of an integrated design process.

In contrast to the first, the second tuning incorporates the integrator of the closed loop in the root locus system to create a complete Butterworth polynomial. The potential for improving energy treatment is the primary motivation behind this slight difference. When the energy requirements are plotted, the results clearly show a difference, showing improved performance that results in significant energy savings that range from 12 % to 90 %. The settling time has also been significantly improved. This finding is relevant when a bulk energy amount needs to be transferred to accomplish power peak shaving, frequency supporting, and islanded operation mode, among others, which inspired the basis for this research.

However, once the concatenated scheme was designed, it was verified that, during the operation in rectifier mode, which is inherently bilinear, it is also possible to control the energy conversion with the same approach, only modifying the current reference channel by a shift of 180° to the current. Finally, once the viability of the method was demonstrated, it was put to the test under the different requirements required by IEEE 1547-2018 for the interconnection of renewable energy resources. It results in a smooth transition between operation modes, step loads, and step references according to the original formulation of the Butterworth polynomial. It is also worth mentioning that this concatenated perspective allows controlling the system using a single control loop, all in the ABC framework.

Publications

- A. Arellanes, N. Visairo-Cruz, C. Núñez and D. Mora, "Controlled Three-Phase LCL- Filter PWM Rectifier with BESS-oriented Applications Under Unbalanced Grid Conditions," 2020 15th IEEE Conference on Industrial Electronics and Applications (ICIEA), Kristiansand, Norway, 2020, pp. 737-742, doi: 10.1109/ICIEA48937.2020.9248209.
- C. Nuñez, N. Visairo-Cruz, A. Arellanes, D. Mora and J. Segundo, "Holistic Control Approach for the Grid-Connected Converter of a Battery Energy Storage System," in IEEE Access, vol. 8, pp. 216844-216855, 2020, doi: 10.1109/ACCESS.2020.3038149.
- A. Arellanes, C. Nuñez, N. Visairo, and A. A. Valdez-Fernandez, "An improvement of holistic control tuning for reducing energy consumption in seamless transitions for a bess grid-connected converter," Energies, vol. 15, p. 7964, 10 2022.

Future work In this thesis, several opportunities for improvement were identified. Therefore several future works can be inferred, such as; For the generation of references

and the synchronization of the control with the power system, a generic PLL was taken. Therefore it remains the following questions, is the PLL the weakest link? How is the performance of the PLL evaluated in the complete system? Could it be included in the complete control scheme? Is it a good idea to add it to the model? Or do a study of the art of the PLL? and make an analysis to design it and that it is negligible in the systems; For the design of the filter in conjunction with the converter, it would be convenient to consider a network equivalent considering the interconnection impedance; Concerning the DC bus, it would also be convenient to consider a non-linear switched load.

Appendix

Appendix A

Table 1 provides a list of recommendations and standards along with their scope and BESS stage target.

Table 1: Recommendations and standards for BESS.

Standard	Scope	stage
IEEE 1547.2-2008	This guide provides technical background and application information to understand the IEEE Std 1547-2003.	Inverter (grid requirements)
IEEE 1547a-2015	Voltage regulation, voltage ride-through, and frequency ride-through are the only three highest priorities that this standard addresses as a standard to 1547.	Inverter (grid requirements)
IEEE 1547-2018	The criteria and requirements for the interconnection of distributed resources (DR) with electric power systems established by this standard (EPS).	Inverter (grid requirements)
ANSI C84.1-2006	The nominal voltage ratings and operating tolerances for 60 Hz electric power systems above 100 V and through 230 kV are established by this standard.	Inverter (grid requirements)
UL-1741-2010	The requirements for converters used in utility-interactive (grid connected) or stand-alone (not connected to the grid) power systems are covered by this standard.	Inverter (grid requirements
AS 4777.2-2005	This standard defines the specifications for inverters used to inject electrical power into the electricity distribution network, with ratings up to 30 kVA for three-phase units or 10 kVA for single-phase units.	Inverter (grid requirements)
IEEE-929-2000	This recommended practice is applicable for PV power systems connected to utilities and running in tandem.	Inverter (grid requirements)
RES/119/2012	The general guidelines for the interconnection of the utility with renewable energy are outlined in this resolution.	Inverter (grid requirements)
CFE LO000-45	The deviation limitations for the current and voltage waveforms are established by this standard.	Inverter (grid requirements)

Continued on the next page

Table 1: Recommendations and standards for BESS (Continued).

Standard	Scope	stage
IEEE-1184-2006	The purpose of this document is to help users select battery systems for uninterruptible power systems (UPS).	Battery bank and grid requirements
NRF-249-PEMEX	The technical specifications for industrial UPS are set forth in this standard.	Battery bank and grid requirements
IEC 60146-1-1	All self-commutated semiconductor converter types are covered by this standard.	Battery bank grid requirements
IEEE 519-2014	This recommended procedure serves as a design manual for power systems with nonlinear loads. The established limitations are suggested for "worst-case" scenarios and are for steady-state operation.	Battery bank grid requirements
IEEE-1184-2006	This guide is intended to assist users who select battery systems for uninterruptible power systems (UPS).	Battery bank requirements
NEMA PE 5-2003	This standard publication addresses stabilized constant-potential, filtered, or unfiltered battery chargers that are intended to deliver DC power from an AC source to charge a float-type battery while also providing power to the linked utility system load.	Battery bank requirements

Appendix B

Prototype implementation

The prototype implementation is presented in three stages, which are: a) Power Stage, b) Digital Processing Stage and c) Instrumentation Stage.

- Power Stage: it is built with devices that handle the power such as: DC controlled source, capacitor bank, three-phase PWM converter and the LCL filter.
- Digital Processing Stage: it consists of the controller board dSPACE CP1103.
- Instrumentation Stage: corresponds to the measurement devices that are: voltage sensors and current sensors in addition to the adecuation card which protects the dSPACE CP1103 from signals that exceed its operating range and avoid its damage.

Development of instrumentation on PCB (sensors)

The instrumentation stage is a very delicate part of the prototype, that is why it was decided to build it on PCB, in order to reduce noise generated by the experimentation tablet, since a small change in any sensor reading creates a large change at system output. This stage consists of six voltage sensors and seven current sensors. Of which its construction will be detailed below.

Current sensor Figure 1 shows the schematic of the current sensor which was implemented in a printed circuit using the L08P050D15 model, which is a hall effect sensor from the TAMURA brand, which is powered by a symmetric source of $\pm 15\,V$ and has a high immunity to noise, so combined with its linear output signal it is a reliable option for the project. Figure 2 shows a picture of the finished PCB with the

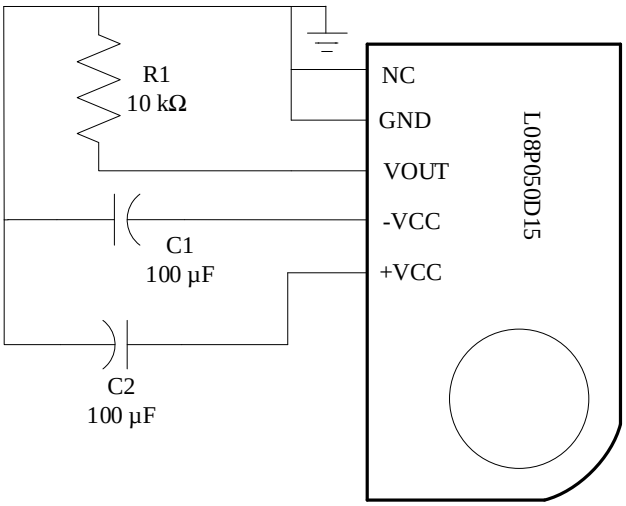

Figure 1: Current sensor PCB board schematic.

current sensor indicating where its power is connected and where its output voltage is obtained.

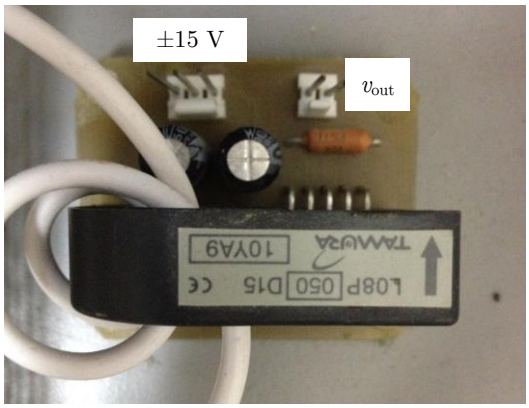

Figure 2: Current sensor PCB.

The sensor tests were performed with a resistive load connected to the electrical network. In the oscilloscope, a comparison was made of the sensor's output voltage, with the current that passed through the sensor, measured by means of a hall-effect clamp, fluke AC / DC, as shown in Figure 3 and in which we can see that the Sensor works as specified in the data sheets provided by the manufacturer.

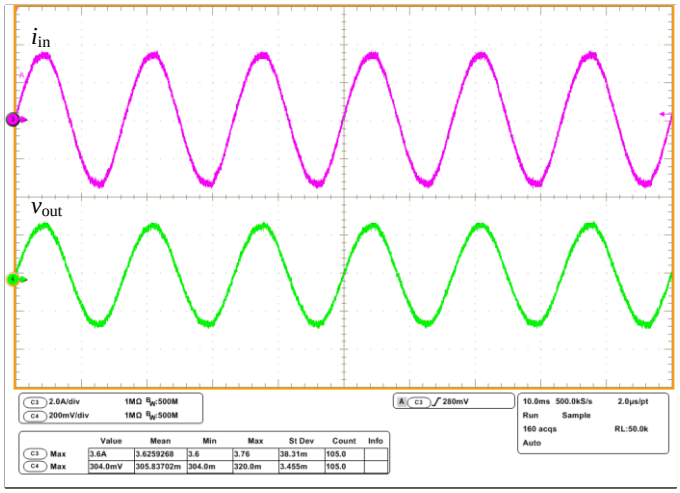

Figure 3: Input current and output voltage at the current sensor.

Voltage sensor For the voltage sensor, the HCPL-7800 high rejection isolating amplifier was used to isolate the control stage from the power stage, a variable voltage divider is used at the input of the circuit in which changes are made by means of a switch jumper type by varying the interconnection of the resistors to adapt the input signal.

An operational amplifier OP27 configured as a low pass filter is used in the output stage to eliminate the high frequency noise that can be generated in the acquisition process of the voltage sensing circuit. For the circuit and to maintain an isolation between the two stages, two power supplies are required, one for the $\pm 15\,V$ op amps and the other for the $5\,V$ power supply of the HCPL-7800. In Figure 4 we can see the schematic of the voltage sensor. The voltage sensor circuit was made on a PCB and taking the necessary precautionary measures to maintain optimal insulation and keeping the input and output stage tracks in separate blocks.

A first order low pass filter implemented by means of a low noise operational amplifier OP27 is located in the output part. This is to suppress the high frequency noise that could result in the attenuation and isolation process. Two independent power supplies are required to retain the isolator character. In the input stage, the integrated circuit HCPL-7800 is fed with a $5\,V$ source. A $\pm 15\,V$ source is connected to the output, for the operational amplifier; the positive part is regulated by the LM7805 integrated circuit for the output section of the HCPL-7800 that consumes $5\,V$.

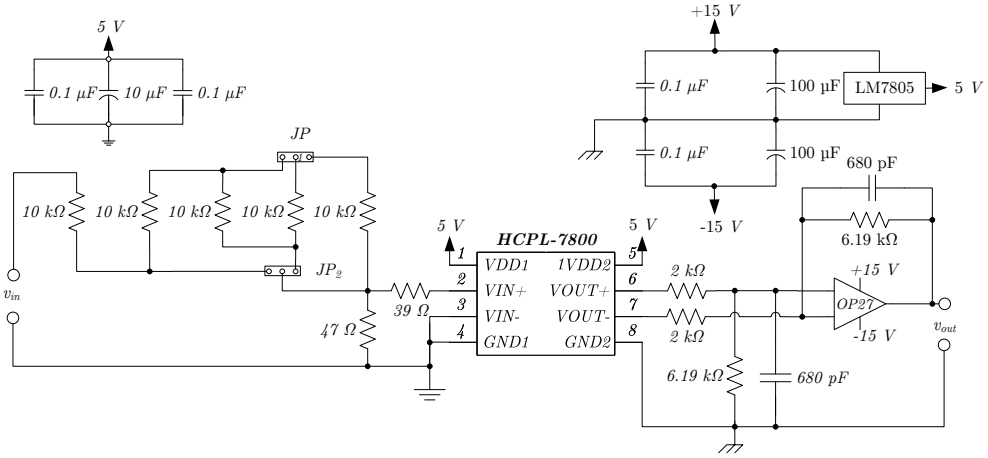

Figure 4: Whole BESS scheme used for simulations.

The final voltage sensor PCB can be seen in Figure 5.

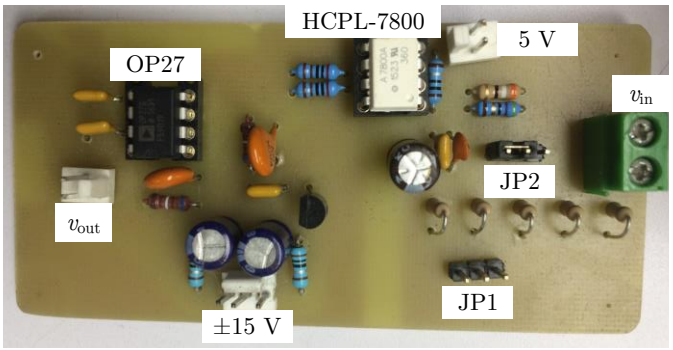

Figure 5: Voltage sensor board.

Development of instrumentation on PCB (protection circuit)

Once the signals have been acquired through the sensors, it is necessary to adjust them to values that the next stage, the control stage, can recognize. In addition, due to the sensitivity of the processor that is in charge of control, it is necessary to establish criteria required by the DSP for the input signals to its analog port, such as: The data sheet of the CP1103 card, used for control, specifies that the Input signals to the analog port must not exceed the range of 0 to $\pm 10\,V$.

The mains voltage signal was input to the v_{in} and both input and output were

measured. The screenshot obtained with the Tektronix oscilloscope is shown in Figure 6. It shows the input and output signals at the voltage sensor. It can be seen that the peak voltage values are 176 V and 5.4 V respectively.

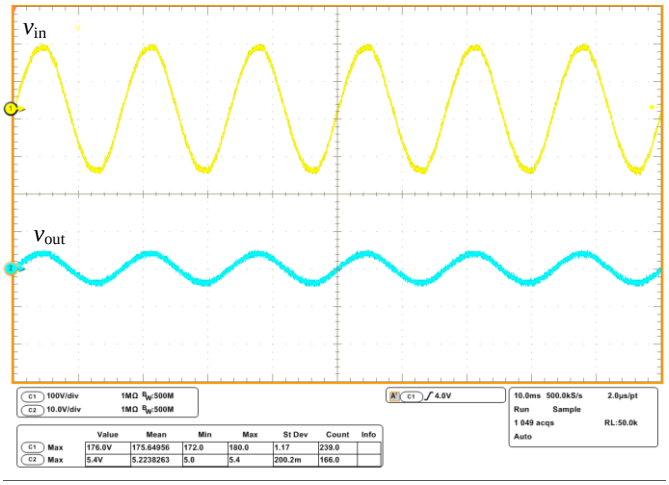

Figure 6: Voltage sensor input signal compared to output signal.

For this, the circuit in Figure 7 was designed.

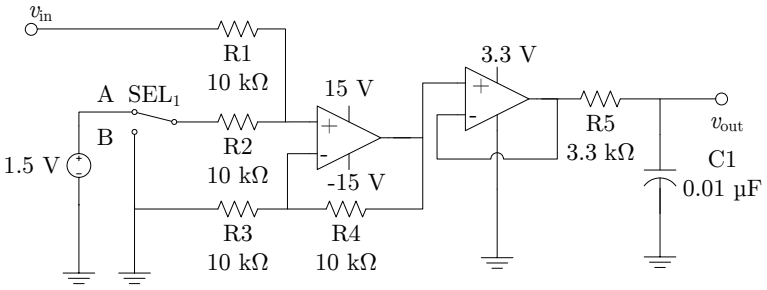

Figure 7: Signal adaptation and protection circuit.

In the first stage of the circuit, a 1.5 V level is added. This function is optional and should only be done when working with bipolar signals. If the input signal is unipolar, switch SEL1 to position B. Adding a level of 1.5 V allows the bipolar signals to be centered in the middle of the range allowed by the TMS320F28379D. The second stage of this card is a limiter that was implemented with the LM2902 operational amplifier; using a configuration where it acts as a voltage follower. Adjusting their saturation voltages to 0 V and 3.3 V, it is ensured that the signals that are sent to the analog port of the DSP, do not exceed that range. Finally the adjusted signal is passed through a passive low pass filter with a cutoff frequency of 4800 Hz. As it is an anti aliasing filter,

the maximum cutoff frequency is half the sampling frequency. Two cards with eight identical channels were designed and implemented. In addition, the card contains two voltage regulators. The first regulator generates the $1.5\,V$ reference signal. The second regulator provides the supply voltage so that the operational amplifiers are saturated at $0\,V$ and $3\,V$. A photograph of the adaptation and protection card is shown in Figure 8.

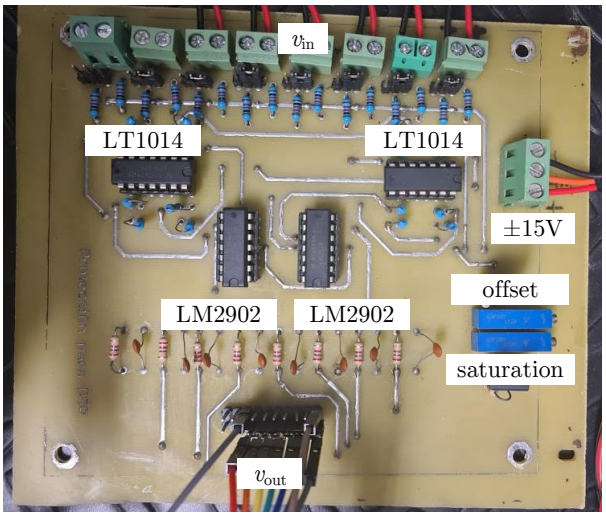

Figure 8: Signal adaptation and protection PCB.

Figure 9 shows a capture of the oscilloscope where the input signal is shown at the top, and at the output the identical signal but with an offset of $1.5\,V$.

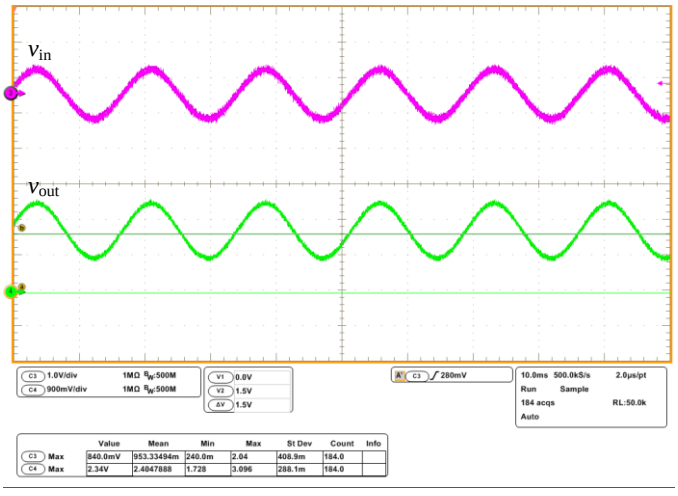

Figure 9: Input-output signals of the signal adaptation circuit, offset probe.

The next test consists of testing the protection capacity against voltage levels

outside the range of 0 V to 3 V. A signal is input that exceeds the limits and the second potentiometer is adjusted until the signal is cut at 3 V. A screenshot of the oscilloscope is shown in Figure 10. It shows, on channel 3, an input signal that exceeds the limits of the range allowed by the DSP. Channel 4 shows the same signal, only limited to between 0 and 3 V approximately.

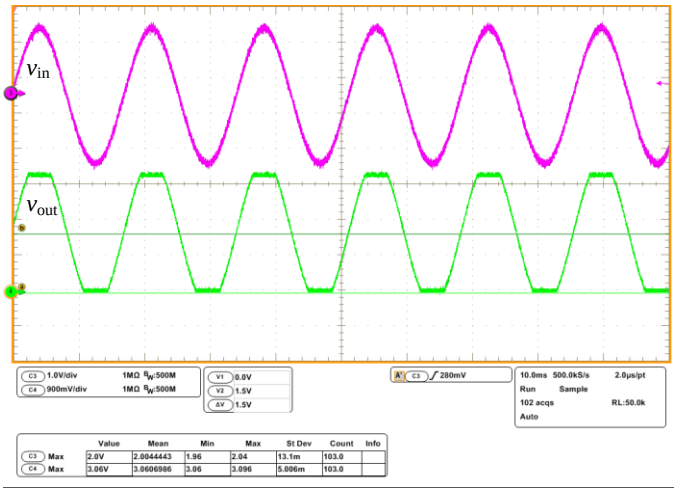

Figure 10: Input-output signals of the signal adaptation circuit, saturation probe.

Power stage development

At this stage, some elements that interact with the electrical network were designed and built and some others were selected. For practical and testing purposes a low voltage system was used. The grid voltage was regulated by means of a variable autotransformer, Variac.

Selection of the three-phase PWM converter The KIT8020CRD8FF1217P-1 CREE Silicon Carbide MOSFET Evaluation Kit is chosen due than It can be easily configured for several topologies from the basic phase-leg configuration and the power rating, furthermore the high efficiency given by the fabricant around that 98.9% at 4 kW.

The kit board can be flexible to implement difference topologies when using the different configurations of SiC MOSFETs and SiC diodes. It is possible to test several topologies with this board: synchronous Buck, non-synchronous Buck (or high-side Buck), synchronous Boost, non-synchronous Boost, half phase-leg bridge converter, H bridge converter (2x EVL boards) and bi-directional buck-boost converters.

Figure 11 shows the board.

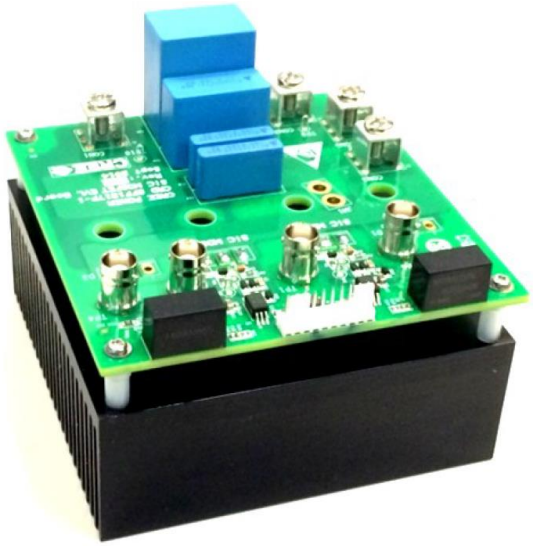

Figure 11: Cree KIT8020CRD8FF1217P-1 board assembly.

The package contents are shown follow in Table 3.

LCL filter design and construction For the LCL filter design the polynomial approach based on [7] was used considering a Butterworth polynomial. To use this method it is required the cutoff frequency and the nominal load. The cutoff frequency was calculated to fulfill with the voltage THD required by [70], being $\omega_r = 2\pi f_c = 2\pi\, 1.5\,\text{kHz} = 9.42$ rad/s and $Z_{load} = 96.8\ \Omega$. The normalized characteristic equation of the Butterworth polynomial is given by:

The inductors are shown in Figure 12 and Figure 13 wich are made of laminar core.

For the C_f four capacitor of 1 μF are put in parallel as is shown in Figure 14.

Table 3: Cree KIT8020CRD8FF1217P-1 content.

QTY-P/N	Description
1-CRD8FF1217P-1	Avago Driver version Eval board
4-AOS2182471	Ceramic tile
1-57908	Heat sink with mounting holes
2-C2M0080120D	80 mohm MOSFET
2-C4D20120D	20A Diode
1	Copper shorting strip
2-74270011	Ferrite Bead
8-91166a210	M3 washer, Zn-S
4-92005a129	M3x22mm, Zn-S
4-94669a727	Stand offs, Al spacer
4-92005a120	M3x10mm, Zn-S
1	User Guide

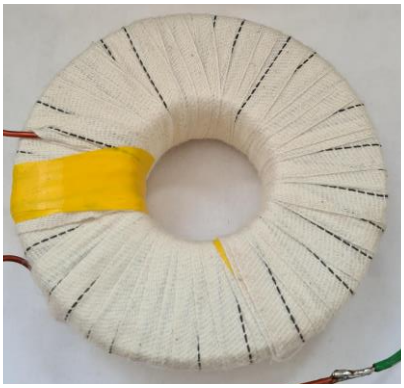

Figure 12: Inductor L_{f1}.

Figure 13: Inductor L_{f2}.

Figure 14: Capacitor C_f.

Bibliography

[1] R. R. E. P. Network, "Renewables 2022-global status report," 2022. xxix, 1, 2, 7

[2] 1547-2018, *IEEE Standard for Interconnection and Interoperability of Distributed Energy Resources with Associated Electric Power Systems Interfaces Sponsored by the IEEE Standard for Interconnection and Interoperability of Distributed Energy Resources with Associate*. IEEE, 2018. xxix, 10, 12, 13, 20, 41

[3] D. Mora, "Diseño y control de un sistema de almacenamiento de energía con base en baterías interconectado a la red," 10 2020. xxix, xxxiii, 8, 15, 25, 26

[4] U. Tamrakar, D. Shrestha, M. Maharjan, B. P. Bhattarai, T. M. Hansen, and R. Tonkoski, "Virtual inertia: Current trends and future directions," *Applied Sciences*, vol. 7, p. 654, 2017. xxix, xxx, 39, 41, 42, 43

[5] Nikos, J. Milanovic, C. Rahmann, V. Ajjarapu, C. Cañizares, I. Erlich, D. Hill, I. Hiskens, I. Kamwa, B. Pal, and others Hatziargyriou, "Stability definitions and characterization of dynamic behavior in systems with high penetration of power electronic interfaced technologies," *IEEE PES Technical Report PES-TR77*, 2020. xxx, 41, 43

[6] P. Kundur, *Power System Stability and Control - P. Kundur.pdf*. 1994. xxx, 43, 44

[7] A. I. Zverev, *Handbook of filter synthesis*. 1967. xxxiii, 16, 20, 21, 22, 84, 99

[8] BloombergNEF, "Battery pack prices fall to an average of price 132/ kwh, but rising commodity prices start to bite," 11 2021. 2

[9] M. Castilla, L. G. de Vicuña, and J. Miret, "Control of power converters in ac microgrids," 2019. 2

[10] N. Salehi, H. Martinez-Garcia, G. Velasco-Quesada, and J. M. Guerrero, "A comprehensive review of control strategies and optimization methods for individual and community microgrids," *IEEE Access*, vol. XX, pp. 1–1, 2022. 2

[11] R. Carnegie, D. Gotham, D. Nderitu, and P. V. Preckel, "Utility scale energy storage systems," 2013. 8

[12] P. J. dos Santos Neto, T. A. Barros, J. P. Silveira, E. R. Filho, J. C. Vasquez, and J. M. Guerrero, "Power management techniques for grid-connected dc microgrids: A comparative evaluation," *Applied Energy*, vol. 269, p. 115057, 7 2020. 9

[13] Y. Zhang, P. Yang, Z. Xu, and J. Chen, "Smooth mode transition strategies of pv-bess microgrids," *2017 2nd International Conference on Power and Renewable Energy, ICPRE 2017*, pp. 709–716, 2018. 10

[14] M. Cucuzzella, G. P. Incremona, and A. Ferrara, "Design of robust higher order sliding mode control for microgrids," *IEEE Journal on Emerging and Selected Topics in Circuits and Systems*, vol. 5, pp. 393–401, 2015. 10

[15] L. Zhang, Y. Dong, Z. Chen, X. Xie, H. Sun, and Z. Liu, "An integrated control strategy of battery energy storage system in microgrid," *IET Conference Publications*, vol. 2013, 2013. 10

[16] M. Fusero, A. Tuckey, A. Rosini, P. Serra, R. Procopio, and A. Bonfiglio, "A comprehensive inverter-bess primary control for ac microgrids," *Energies*, vol. 12, 2019. 10

[17] S. Zafar, H. Sadiq, B. Javaid, and H. A. Khalid, "On pq control of bess in grid-connected mode and frequency control in islanded-mode for micro-grid application," *2018 International Conference on Computing, Electronic and Electrical Engineering, ICE Cube 2018*, pp. 1–6, 2019. 10

[18] D. Mora, N. Ciro, N. Visairo, J. Segundo, and E. Camargo, "Control for three-phase lcl-filter pwm rectifier with bess-oriented application," 2019. 10

[19] S. Shan and L. Umanand, "A unified controller for utility-interactive uninterruptible power converters for grid connected and autonomous operations," *IEEE Transactions on Power Electronics*, vol. 34, pp. 3871–3887, 2019. 10

[20] M. Karimi-Ghartemani, S. A. Khajehoddin, P. Piya, and M. Ebrahimi, "Universal controller for three-phase inverters in a microgrid," *IEEE Journal of Emerging and Selected Topics in Power Electronics*, vol. 4, pp. 1342–1353, 2016. 10

[21] S. Bayhan and H. Abu-Rub, "A simple control technique for distributed generations in grid-connected and islanded modes," *IEEE International Symposium on Industrial Electronics*, vol. 2018-June, pp. 1237–1242, 2018. 10, 11

[22] B. Onar and S. evki Demirbas, "A survey on the provision of smooth transition between operation modes in pv-bess microgrid," pp. 203–207, Institute of Electrical and Electronics Engineers (IEEE), 8 2022. 10

[23] S. Kannan, R. K. Gnanasekar, and K. Vasudevan, "Novel unified control strategies for seamless transfer of operation of three-phase pv-inverter from grid-tied to islanded mode," *CIRED*, pp. 7–8, 2018. 10

[24] S. D'Silva, M. Shadmand, S. Bayhan, and H. Abu-Rub, "Towards grid of microgrids: Seamless transition between grid-connected and islanded modes of operation," *IEEE Open Journal of the Industrial Electronics Society*, vol. 1, pp. 66–81, 2020. 10

[25] O. P. Jaga and S. G. Choudhuri, "Seamless transition between grid-connected and islanded operation modes for hybrid pv-bess combination used in single-phase, critical load applications," Institute of Electrical and Electronics Engineers Inc., 1 2021. 10

[26] I. Sindhuja, Y. K. Latha, and V. Aparna, "A unified seamless transfer control scheme for grid-connected and islanding modes of operation of grid- connected pv system," *Indian Journal of Science and Technology*, vol. 9, 2016. 11

[27] Z. Liu and J. Liu, "Indirect current control based seamless transfer of three-phase inverter in distributed generation," *IEEE Transactions on Power Electronics*, vol. 29, pp. 3368–3383, 2014. 11, 29

[28] M. Mao, Z. Dong, Y. Ding, and L. Chang, "A unified controller for a microgrid based on adaptive virtual impedance and conductance," *2014 IEEE Energy Conversion Congress and Exposition, ECCE 2014*, pp. 695–701, 2014. 11

[29] M. Ganjian-Aboukheili, M. Shahabi, Q. Shafiee, and J. M. Guerrero, "Seamless transition of microgrids operation from grid-connected to islanded mode," *IEEE Transactions on Smart Grid*, vol. 11, pp. 2106–2114, 5 2020. 11

[30] R. N. Beres, X. Wang, M. Liserre, F. Blaabjerg, and C. L. Bak, "A review of passive power filters for three-phase grid-connected voltage-source converters," *IEEE Journal of Emerging and Selected Topics in Power Electronics*, vol. 4, pp. 54–69, 2016. 16

[31] H. Athari, M. Niroomand, and M. Ataei, "Review and classification of control systems in grid-tied inverters," *Renewable and Sustainable Energy Reviews*, vol. 72, pp. 1167–1176, 2017. 16

[32] S. Butterworth, "On the theory of filter amplifiers," *Experimental Wireless and The Wireless Engineer*, pp. 536–541, 1930. 20

[33] T. Hornik and Q.-C. Zhong, *Control of power inverters in renewable energy and smart grid integration*. John Wiley {$} Sons, 2012. 25

[34] W. Zhang, H. Liu, W. Wang, and P. C. Loh, "Seamless transfer scheme for parallel pv inverter system," *IET Power Electronics*, vol. 13, pp. 1051–1058, 2020. 25

[35] J. He and Y. W. Li, "Hybrid voltage and current control approach for dg-grid interfacing converters with lcl filters," *IEEE Transactions on Industrial Electronics*, vol. 60, pp. 1797–1809, 2012. 25

[36] M. B. Delghavi and A. Yazdani, "A unified control strategy for electronically interfaced distributed energy resources," *IEEE Transactions on Power Delivery*, vol. 27, pp. 803–812, 2012. 26

[37] C. Nunez, N. Visairo-Cruz, A. Arellanes, D. Mora, and J. Segundo, "Holistic control approach for the grid-connected converter of a battery energy storage system," *IEEE Access*, vol. 8, pp. 216844–216855, 2020. 27, 29, 36, 80

[38] Z. Li, "Design and analysis of improved butterworth low pass filter," *2007 8th International Conference on Electronic Measurement and Instruments, ICEMI*, pp. 1729–1732, 2007. 29

[39] M. Sandhu, S. Kaur, and J. Kaur, "A study on design and implementation of butterworth , chebyshev and elliptic filter with matlab," *International Journal of Emerging Technologies in Engineering Research (IJETER)*, vol. 4, pp. 111–114, 2016. 29

[40] W. M. Laghari, M. U. Baloch, M. A. Mengal, and S. J. Shah, "Performance analysis of analog butterworth low pass filter as compared to chebyshev type-i filter, chebyshev type-ii filter and elliptical filter," *Circuits and Systems*, vol. 05, pp. 209–216, 2014. 29

[41] C. tsong Chen, *LINEAR SYSTEM Third Edition*. 1999. 31

[42] D. Graham and R. C. Lathrop, "The synthesis of "optimum" transient response: Criteria and standard forms," *Transactions of the American Institute of Electrical Engineers, Part II: Applications and Industry*, vol. 72, pp. 273–288, 2013. 36

[43] W. Winter, K. Elkington, G. Bareux, and J. Kostevc, "Pushing the limits: Europe's new grid: Innovative tools to combat transmission bottlenecks and reduced inertia," *IEEE Power and Energy Magazine*, vol. 13, pp. 60–74, 2014. 38

[44] J. Bomer, K. Burges, C. Nabe, and M. Poller, "All island tso faciliation of renewables study—final report for work package 3 ecofys," 2010. 38

[45] M. Kayikci and J. V. Milanovic, "Dynamic contribution of dfig-based wind plants to system frequency disturbances," *IEEE Transactions on Power Systems*, vol. 24, pp. 859–867, 2009. 38

[46] J. Fang, P. Lin, H. Li, Y. Yang, and Y. Tang, "An improved virtual inertia control for three-phase voltage source converters connected to a weak grid," *IEEE Transactions on Power Electronics*, vol. 34, pp. 8660–8670, 2018. 38, 41

[47] T. Younis, M. Ismeil, E. K. Hussain, and M. Orabi, "Improved single-phase self-synchronised synchronverter with enhanced dynamics and current limitation capability," *IET Power Electronics*, vol. 12, pp. 337–344, 2019. 38

[48] D. Shrestha, *Virtual inertia emulation to improve dynamic frequency stability of low inertia microgrids*. South Dakota State University, 2016. 38, 44

[49] J. Alipoor, Y. Miura, and T. Ise, "Power system stabilization using virtual synchronous generator with alternating moment of inertia," *IEEE journal of Emerging and selected topics in power electronics*, vol. 3, pp. 451–458, 2014. 38, 41

[50] G. Delille, B. Francois, and G. Malarange, "Dynamic frequency control support by energy storage to reduce the impact of wind and solar generation on isolated power system's inertia," *IEEE Transactions on sustainable energy*, vol. 3, pp. 931–939, 2012. 40, 41

[51] Y. Liu, S. You, J. Tan, Y. Zhang, and Y. Liu, "Frequency response assessment and enhancement of the u.s. power grids toward extra-high photovoltaic generation penetrations—an industry perspective," *IEEE Transactions on Power Systems*, vol. 33, pp. 3438–3449, 5 2018. 40

[52] W. Uijlings, D. Street, and S. London, "An independent analysis on the ability of generators to ride through rate of change of frequency values up to 2hz/s," *EirGrid, London, UK, Rep*, vol. 16010927, 2013. 41

[53] ENTSO-E, "Continental europe operation handbook, appendix a: Load-frequency control and performance," 2004. 41

[54] J. Driesen and K. Visscher, "Virtual synchronous generators," pp. 1–3, IEEE, 7 2008. 41

[55] Y. Hirase, K. Abe, K. Sugimoto, K. Sakimoto, H. Bevrani, and T. Ise, "A novel control approach for virtual synchronous generators to suppress frequency and voltage fluctuations in microgrids," *Applied Energy*, vol. 210, pp. 699–710, 2018. 41

[56] L. Xia and L. Hai, "Comparison of dynamic power sharing characteristics between virtual synchronous generator and droop control in inverter-based microgrid," pp. 1548–1552, 2017. 41

[57] H. Bevrani, T. Ise, and Y. Miura, "Virtual synchronous generators: A survey and new perspectives," *International Journal of Electrical Power and Energy Systems*, vol. 54, pp. 244–254, 2014. 41

[58] M. Torres and L. A. C. Lopes, "Virtual synchronous generator: A control strategy to improve dynamic frequency control in autonomous power systems," 2013. 41

[59] P. Tielens and D. V. Hertem, "The relevance of inertia in power systems," *Renewable and Sustainable Energy Reviews*, vol. 55, pp. 999–1009, 2016. 41

[60] M. P. N. V. Wesenbeeck, S. W. H. D. Haan, P. Varela, and K. Visscher, "Grid tied converter with virtual kinetic storage," pp. 1–7, 2009. 41

[61] P. Kundur, J. Paserba, V. Ajjarapu, G. Andersson, A. Bose, C. Canizares, N. Hatziargyriou, D. Hill, A. Stankovic, C. Taylor, T. V. Cutsem, and V. Vittal, "Definition and classification of power system stability ieee/cigre joint task force on stability terms and definitions," *IEEE Transactions on Power Systems*, vol. 19, pp. 1387–1401, 2004. 41

[62] J. Rocabert, A. Luna, F. Blaabjerg, and P. Rodríguez, "Control of power electronic converters in ac microgrids," *Power Systems*, vol. 27, pp. 329–355, 2012. 44

[63] J. Rahman and M. Fripp, "Provision of inertial and droop response by controlling the charging rate of battery pack," 2018. 44

[64] H. Saadat, "Power system analysis," 1999. 46

[65] C. Sun, S. Q. Ali, Geza, Joos, and F. Bouffard, "Design of hybrid-storage-based virtual synchronous machine with energy recovery control considering energy consumed in inertial and damping support," *IEEE Transactions on Power Electronics*, vol. 37, pp. 2648–2666, 2021. 46

[66] IEC-60146-1-2, *Semiconductor converters-General requirements and line commutated converters*. 2009. 49, 63

[67] X. Wang, M. Yue, and E. Muljadi, "Pv generation enhancement with a virtual inertia emulator to provide inertial response to the grid," *2014 IEEE Energy Conversion Congress and Exposition, ECCE 2014*, pp. 17–23, 2014. 58

[68] I. Dobson, H.-D. Chiang, J. S. Thorp, and L. Fekih-Ahmed, "A model of voltage collapse in electric power systems," 1988. 74

[69] A. Arellanes, C. Nuñez, N. Visairo, and A. A. Valdez-Fernandez, "An improvement of holistic control tuning for reducing energy consumption in seamless transitions for a bess grid-connected converter," *Energies*, vol. 15, p. 7964, 10 2022. 80

[70] I. S. A. I. Standard and U. 2014, "Ieee application guide for ieee std 1547(tm), ieee standard for interconnecting distributed resources with electric power systems." 99